

**Studying Hydrogen Emission Lines
from Classical T Tauri Stars:
Telluric Line Removal, Physical
Conditions in the Emitting Gas,
and Reddening**

Dissertation
zur Erlangung des Doktorgrades
des Fachbereichs Physik
der Universität Hamburg

vorgelegt von
Natascha Rudolf

aus Hamburg

Hamburg
2014

Gutachter der Dissertation: Prof. Dr. Jürgen H. M. M. Schmitt
Prof. Dr. Ralph Neuhäuser

Gutachter der Disputation: Prof. Dr. Robi Banerjee
Dr. Frederic V. Hessman

Datum der Disputation: 26. Juni 2014

Vorsitzender des Prüfungsausschusses: Dr. Robert Baade

Vorsitzende des Promotionsausschusses: Prof. Dr. Daniela Pfannkuche

Dekan der MIN Fakultät: Prof. Dr. Heinrich Graener

Zusammenfassung

Während ihrer Entstehung durchlaufen Sterne verschiedene Entwicklungsphasen, bevor sie die Hauptreihe erreichen. Sie bilden sich durch den gravitativen Kollaps von molekularen Wolken. Die Erhaltung des Drehimpulses erfordert es, dass die Massenakkretion nicht radial, sondern von einer Scheibe aus stattfindet. Sterne mit niedriger Masse, die sich in einer Entwicklungsphase befinden, in der sich das meiste Material in der Scheibe befindet und der Stern nicht mehr in der Wolke verborgen ist, werden klassische T Tauri Sterne (CTTS) genannt. Diese Arbeit befasst sich mit der zirkumstellaren Umgebung dieser Sterne.

Die Untersuchungen basieren auf VLT/X-Shooter-Spektren von 20 Sternen mit unterschiedlichen Spektraltypen und Massenakkretionsraten. Die X-Shooter-Spektren decken zeitgleich einen Spektralbereich von etwa 3000 Å bis etwa 25 000 Å bei einer mittleren Auflösung ($R \sim 10\,000$) ab. Ein wichtiger Schritt der Datenreduktion ist die Entfernung der tellurischen Linien, die die Erdatmosphäre dem Spektrum hinzufügt. An Stelle der Nutzung beobachteter tellurischer Standardsterne verwende ich Modelle der atmosphärischen Transmission, die an die Wetterbedingungen zum Zeitpunkt der Beobachtung angepasst sind, um diese Kontamination zu entfernen.

Für die Analyse von CTTS-Spektren ist es sehr wichtig die Stärke der Rötung zu kennen, daher nutze ich eine neue Methode um die Rötung zu messen. Das Verhältnis von emittierten Wasserstofflinien mit dem selben oberen Niveau ist unabhängig von den Bedingungen im Gas und gegeben durch Konstanten, die aus der Atomphysik bekannt sind. Somit kann eine Differenz zwischen den beobachteten und den theoretischen Linienverhältnissen nur durch die Rötung verursacht werden. Die Messung der Extinktion für mehrere Linienpaare mit dem selben oberen Niveau auf diese Weise erlaubt es mir, neue Extinktionswerte A_V für sechs Objekte zu bestimmen. Obwohl die Form des Rötungsgesetzes mit dieser neuen Methode ebenfalls untersucht werden kann, finde ich aufgrund relativ hoher Fehler der Daten keine Abweichung vom üblicherweise für den Infrarotbereich genutzten Rötungsgesetz, $A \sim \lambda^{-1.84}$.

Das aktuelle Modell der Akkretion auf CTTS ist das Modell des magnetisch kontrollierten Einfalls. In diesem Modell fällt das Material entlang der Magnetfeldlinien in Akkretionstrichtern auf den Stern. Dieses Modell erklärt die wesentlichen Merkmale, die wir bei CTTS beobachten, jedoch sind die physikalischen Eigenschaften des emittierenden Gases noch unklar. Die Temperatur T und die Elektronendichte n_e im Gas können aus einer Analyse von Wasserstoffemissionslinien bestimmt werden. Ich messe die Flüsse der Wasserstoffemissionslinien der Paschen- und Brackett-Serie und vergleiche die Linienverhältnisse der höheren Paschen-Linien zu $\text{Pa}\beta$, $\text{Br}\gamma$ zu den höheren Paschen-Linien und der höheren Brackett-Linien zu $\text{Br}\gamma$ mit den Vorhersagen der sogenannten Fall-B-Modelle für rekombinierenden Wasserstoff. Die Fall-B-Modelle nehmen an, dass das Gas in der Lyman-Serie optisch dick ist und optisch dünn in allen anderen Übergängen. Dies ergibt Temperaturen zwischen 500 K und 5000 K und Dichten zwischen 10^9 cm^{-3} und 10^{10} cm^{-3} . Eine große Quelle für Unsicherheiten in dieser Analyse ist die Entrötung der Linienflüsse. Allerdings ergeben die Fall-B-Modelle selbst bei Objekten, bei denen die Entrötung plausibel erscheint, oft keine statistisch gute Übereinstimmung mit den Daten. Dies wirft die Frage auf, ob die Annahmen der Fall-B-Modelle die angemessene Beschreibung sind für die Bedingungen in der Region von CTTS, in der die Wasserstofflinien entstehen. Es scheint, dass allgemeinere Modelle der Linienanregung und -rekombination nötig sind um die Beobachtungen zu erklären.

Wenn die gefundenen physikalischen Eigenschaften zutreffend sind, stimmen sie mit den Vorhersagen von magnetosphärischen Akkretionsmodellen bezogen auf die Dichten überein, die gefundenen Temperaturen sind allerdings niedriger. Die niedrigen Temperaturen des Gases implizieren sehr kurze Abkühlzeiten von nur einigen Minuten. Dies deutet auf die Notwendigkeit hin, das Modell des magnetisch kontrollierten Einfalls weiterzuentwickeln um weitere Prozesse und Beiträge einzuschließen, die für die Entstehung von Emissionslinien wichtig sind.

Abstract

During their formation stars go through different evolutionary stages before reaching the main sequence. They form from a molecular cloud via gravitational collapse. The conservation of angular momentum requires the mass accretion to proceed not radially but from a disk. Low-mass stars at an evolutionary stage, where most material is in the disk and the star is not hidden inside a cloud any more, are called classical T Tauri stars (CTTS). This thesis deals with the circumstellar environment of these stars.

The study is based on VLT/X-Shooter spectra of 20 stars with different spectral types and mass accretion rates. The X-Shooter spectra simultaneously cover the spectral range from about 3000 Å to about 25 000 Å at medium resolution ($R \sim 10\,000$). An important data reduction step is the removal of telluric lines imprinted on the spectra by the atmosphere of the Earth. Instead of using observed telluric standards, I employ models of the atmospheric transmission adapted to the weather conditions at the time of observation to remove the contamination.

For the analysis of CTTS spectra, it is very important to know the amount of reddening of the light. Therefore, I apply a new method to measure the reddening. The ratio of emitted hydrogen lines with a common upper level is independent of the conditions in the gas and given by constants known from atomic physics. Thus, a difference between the observed and the theoretical line ratios can only be caused by reddening. Measuring the extinction for several common upper level line pairs in this way allows me to determine new extinction values A_V for six objects. Although the shape of the reddening law can also be tested with this new method, I do not find a deviation from the standard reddening law in the near-infrared, $A \sim \lambda^{-1.84}$, due to relatively high uncertainties of the data.

The current model of accretion onto CTTS is the magnetically funnelled infall model. In this model, the material falls onto the star along the magnetic field lines in accretion funnels. This model explains the main features we observe from CTTS, but the physical conditions in the emitting gas are still uncertain. The temperature T and the electron density n_e in the gas can be deduced from an analysis of hydrogen emission lines. I measure the hydrogen emission line fluxes in the Paschen and Brackett lines and compare the line ratios of the higher order Paschen lines to $\text{Pa}\beta$, $\text{Br}\gamma$ to the higher order Paschen lines, and the higher order Brackett lines to $\text{Br}\gamma$ to the predictions of the so-called case B models for recombining hydrogen. The case B models assume that the gas is optically thick in the Lyman series and optically thin in all other transitions. This yields temperatures between 500 K and 5000 K and densities between 10^9 cm^{-3} and 10^{10} cm^{-3} . A major source of uncertainty for this analysis is the dereddening of the line fluxes. However, even for objects where the dereddening seems reasonable, the case B models often do not provide a statistically good fit to the data. This raises the question whether the assumptions of the case B model are the appropriate description of the conditions in the hydrogen line formation region of CTTS. It seems that more general models of line excitation and recombination are required to explain the observations.

If applicable, the physical conditions found agree with predictions by magnetospheric accretion models in terms of density, but the temperatures found here are lower. The low temperatures of the gas imply very short cooling times of only a few minutes. This points towards a necessity to refine the magnetically funnelled infall model to include further processes and contributions that are important for the emission line formation.

Contents

1	Introduction	1
1.1	From clouds to stars	1
1.2	The main sequence	3
1.3	The final phases of a stellar life	4
1.4	Remarks on the structure of this work	5
2	T Tauri Stars and Their Environment	7
2.1	Observational characteristics	7
2.1.1	Disk and outflows	8
2.1.2	Accretion	8
2.2	The magnetically funnelled infall model	10
2.3	Reddening and dust	12
3	Observations and Data Reduction	17
3.1	The instrument: VLT/X-Shooter	17
3.2	The sample	18
3.3	Data reduction using the ESO pipeline	18
3.4	Flux calibration	19
3.4.1	Using the white dwarf standards	19
3.4.2	Using the telluric standards	20
3.5	Additional reduction steps	24
4	Telluric Line Removal	29
4.1	Modelling telluric line spectra in the optical and infrared with an application to VLT/X-Shooter spectra	29
4.2	Preface of the user manual	37
4.3	Preparations	37
4.3.1	Installation of LBLRTM	37
4.3.2	Creating the line database	38
4.3.3	Model atmosphere	38
4.3.4	MPFIT and IDL Astronomy User's Library	39
4.3.5	Reduction of the spectra	40
4.3.6	<code>tellrem</code> input file	40
4.3.7	Testing the package	40
4.4	The program package	41
4.5	Basics of using LBLRTM	42
4.5.1	The TAPE5	43
4.5.2	Other points to know	44
4.6	Using <code>tellrem</code> for other spectra	44
4.6.1	Input	44
4.6.2	Adapting the routines	44

5	Relevant Theories and Methods	47
5.1	Hydrogen emission line fluxes	47
5.1.1	Measuring the line fluxes	47
5.1.2	Estimating the uncertainties of the line fluxes	49
5.2	Models for the level populations N_{nl} in recombining hydrogen	53
5.3	Reddening of ratios of common upper level hydrogen lines	54
5.4	Application to classical T Tauri stars	56
5.4.1	The temperature T and the electron density n_e in the emitting gas	56
5.4.2	The extinction value A_V and the exponent α of the reddening power law	57
6	Results and Discussion	59
6.1	The temperature T and the density n_e in the emitting gas	59
6.2	Discussion of the physical conditions in the emitting gas of classical T Tauri stars	70
6.3	The reddening towards classical T Tauri stars	72
6.4	Discussion concerning the extinction and the reddening law	74
6.5	Using the newly determined A_V values for the estimation of the temperature T and the electron density n_e	76
7	Summary and Outlook	83
7.1	Summary	83
7.1.1	Telluric line removal	83
7.1.2	The physical conditions in the emitting gas	83
7.1.3	The reddening towards classical T Tauri stars	84
7.2	Outlook	84
7.2.1	Adaptation of <code>tellrem</code> for TIGRE	84
7.2.2	The physical conditions in the emitting gas	84
7.2.3	Characterising the sample stars	85
7.2.4	The reddening towards classical T Tauri stars	85
A	Documentation for <code>tellrem</code> Routines	87
A.1	<code>CREATE_STANDARD_PARINFO</code>	87
A.2	<code>EXCLUSION</code>	87
A.3	<code>FITTELL</code>	88
A.4	<code>GAUSSCONV</code>	89
A.5	<code>GETABUNDANCES</code>	90
A.6	<code>GETOBJECTS</code>	91
A.7	<code>IDLPLOTTITLECHANGER</code>	91
A.8	<code>LOADTELLREMINFO</code>	92
A.9	<code>RDDAT</code>	93
A.10	<code>READMODATM</code>	93
A.11	<code>RECRFITTELLRES</code>	94
A.12	<code>RUNLBLRTM</code>	95
A.13	<code>STATUSINTERPRETER</code>	96
A.14	<code>SUBZERO</code>	97
A.15	<code>TELL</code>	98
A.16	<code>TELLREM</code>	98
A.17	<code>TELLREMPARAMETERS</code>	99
A.18	<code>TELLREMSPECTRA</code>	101
A.19	<code>TELLREM_TEST_RUN</code>	102
A.20	<code>TELLWITHOUT</code>	102
A.21	<code>UVEXTINCTION</code>	103
A.22	<code>WHICHGDAS</code>	104

B Annotated Example TAPE5	105
C Additional Tables	107
C.1 Hydrogen emission line fluxes	107
C.2 Flux calibration	111
C.3 Additional reduction steps	112
C.4 The temperature T and the density n_e in the emitting gas	112
C.5 Using the newly determined A_V values for the estimation of the temperature T and the electron density n_e	117
D Additional Plots	119
D.1 Uncertainty of relative flux calibration	119
D.2 Uncertainty of absolute flux calibration	120
List of Figures	121
List of Tables	123
Bibliography	125

Chapter 1

Introduction

The objects in the sky above us have been watched since the dawn of mankind. In a human life time the sky seems to be static, only the movement of the Sun, the Moon, and the planets along the celestial sphere and the yearly movement of the stellar constellations cause some change. For the unaided eye, the stars themselves seem to be unchangeable and everlasting. Only rare events like comets or a galactic supernovae, the conclusion of the evolution of massive stars, break the quiet.

The evolution of stars takes place over long time scales, so that the shift between individual stages is beyond detection even within several human lifespans. Only in the middle of the 20th century astronomers found evidence for the early stages of stellar evolution. However, on astronomical time scales the birth of stellar and planetary systems is a fast process taking only a few million years.

In this chapter I present an overview on the life cycle of stars focusing on the early evolutionary phases and the further development of low-mass stars, followed by a short overview on the structure of this work.

1.1 From clouds to stars

The space between the stars of a spiral galaxy is not empty. While most of the baryonic matter is indeed concentrated in the stars, between 20 % and 50 % remains in the interstellar medium (Bell et al. 2003). A large amount of this matter is in dense and cold molecular clouds. These clouds obscure the light of background stars at optical wavelengths, making them appear as dark spots in the sky, whereas infrared light is not totally blocked. This is illustrated in Figure 1.1 using the example of the dark cloud Barnard 68. Small molecular clouds like this are also called Bok globules. The temperature inside these clouds is only on the order of ten Kelvin. The outer regions can reach temperatures on the order of thousand Kelvin due to illumination by other stars. The main constituent of these clouds is molecular hydrogen, but also a vast range of other molecules is able to form, e.g. CO, NH₃, CS, and HCN (Dobbs et al. 2013). The Cologne Database for Molecular Spectroscopy (Müller et al. 2001) lists around 180 molecules that have been detected in the interstellar medium or in circumstellar material. Dust particles facilitate condensation of some elements, while the surface of the dust offers an environment for chemical reactions.

Within the clouds, the matter is constantly in motion. Flows and turbulence disturb the structure. If the mass of a cloud or a part thereof exceeds a critical mass, the Jeans mass, which depends on temperature and density, the cloud undergoes a gravitational collapse. The Jeans mass is typically thousands to tens of thousands of solar masses. Higher masses are needed at higher temperatures because the thermal pressure counteracts the gravitational contraction. For a few thousand years these protostars get denser and hotter. These objects are difficult to observe, because they are still hidden in the surrounding envelope of matter. Only infrared (IR) and radio emission are able to escape from these objects. They are also called IR class 0 sources.

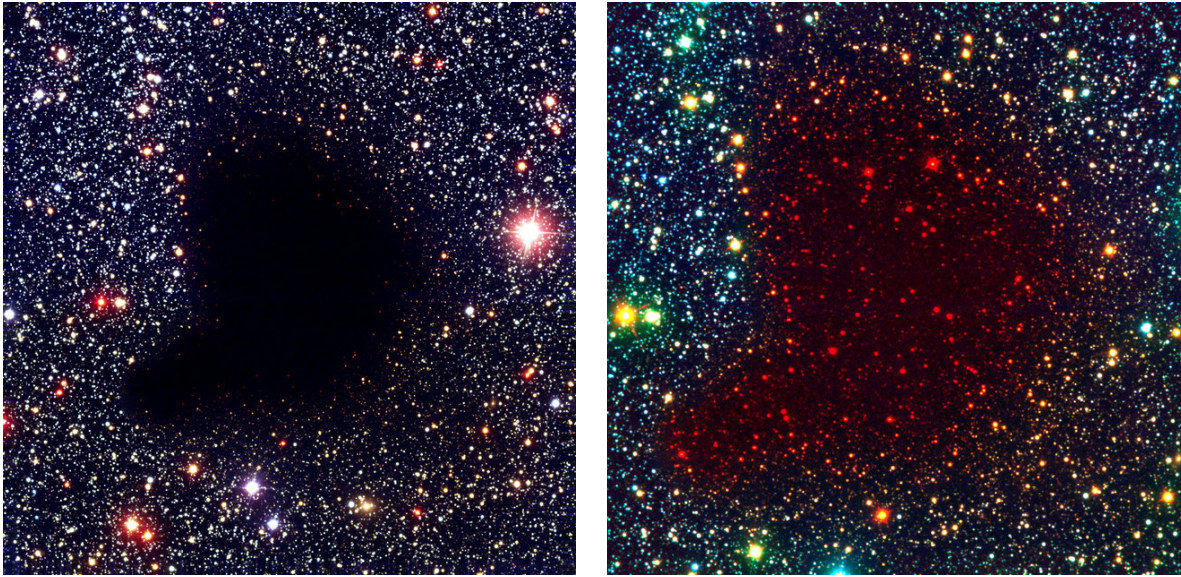


Figure 1.1: Observations of the dark cloud Barnard 68 in various bands combined into two colour composites. On the *left*, a composite of images in the optical filters B (blue), V (green), and I (red) is shown, while on the *right* a false-colour composite of images in the filters B (blue), I (green), and K_s (red) is displayed (Image credit: ESO).

Very massive molecular clouds typically form a large number of stars. An example of a star forming region with stars at different stages of their formation process is shown in Figure 1.2. The initial angular momentum of the accreted material has to be conserved, so the object rotates around an axis. The envelope material falls to the rotational plane and develops a thick disk. The object now has become an evolved protostar (IR class I) with an age on the order of 10^5 years. As the evolution continues, many objects develop powerful bipolar outflows in the form of highly collimated jets (see e.g. the review by Frank et al. 2014). Some objects already develop outflows in the class 0 stage. These outflows return mass and momentum to the natal cloud and drive turbulence in the cloud. In regions, where the jet interacts with the interstellar medium or different parts of the jet with different velocities collide, shocks form that heat up the material. These “knots” are observable as diffuse emission regions mainly in $H\alpha$, the so-called Herbig-Haro objects (see e.g. the review by Reipurth & Heathcote 1997).

Once the residual gas and dust of the envelope are either accreted onto the disk or blown out of the system by stellar wind and outflows, the star becomes visible in the optical (IR class II). After the prototypical system of this class, T Tauri, these stars are called classical T Tauri stars (CTTS, Joy 1945). For a few million years the star continues to accrete matter from the disk. This stage of the evolution is described in more detail in Chapter 2. This disk is comprised of gas and dust from the original cloud. The surface of the disk is heated to a few thousand Kelvin by the central star. In the midplane of the disk the temperatures are much lower (see e.g. the review by Dutrey et al. 2014). Here, the dust settles down gravitationally. In this region planet formation occurs, but there are still open questions concerning the growth mechanisms. Upon collision, smaller particles stick together in a process called coagulation. Once a sufficient mass is reached, the gravity of a fragment allows it to grow further. The physical conditions in the disk can also cause the protoplanets to migrate inwards or outwards. Once the disk is dispersed the process of planet formation ends.

Matter leaves the disk due to several processes: accretion onto the protoplanets and onto the central star as well as ejection from the system by the combined pressure of the radiation, and the stellar and the disk winds. Once the supply of new matter from the circumstellar envelope stops, the disk mass decreases. At an age of a few million years, the disk becomes thin and the mass accretion rate drops. Stars at this evolutionary stage are called weak-lined T Tauri stars



Figure 1.2: The star forming region NGC 2174 observed by the Hubble space telescope. This composite image combines data from three filters in the infrared: Y (blue), J (green), and H (red) (Image Credit: NASA, ESA, and the Hubble Heritage Team (STScI/AURA)).

(WTTS, IR class III, see e.g. Herbig & Bell 1988).

During its formation the star contracts and therefore the temperature in its core increases. In the T Tauri phase deuterium burning takes places. The star contracts further until the temperature required to start hydrogen fusion is reached. The star now stabilises and stays that way for a time significantly longer than the evolution took to arrive at this point.

1.2 The main sequence

Once the fusion of hydrogen has started, the star is said to be on the main sequence. It stays in hydrostatic equilibrium as long as the energy supplied by the fusion process compensates the energy loss due to radiation. Stars with higher mass are hotter and more luminous than low mass stars. This is typically depicted using a Hertzsprung-Russel diagram (HR diagram, e.g. Unsöld & Baschek 2002) of the temperature and the luminosity of the stars (Figure 1.3), where higher-mass stars are found in the upper left region. Low-mass stars are located in the lower right corner. They have luminosities similar to the Sun or below. Higher-mass stars consume

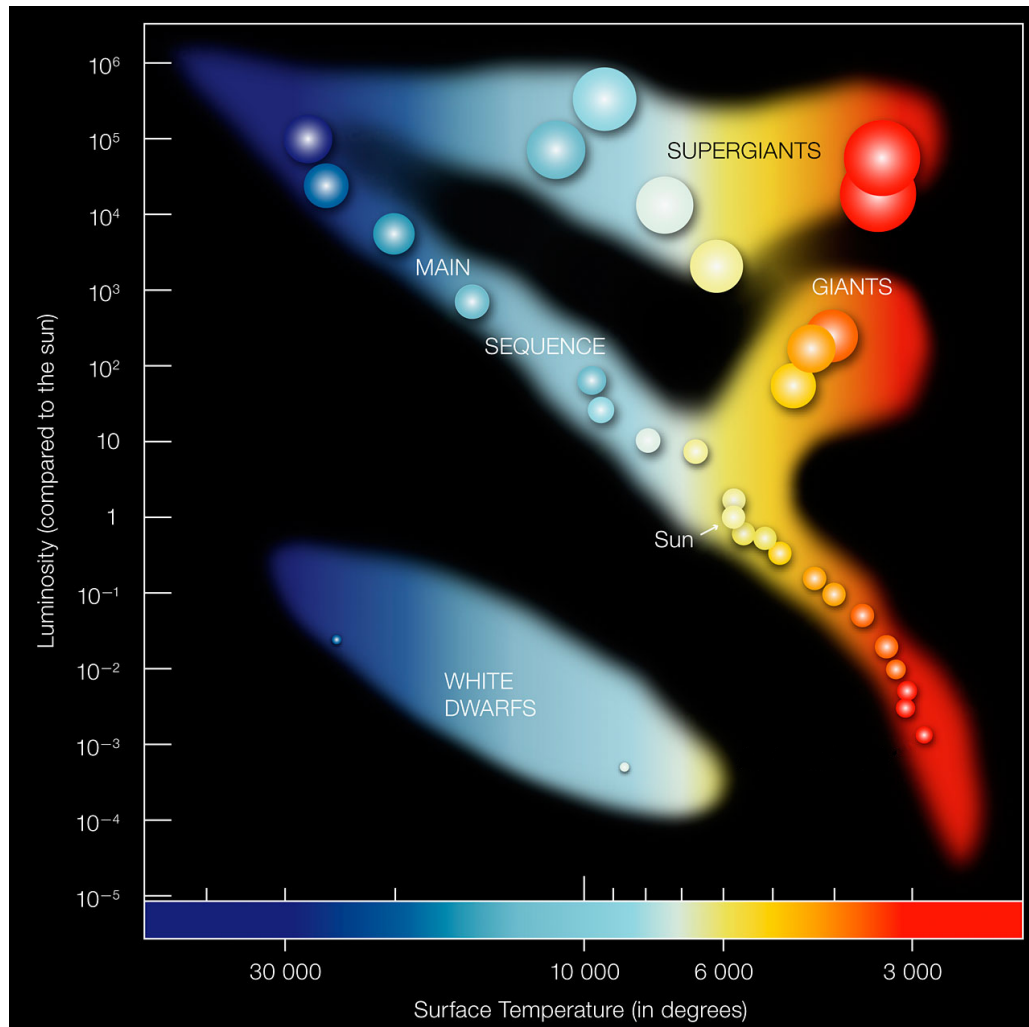


Figure 1.3: A schematic Hertzsprung-Russel (HR) diagram (Image Credit: ESO).

their energy resources much faster. A star with a temperature of about 30 000 K on the surface with a luminosity 10^4 to 10^5 times the solar luminosity stays on the main sequence for only about 10^7 years or less. The Sun, however, with a surface temperature of about 6000 K will be on the main sequence for about 10^{10} years in total. For stars with even lower masses, the main sequence life time gets even longer. This circumstance is used to determine the age of stellar populations, e.g. a cluster of stars: the most massive star that is still on the main sequence indicates the age (e.g. Unsöld & Baschek 2002).

1.3 The final phases of a stellar life

When the hydrogen burning in the core ceases at the end of the main sequence life time of a star, the equilibrium state cannot be maintained any longer. In stars with masses below about 2.5 solar masses the core now collapses and the released energy heats the layers around the core, causing hydrogen to fuse in these shells. The outer layers expand and the star moves up the giant branch in the HR diagram as its luminosity increases. The giants and their different evolutionary stages described in the following are located in the upper right in Figure 1.3. When the electrons in the core are Fermi-Dirac degenerated and the temperature rises high enough, helium burning starts with a so-called helium flash. The helium fusion produces enormous amounts of energy in a runaway process until the increasing temperature ends the degeneracy. The helium burning stabilises and proceeds in the core for a while surrounded by a shell, where hydrogen burning takes place. The star is now on the horizontal branch and contracts again

increasing its surface temperature. Once the fusion process in the core stops, it continues in a shell and the star ascends the asymptotic giant branch. The shell burning is unstable, periodically causing thermal pulses which then increase the luminosity of the star. When there is not enough material for shell burning left, the star contracts again expelling its outer shells. This creates a planetary nebula with a hot central star. The star contracts until the electrons degenerate, stopping the compression. It is now a white dwarf that slowly cools down (bottom left in Figure 1.3). This is the end of the evolution of a low-mass star.

In more massive stars there is no helium flash because the temperatures needed for helium fusion are reached before the electrons degenerate. The star burns first helium in the core and, as the star gets hotter and collapses, heavier elements with shell burning surrounding the core. Once iron is reached in this process, further fusion needs energy instead of producing it. If the core is heavy enough, electron degeneracy cannot prevent a collapse causing the star to explode in a supernova leaving a neutron star or a black hole. Some stars are even thought to get destroyed totally (e.g. Unsöld & Baschek 2002). During the supernova explosion large amounts of mass are ejected into the interstellar medium. This material is enriched with heavy elements. It eventually mixes with gas clouds creating a pool from which a new generation of stars and planetary systems can form.

1.4 Remarks on the structure of this work

In Chapter 2, observations, models, and concepts concerning young stars and their environment that are important for this thesis are detailed. The observations and the data reduction are described in Chapters 3 and 4, while Chapter 5 presents the theories and methods employed in this work. Chapter 6 contains the results and their discussion. Finally, Chapter 7 gives a summary of the findings of this thesis and an outlook on further research ideas following from this project.

Chapter 2

T Tauri Stars and Their Environment

This chapter gives an overview of T Tauri stars, the young pre-main-sequence (PMS) objects already mentioned in Section 1.1, and their environment. T Tauri stars are low mass ($M_* < 3M_\odot$, e.g. Appenzeller & Mundt 1989), cool stars with a convective envelope. They encompass the spectral types F to M. Traditionally, the T Tauri stars are divided into two subgroups based on a spectroscopic signature, their H α equivalent width (EW). Stars with an H α EW larger than 10 Å are called classical T Tauri stars (CTTS), those with a lower one weak-lined T Tauri stars (WTTS). Barrado y Navascués & Martín (2003) suggest that the dividing EW should depend on the spectral type and be higher for later type stars. TTS are variable objects and their spectra change over time. Often, the H α EW fluctuates around the dividing line. In a more physical definition, the CTTS are objects which actively accrete material from a circumstellar disk, while in WTTS the accretion process has already stopped and the disk is thin or even completely dissolved. These objects are therefore sometimes called naked TTS (NTTS).

More massive PMS objects of spectral type A or B with emission lines are called Herbig Ae/Be stars (see e.g. the review by Waters & Waelkens 1998). The accretion mechanism for these stars may be different, because they do not have a convective envelope and cannot generate magnetic fields in a solar-like dynamo. Even more massive O-type stars cannot be observed in a phase similar to the TTS, because they evolve so fast that they have already reached the main sequence by the time the molecular cloud reveals them.

This thesis concentrates on CTTS. Observational characteristics are presented in Section 2.1, while the current theoretical model for accretion onto CTTS is described in Section 2.2. The gas and the dust in the disk cause reddening as discussed in Section 2.3.

2.1 Observational characteristics

The central star of a CTTS system is in many aspects similar to a main-sequence analogue of the same spectral type. Young stars are typically more active manifesting in a higher level of X-ray activity and stronger chromospheric lines. The defining characteristic of CTTS is their photometric variability that has been observed at most wavelengths with time scales as short as hours and even minutes (e.g. Joy 1945; Bouvier et al. 1993; Gahm et al. 1995). The variability of the spectral emission features typical for these objects has also been widely studied (e.g. Johns & Basri 1995a; Alencar et al. 2001; Bouvier et al. 2007) revealing variations in their shapes and line strengths. Especially the hydrogen Balmer lines show a complicated kinematic line structure often including blue-shifted and/or red-shifted absorption components (e.g. Reipurth et al. 1996). These lines exhibit quite large full widths at half maximum (FWHM) suggesting that parts of the gas are moving at hundreds of km s^{-1} relative to the sources.

2.1.1 Disk and outflows

CTTS are still surrounded by circumstellar disks manifesting in an IR excess. These disks do not reach down to the stellar surface, but are truncated at a few stellar radii. Eisner et al. (2006) proved this for the well-studied CTTS TW Hya using near-infrared interferometry. The stellar radiation heats the upper layers of the disk to about 2500 K. The heating by Ly α radiation excites molecular hydrogen to the rotational-vibrational states. The decay of these states is observable in the UV and FUV (Herczeg et al. 2002, 2004). In IR observations of several stars, molecular hydrogen has been detected further out from the star (Beck et al. 2008), although it is not clear whether this emission comes from the disk or a wind.

In the disks of CTTS planet formation is expected to take place. The variability of the star interferes with the usual methods to detect planets. In 2008, Setiawan et al. announced the detection of a planet orbiting TW Hya, but this could not be confirmed by other authors (Rucinski et al. 2008; Huélamo et al. 2008). Recently, a possible transiting planet orbiting a WTTS has been detected (van Eyken et al. 2012). Radio observations provide evidence that dust grains in the disk around older CTTS have grown to pebbles with sizes of the order of a few cm (Testi et al. 2003; Rodmann et al. 2006). Even more complex materials like crystalline silicates have been found in the disk of CTTS (Schegerer et al. 2006).

CTTS can drive several types of outflows. A cool wind is observable in forbidden optical lines (Lamzin et al. 2004). The origin of this wind is the disk and most likely also the star itself. The blue-shifted absorption components often observed in the hydrogen emission features are most likely produced by this wind (e.g. Hartmann et al. 1990). The He I line at 10 830 Å is often used to study winds in CTTS. Edwards et al. (2003, 2006) detect a relationship between the wind acceleration and the accretion, showing that the inflow is most likely needed to power the outflow. Spectro-astrometric observations by Whelan et al. (2004) in the Pa β line revealed that some of the emission in the line wings has a measurable offset with respect to the central star. This emission is interpreted as originating in outflowing gas.

Some CTTS, like DG Tau and RW Aur, develop a jet, a highly collimated often bipolar outflow. Within the jet, several “knots” are formed, regions where the gas is heated by internal shocks. These knots radiate in optical lines, mostly H α , and are called Herbig-Haro (HH) objects. The jets typically extend a few hundred AU, but several jets with extensions of more than a parsec from the star are also known (McGroarty & Ray 2004). The material in the jets can reach velocities of up to 600 km s⁻¹, where the faster components are more collimated than the slower ones (Bacciotti et al. 2000). These jets produce X-ray emission, both close to the star (e.g. Schneider & Schmitt 2008) and further away (e.g. Güdel et al. 2005, 2008).

The composition of the outflows of CTTS remains uncertain. Their gas-to-dust ratio could be different from the interstellar medium. There are several possible driving mechanisms for winds and outflows that have different launching regions. A warm (\sim 2000 K), molecular, wide-angle outflow can be launched by the disk (Takami et al. 2004), the temperatures in the stellar wind might be higher.

With the material from the disk CTTS also accrete angular momentum. Nevertheless, they rotate far below their break-up velocity. The outflows are a promising process to extract angular momentum from the system.

2.1.2 Accretion

CTTS exhibit strong magnetic fields on their surface that cover a large portion of the photosphere. The average surface field can reach strengths of a few kG, e.g. 2.6 ± 0.3 kG on BP Tau (Johns-Krull et al. 1999). Similar fields have been found on other CTTS (e.g. Valenti & Johns-Krull 2004; Yang et al. 2005), but some stars do not show a field with large scale order. A simple dipole cannot explain the observations, higher order components are required (Donati et al. 2007).

The stellar magnetic field truncates the disk at a few stellar radii, around the co-rotation radius.

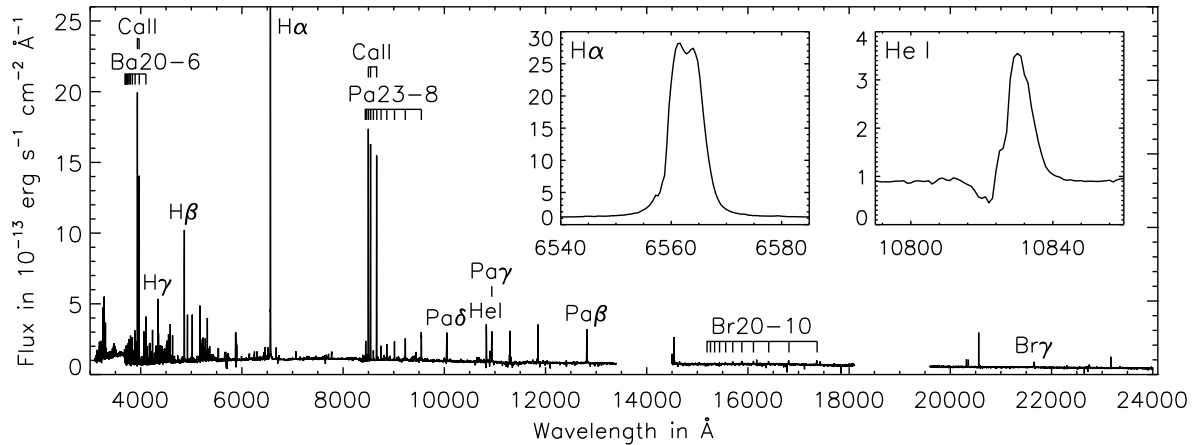


Figure 2.1: The VLT/X-Shooter spectrum of RU Lup annotated with important emission lines. The insets show the line profiles of H α and He I 10 830 Å.

The inner rim of the disk gets ionised by the stellar radiation and due to the Lorentz force the matter follows the field lines, forming accretion funnels. The infalling material reaches the star at the foot points of the accretion funnels, where a strong accretion shock forms (see also below). The radiation from the funnels and the accretion shock gives rise to a spectrum rich in emission lines, mainly from hydrogen, but also from other elements like helium and calcium. Figure 2.1 shows, as example, the spectrum of RU Lup.

The Balmer series, Pa β , and Br γ line profiles are often used to study the accretion geometry (Muzerolle et al. 1998a,b; Lawson et al. 2004). While the Balmer lines often show blue-shifted absorption features, these are not present in the infrared lines, which have lower opacities than the former ones (Folha & Emerson 1998). The infrared lines seem also to correlate with the accretion rates inferred from the blue continuum excess (Gullbring et al. 1998, 2000; Muzerolle et al. 2001). This is seen as evidence that the hydrogen emission and the blue excess are directly related to the accretion activity.

Although we now have a good understanding of the origin of the hydrogen emission features, the physical conditions in the emitting gas (e.g. ionisation state, level populations, temperature, and density) are still only rudimentary understood (e.g. Alencar & Basri 2000; Whelan et al. 2004; Eisner 2007). Muzerolle et al. (2001) model line fluxes and profiles dependent on the mass accretion rate \dot{M}_{ac} and a range of gas temperatures. They find that the temperature in the accreting gas has to be between 6000 K and 12 000 K, for higher mass accretion rates lower temperatures are found, to explain observational diagnostics like profile shapes, line ratios, and continuum emission. They also compared observed Pa β /Br γ line ratios to the predictions for optically thin and thick gas in LTE as well as the case B approximation of hydrogen recombination line theory (Storey & Hummer 1995, and references therein), but find that neither of these models provides a good match. In most cases these comparisons used non-simultaneous data. The infrared hydrogen line fluxes are variable on time scales as short as hours (e.g. Johns & Basri 1995b; Alencar et al. 2001; Bouvier et al. 2007). Thus, line ratios calculated from observations taken at different times will likely be misleading and fail to provide constraints on the physical conditions in the gas.

Bary et al. (2008) simultaneously observed the Paschen and Brackett series of a sample of 15 CTTS at low resolution ($R \simeq 300$) to improve on the previous comparisons. The measured line flux ratios of Pa n_{up} to Pa β , where n_{up} is the upper level of the transition, and Br n_{up} to Br γ show a relatively small scatter even though they are comprised of data from many different sources with a broad range of mass accretion rates \dot{M}_{ac} and multiple epochs of observations of the same source. The ratios seem to be insensitive to variations in \dot{M}_{ac} , motivating Bary et al. (2008) to use a “global” line ratio for each ratio included in their analysis of the average conditions in the gas. The global line ratios, representative for all stars in their survey, are the average value for

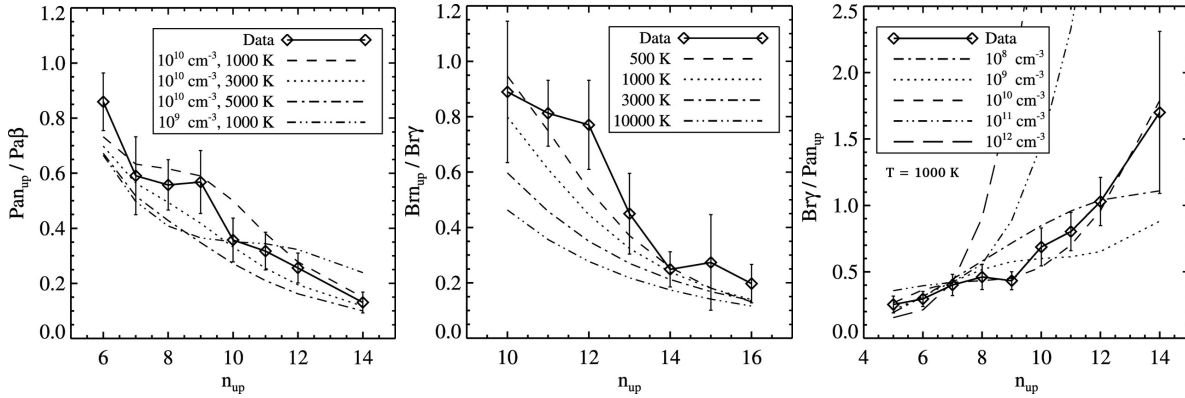


Figure 2.2: The measured line flux ratios and the calculated case B models from Bary et al. (2008): The Paschen decrements $Pan_{up}/Pa\beta$ and the four models with smallest reduced χ^2 (left, $T = 1000 \text{ K}$ and $n_e = 10^{10} \text{ cm}^{-3}$ is the best-fit model), the Brackett decrements $Brn_{up}/Br\gamma$ and four models with $n_e = 10^{10} \text{ cm}^{-3}$ and varying temperature T (middle, $T = 500 \text{ K}$ and $T = 1000 \text{ K}$ are the best-fit models) as well as the line ratios $Br\gamma/Pan_{up}$ and four models with $T = 1000 \text{ K}$ and varying electron density n_e (right, $n_e = 10^{10} \text{ cm}^{-3}$ is the best-fit model).

each line ratio weighted by the uncertainty. These global line ratios are statistically well fitted by the case B models of Storey & Hummer (1995) (see also Section 5.2) constraining the temperature in the emitting gas to $T \lesssim 2000 \text{ K}$ and the electron density to $10^9 \text{ cm}^{-3} < n_e \lesssim 10^{10} \text{ cm}^{-3}$. Figure 2.2 shows their data for the ratios $\frac{Pan_{up}}{Pa\beta}$, $\frac{Brn_{up}}{Br\gamma}$, and $\frac{Br\gamma}{Pan_{up}}$ along with case B models. Case A was not considered in their analysis since it is only appropriate for very low density environments and not for the gas in the inner regions of accreting CTTS (Osterbrock 1989). They also compare their data to the optically thin and thick LTE cases, finding no agreement for any temperature, providing evidence that the level populations in the hydrogen gas are not in LTE. While Bary et al. (2008) used global line ratios to study the average conditions in the emitting gas, in Sections 6.1 and 6.2 I examine the line ratios of several CTTS individually to infer temperature and density.

The fraction of the stellar surface covered by the foot points of the accretion funnels, where the infalling material reaches the star, i.e. the surface filling factor f , is typically a few percent or less (e.g. Donati et al. 2007). A strong shock forms on the stellar surface converting most of the kinetic energy of the material to heat. The temperatures in the post-shock gas reach a few 10^6 K . The gas cools down radiatively after it passed the shock front. This radiation is observable in several spectral bands, most prominently in X-rays. Not all of the cooling radiation escapes the post-shock cooling zone. Instead it heats the underlying photosphere generating an additional continuum from the UV to the IR that increases the level of the stellar emission continuum. In a continuum normalised spectrum the spectral absorption lines seem less deep relative to a main-sequence star of the same spectral type. This effect is called “veiling”. It is also a diagnostic for the mass accretion rate.

2.2 The magnetically funnelled infall model

The magnetically funnelled infall model for CTTS was introduced by Uchida (1983) and Koenigl (1991) to solve some problems of the previously preferred boundary layer model. In the boundary layer model the disk was thought to reach down to the stellar surface. Shu et al. (1994) developed the magnetically funnelled infall model further into the X-wind model for the accretion along dipolar field lines where a wind is driven from the inner disk rim simultaneous to the accretion. For a simple dipole configuration of the magnetic field, the infall impacts the stellar surface at high latitudes. Figure 2.3 shows a sketch of the geometry following the magnetically funnelled infall model. If the field is rotationally symmetric, the accretion spot will take the

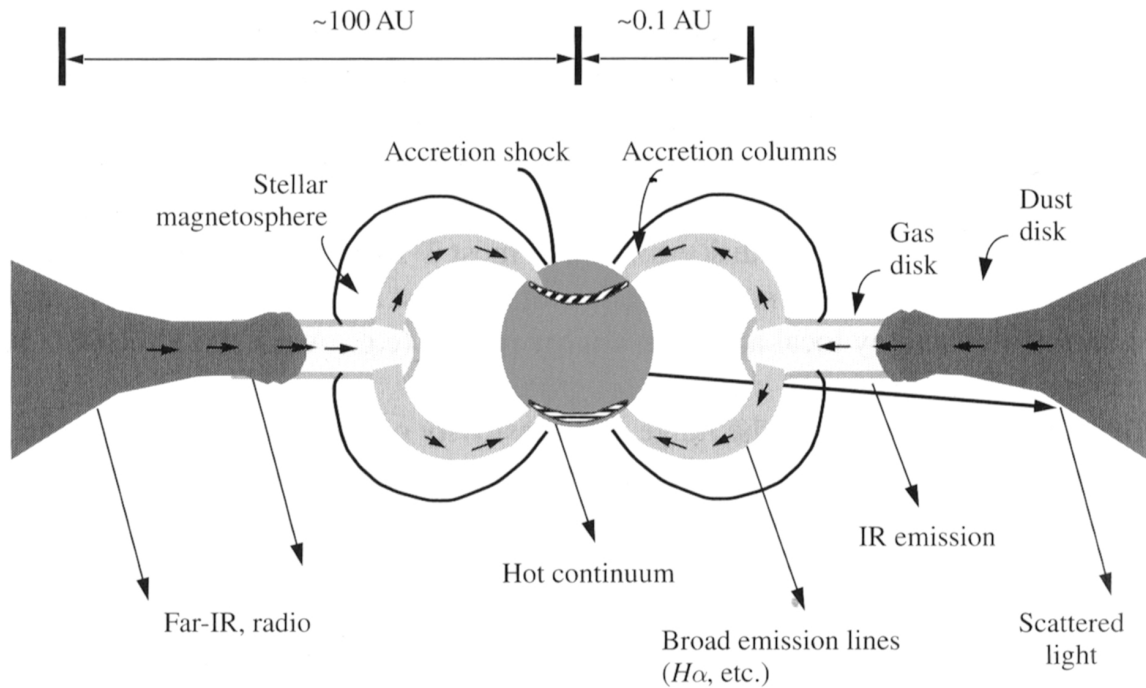


Figure 2.3: A not true to scale sketch of the model of disk accretion in CTTS (Hartmann 2009).

form of a ring at constant latitude, but the photometric variability of CTTS shows that the funnels impact in distinct spots for most stars.

The stellar magnetic field controls the large-scale accretion geometry. In reality the field is complex, but with increasing distance from the star the contributions of higher-order multi-pole components to the field strength decrease faster than those of the dipolar field. The first simulations of the full magneto-hydrodynamic equations for the region from the inner disk rim to the stellar photosphere therefore used dipolar fields (Romanova et al. 2004). They investigated an inclination between the axis of rotation and the symmetry axis of the magnetic field. For more complex fields, different modes of accretion are possible. Long et al. (2007) use a combination of a dipole and quadrupole field, finding that emission might occur simultaneously in hot spots at high latitudes and in the equatorial region.

A complementary approach is the extrapolation of the magnetic field which is reconstructed with Zeeman Doppler imaging. The magnetic field lines can be calculated for a simple set of boundary conditions and an assumed field configuration. Some of the field lines thread the disk, potentially carrying the accretion stream. The foot points of the field lines are not all concentrated at higher latitudes, but scattered over the stellar surface (Gregory et al. 2006; Jardine et al. 2008).

The velocity the material reaches when it impacts the star, is essentially given by the free-fall velocity, as confirmed by advanced simulations, although some accretion funnels may be slowed down before the impact and lose kinetic energy to the magnetic field. The material reaching free-fall velocity explains the large velocities observed for the hydrogen emission lines and also the red-shifted absorption components in their line profiles. Calvet & Gullbring (1998) simulated the gas dynamics in a simple one-dimensional geometry of the accretion spot and a stationary post-shock cooling zone finding that the underlying photosphere is heated to about 20 000 K. This temperature is large enough to explain the veiling and UV continuum excess observed in CTTS. These models allow observations of the Balmer and Paschen continua to be converted into an estimate of the mass accretion rate. A similar model for the high-energy emission was developed by Lamzin (1998). Günther et al. (2007) present simulations of X-ray spectra of CTTS including also the contribution of the stellar corona to the high-energy emission.

The magnetically funnelled infall model has been used by several authors to predict the fluxes and line profiles of optical and infrared hydrogen emission features (Hartmann et al. 1994; Muzerolle et al. 1998a,b). In these models most of the emitting gas is confined to the accretion columns and not in an outflowing wind, while the models by Kurosawa et al. (2006) also include the emission by winds.

When analysing hydrogen lines of CTTS, it is very important to keep in mind the different contributions to both the emission and the absorption mentioned above. Kurosawa et al. (2006, 2011) had to combine the magnetospheric accretion model with wind models to reach qualitative agreement with observations, e.g. the H α line profile catalogue and classification scheme by Reipurth et al. (1996) or the sample of line profiles of Pa γ and the He I line at 10 830 Å by Edwards et al. (2006). Four regions contribute to the formation of the lines: a central continuum source, composed of the star itself and the emission of the accretion hot spots, the magnetospheric accretion flow, the wind outflows, and the accretion disk. While contribution of the emissivity of the disk to the H α continuum flux is neglected in their models, because the mass of the disk is very small and the temperatures are low, both the accretion flow and the outflows contribute to the observed emission in H α . The outflows are either a disk wind, where the outflow is launched from the disk through open field lines over a range of distances from the star, or a stellar wind, arising from the polar region and propagating radially. In reality, a combination of the two is likely. The line profiles are complicated by blue shifted absorption and a redward asymmetry from the wind and red-shifted absorption by the accretion funnels. With changing inclination the strength of the different absorbing contributions changes, as some accretion funnels can be blocked by the photosphere or the inner disk. These models also reproduce the observational result that the near-infrared hydrogen lines are less affected by the outflows (e.g. Folha & Emerson 2001; Edwards et al. 2006), i.e. the line profiles show no blue-shifted absorption features, only the red-shifted absorption component from the accretion funnels.

While Kurosawa et al. (2006, 2011) use a black-body radiation model with a single temperature for the emission of the hot spots, the spots also produce emission in lines (e.g. Dodin et al. 2012; Dodin & Lamzin 2012, and references therein), which adds another region contributing to the observed hydrogen emission lines.

From a time series of H α and H β line profile observations of TW Hya, showing signatures of inflow and variable outflow, Dupree et al. (2012) conclude that these lines originate in the post-shock cooling region. They suggest that this region dominates the formation of the H α line profile and not the accretion stream as frequently assumed in the magnetically funnelled infall model. Additionally, they point out that the chromosphere might also play a significant role for the formation of H α . The chromosphere and the post-shock cooling region are not taken into account as contributors to the H α line profiles in most models, e.g. those by Muzerolle et al. (2001).

2.3 Reddening and dust

Reddening is caused by extinction, i.e. the absorption and scattering of light by dust and, to a lesser extent, gas between the emitting object and the observer. In fact, the existence of interstellar dust was inferred from the obscuration of stellar light via extinction (Trumpler 1930). Because dust absorbs and scatters blue light more strongly than red light, the stars appear redder than they are. Our knowledge of interstellar dust stems mostly from studies of the wavelength-dependence of the extinction. The wavelength-dependence itself constrains the grain size distribution. The dust grains in the interstellar medium have sizes varying from molecules to a few tenth of a μm . Spectral features in the extinction reveal the chemical composition.

The extinction is typically determined using the pair method, i.e. comparing the spectrophotometry of two stars of the same spectral type. One of the stars has to have negligible foreground dust, while the other is reddened. Assuming that dust extinction goes to zero at very long wavelengths, the extinction $A_\lambda \equiv 2.5 \log_{10} \frac{F_\lambda^0}{F_\lambda}$ as a function of the wavelength λ can be determined,

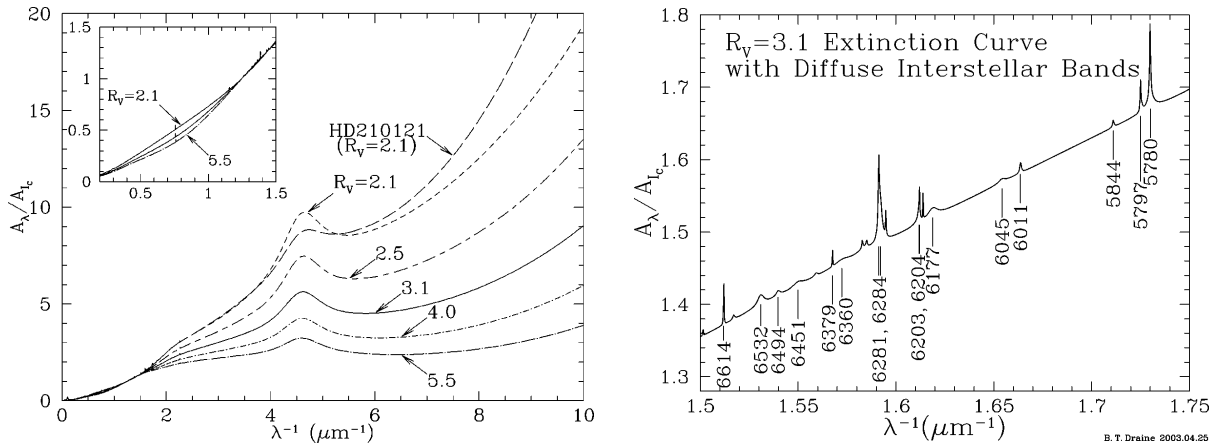


Figure 2.4: Normalised extinction curves using the parametrisation of Fitzpatrick (1999) for different R_V (left) and diffuse interstellar bands in the 5700 Å to 6670 Å region (right), using DIB parameters from Jenniskens & Desert (1994) (Draine 2003).

where F_λ is the observed flux and F_λ^0 is the unreddened flux, i.e. in absence of extinction. The spectral type of CTTS is usually not well determined. Additionally, for the determination of the extinction towards these objects, the veiling (see Section 2.1.2) needs to be known. Sections 6.3 and 6.4 deal with finding a way to determine the extinction towards CTTS without needing exact knowledge about the object and its veiling employing hydrogen lines with a common upper level.

The parameter $R_V = \frac{A_V}{A_B - A_V}$, where A_V and A_B are the extinction in the B and V filter bands, is commonly used to measure the slope of the extinction curve in the optical region. The extinction produced by very large grains would result in $R_V \rightarrow \infty$, while Rayleigh scattering, i.e. $A_\lambda \propto \lambda^{-4}$, would cause very steep extinction with $R_V \approx 1.2$. In the Milky Way the mean extinction is characterised by a diffuse cloud with $R_V \approx 3.1$ (Schultz & Wiemer 1975), but the extinction can vary between 2.1 (Welty & Fowler 1992) and 5.6 to 5.8 (Cardelli et al. 1989; Fitzpatrick 1999) for different lines of sight. Sight lines that intersect clouds with larger extinction per cloud seem to have larger values of R_V . This may indicate grain growth by accretion and coagulation (Draine 2003).

The normalised extinction curve $\frac{A_\lambda}{A_I}$, where the *I* band extinction ($\lambda \approx 9000$ Å) is used for normalisation, can be approximated by a function of wavelength with seven parameters (Cardelli et al. 1989). For wavelengths larger than 3030 Å, this function depends only on the wavelength λ and the parameter R_V . If R_V is known the other parameters can be estimated and the UV-optical extinction can be approximated by a one-parameter family of curves. In the infrared, empirical extinction curves of diffuse clouds show only little variation. For wavelength between 0.7 μm and 8 μm and diffuse clouds, the function found by Cardelli et al. (1989) appears to be independent of R_V . Fitzpatrick (1999) derived an improved parametrisation. Figure 2.4 (left) shows extinction curves calculated from the Fitzpatrick (1999) parametrisation for $R_V = 2.1, 2.5, 3.1, 4.0,$ and 5.5 . The coefficients of the parametrisation can be adapted to improve the fit to a specific sight line. In Figure 2.4 (left) this is shown for the early B-type star HD 210121. Here, the UV extinction significantly differs from the average behaviour for the same value of R_V .

The infrared extinction curve between 0.9 μm and 5 μm can be approximated by a power-law, $A_\lambda \propto \lambda^{-\alpha}$. Various studies found different values for the exponent α . Reported values include $\alpha \approx 1.61$ (Rieke & Lebofsky 1985), 1.7 (Whittet 1988; Bertoldi et al. 1999; Rosenthal et al. 2000), 1.75 (Draine 1989), or ~ 1.8 (Martin & Whittet 1990; Whittet et al. 1993). The extinction in this region will be further described in Section 5.3, while in Sections 6.3 and 6.4 the shape of the reddening law will be studied using hydrogen lines with a common upper level.

In the region 5 μm to 8 μm ambiguous results for the extinction have been found. While Draine

(1989), Bertoldi et al. (1999), and Rosenthal et al. (2000) find that the extinction continues to decrease with increasing wavelength to a minimum at $\sim 6 \mu\text{m}$, Lutz et al. (1996) do not find a decline in extinction towards Sgr A* for the region $4 \mu\text{m}$ to $8 \mu\text{m}$.

This shows that extinction is still poorly understood. It varies significantly between different sight lines and many details for a comprehensive model are still missing.

Another way to examine the extinction uses star counts or galaxy counts as a function of apparent brightness. From *UBVRI* photometry of Galactic field stars in high-latitude clouds, Szomoru & Guhathakurta (1999) find $R_V \lesssim 2$, much lower than the average $R_V \sim 3.1$. From *V* and *I* photometry of red clump giants, Udalski (2003) deduces $R_V \sim 3.1$ towards the LMC, while $R_V \sim 1.8 - 2.5$ towards the Galactic bulge regions, prompting him to suggest that the extinction is anomalous towards this regions.

The continuous extinction is modified by several strong absorption features that reveal the chemical composition of the interstellar dust grains. The most prominent feature is a ‘‘bump’’ at 2175 \AA whose origin is not fully understood. Models to explain this feature include small graphite particles (Stecher & Donn 1965), organic carbon and amorphous silicates, or organic molecules (e.g. polycyclic aromatic hydrocarbons, PAHs) in the grains (Bradley et al. 2005). At $3.1 \mu\text{m}$ there is a feature produced by ice in molecular clouds, a hydrocarbon feature at $3.4 \mu\text{m}$, several PAH absorption features between $3 \mu\text{m}$ and $12 \mu\text{m}$ with the most prominent at $6.2 \mu\text{m}$, and at $9.7 \mu\text{m}$ and $18 \mu\text{m}$ features by silicates. In addition, there are the so-called diffuse interstellar bands (DIBs, Fig. 2.4 *right*), of which more than 400 are known (Hobbs et al. 2009), mainly found in the optical and near-infrared. Their origin is unknown so far, but the presence of substructures inside DIB profiles points towards a molecular origin (Galazutdinov et al. 2002). In this thesis I aim to find further features in the near-infrared.

The so-called extended red emission (ERE) from dust grains likely also offers some insight into the composition of interstellar dust. The ERE is a broad featureless emission band between 5400 \AA and 9000 \AA that peaks between 6100 \AA and 8200 \AA and has a FWHM of 600 \AA to 1000 \AA . The exact appearance of this features varies for different regions. Although the ERE has been observed in various dusty environments and has been ascribed to photoluminescence, the material producing them is still uncertain. The interstellar dust additionally produces emission in the infrared and far-infrared, where most of the radiated power is at wavelengths larger than $50 \mu\text{m}$ (Draine 2003). Other means to study the composition of dust are presolar grains in primitive meteorites, interstellar dust entering the solar system, and dust grains released by comets (see e.g. Draine 2003).

Over the past decades several grain models have been developed. Mathis et al. (1977) reproduce the average interstellar extinction with a model containing graphite grains and silicate grains. Both components have a power-law particle-size distribution $n(a) \propto a^{-3.5}$, where a is the size of the grains. The size distribution is truncated at a minimum size of $a_{\text{min}} \approx 50 \text{ \AA}$ and a maximum size of $a_{\text{max}} \approx 2500 \text{ \AA}$. These models were developed when the importance of PAHs for the interstellar grain material was unknown. The graphite-silicate models have since been extended. Very small carbonaceous grains are assumed to be PAH molecules. Grains larger $\sim 0.01 \mu\text{m}$ (containing $N \gtrsim 10^6$ C atoms) have the physical and chemical properties of bulk graphite. With increasing grain size, the properties of the carbonaceous grains are considered to vary smoothly from PAH-like to graphite-like (Draine 2003).

Figure 2.5 shows the size distribution of carbonaceous and silicate grains that Weingartner & Draine (2001) find for average Milky Way dust with $R_V = 3.1$. The distribution for carbonaceous grains has a trimodal shape: The first peak at $a \approx 5 \cdot 10^{-4} \mu\text{m}$ is required to reproduce the PAH emission features at wavelengths between $3 \mu\text{m}$ and $12 \mu\text{m}$. The second peak at $a \approx 5 \cdot 10^{-3} \mu\text{m}$ is needed to match the observed emission near $60 \mu\text{m}$. The third peak at $a \approx 0.3 \mu\text{m}$ is necessary to reproduce the observed extinction curve. The model does not contain a component that creates the observed hydrocarbon feature at $3.4 \mu\text{m}$. Draine (2003) points out that substituting the graphite in the $a \gtrsim 200 \text{ \AA}$ carbonaceous grains with a mix of graphite and hydrocarbons and slightly adjusting the grain size distribution will likely reproduce the extinction curve, including

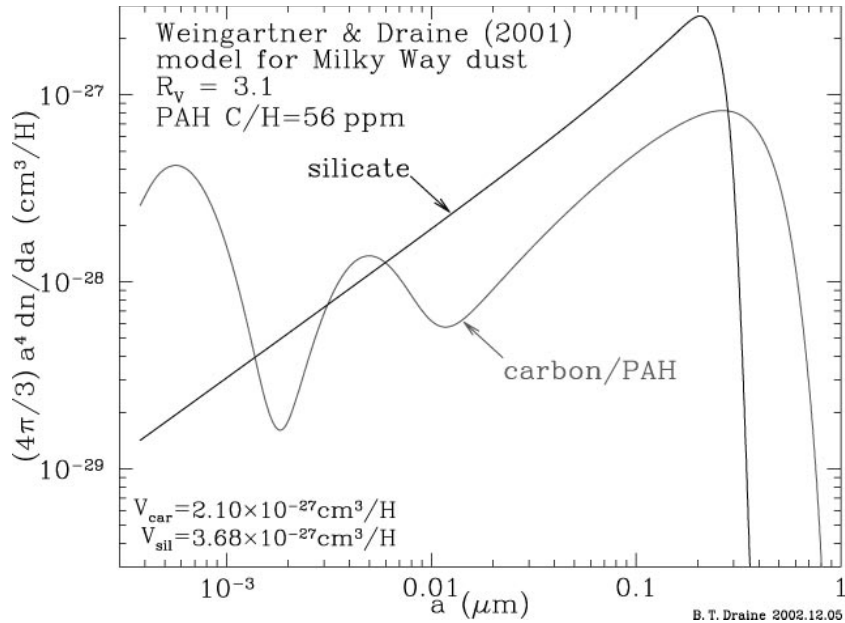


Figure 2.5: The size distributions for the carbonaceous-silicate grain model of Weingartner & Draine (2001) for Milky Way dust with $R_V = 3.1$ (Draine 2003).

the $3.4 \mu\text{m}$ feature.

For CTTS, the material responsible for the extinction resides mainly in the immediate environment of the star and consists of the remaining dust and gas from the natal cloud. The composition of the material might be different from that of average interstellar dust. Examining the shape of the reddening law towards different objects might help to shed light on this and is one goal of this thesis (see Sections 6.3 and 6.4).

Chapter 3

Observations and Data Reduction

The spectroscopic data used in this thesis were taken with the VLT/X-Shooter instrument, described in Section 3.1, during the nights of 2010 May 3/4 and 4/5 in visitor mode. The observations were carried out by J. Robrade, Hamburger Sternwarte, under programme ID 085.C-0764(A) (PI H. M. Günther, then Hamburger Sternwarte, now Harvard-Smithsonian Center for Astrophysics). The observed sample of young stellar objects is introduced in Section 3.2. Most of the data reduction is carried out using the pipeline provided by ESO and is described in Section 3.3. For the flux calibration the pipeline can not be used and I carry it out myself as detailed in Section 3.4. Additional reduction steps are described in Section 3.5. The removal of telluric lines will be described in a separate chapter (Chapter 4).

3.1 The instrument: VLT/X-Shooter

X-Shooter (Vernet et al. 2011; ESO 2010) is a multi-wavelength medium-resolution spectrograph mounted at the Cassegrain focus of one of the unit telescopes (UT) of the Very Large Telescopes (VLT) of the ESO Paranal Observatory in Chile. At the time of observations X-Shooter was mounted at UT2 “Kueyen” that has a mirror diameter of 8.2 m, like all UTs.

X-Shooter takes a spectrum of a single target in the spectral range from the UV to the K band (3000–25000 Å) in one single exposure reaching resolutions between 4000 and 14 000, depending on wavelength and slit width. To reach high efficiencies over the large wavelength range, X-Shooter consists of three distinct arms. Each arm is an independent cross-dispersed echelle spectrograph equipped with optimised optics, dispersive elements, and detectors. Two dichroic beam splitters and accompanying optic elements split the light beam from the telescope and distribute it to the arms. The three arms are labelled UVB, covering 3000–5900 Å, VIS, covering 5400–10 100 Å, and NIR, covering 9900–24 700 Å. During the reduction process the coverage of the NIR arm is split into three parts (9900–13 400 Å, 14 500–18 100 Å, and 19 600–24 700 Å, respectively) omitting the regions lost due to heavy telluric contamination (see Chapter 4). Besides slit spectroscopy, X-Shooter also offers spectroscopy using an integral field unit (IFU). The IFU used for X-Shooter is an image slicer that re-images the input field of $4'' \times 1.8''$ into a slit of $12'' \times 0.6''$.

The observations were taken in slit nodding mode, the standard observational strategy for near-infrared observations. The telescope nods between two positions A and B along the slit to enable sky subtraction, which is described in Section 3.3. The slit widths are $0.5'' \times 11''$ for the UVB arm and $0.4'' \times 11''$ for the VIS and NIR arms resulting in a resolution of $R \sim 18 000$ in the VIS arm and $R \sim 10 000$ in the UVB and NIR arm. The exposure times and the number of exposures per nodding position are summarised in Table 3.1.

Additionally, the two flux standard stars EG 274 and GD 153 were observed in offset mode with a $5.0'' \times 11''$ slit in all arms. The exposure times were 90 s in the UVB arm and 120 s in the VIS and NIR arm for EG 274 as well as 600 s in all arms for GD 153.

Table 3.1: The sample and observational details.

Object (1)	SpT (2)	Ref. (3)	$\log \dot{M}_{ac}^a$ in		Exposure time in s			Exposures per nodding position		
			$M_{\odot} \text{ yr}^{-1}$ (4)	Night (5)	UVB (6)	VIS (7)	NIR (8)	UVB (9)	VIS (10)	NIR (11)
S CrA	G5+K5	1	-6.5	2	150	30	50	2	4	6
TW Hya	K7	6	-7.9	1	150	60	100	2	4	6
EX Lup	M0	2	-9.7	1	150	60	100	2	4	6
GQ Lup	K9	2	-7.8	2	200	80	120	2	4	6
HO Lup	M1	2	-8.5	1	300	140	150	2	4	6
IM Lup	M0	2	-10.2	1	150	60	100	2	3	5
MV Lup	K2	5	^b	2	150	60	100	2	4	6
RU Lup	G5	5	-7.8	1	150	60	100	2	4	6
MP Mus	K1	5	-8.7	1	150	60	100	2	4	6
V853 Oph	M4	7	-9.2	1	200	80	120	2	4	6
V2058 Oph	K5	7	-7.8	1	300	140	150	2	4	6
V2062 Oph	K3	4	-7.9	1	300	140	150	2	4	6
V2129 Oph	K5	7	-9.5	1	200	80	120	2	4	6
V2251 Oph	K5	6	-7.9	1	300	140	150	2	4	6
V2252 Oph	M0	6	-8.5	2	300	140	150	2	4	6
VV Sco	M1	5	-8.8	2	200	80	120	2	4	6
V895 Sco	K5	6	-7.1	2	300	140	150	2	4	6
V1279 Sco	M0	2	-9.0	2	300	140	150	2	4	6
V4046 Sgr	K6	3	-8.5	1	150	60	100	2	4	6
Sz77	M0	2	-10.1	2	200	80	120	2	4	6

References for spectral type. (1) Carmona et al. (2007); (2) Hughes et al. (1994); (3) Torres et al. (2006); (4) Ricci et al. (2010); (5) SIMBAD Astronomical Database; (6) Herbig & Bell (1988); (7) Wilking et al. (2005).

Notes. (a) determined from the $H\alpha$ emission line width (see text); (b) has no $H\alpha$ in emission.

3.2 The sample

The 20 objects in the sample, summarised in Table 3.1, are young stellar objects that were selected from several star forming regions on the southern sky within 200 pc, mainly from the Lupus clouds and the Ophiuchus Molecular Cloud, based on their $H\alpha$ equivalent width. They cover different ages and thus evolutionary stages including the transitional phase between CTTS and WTTS. In column 4 of Table 3.1, I state the mass accretion rate \dot{M}_{ac} of the objects estimated from the width of the $H\alpha$ emission line at 10% of the maximum value, $H\alpha$ 10%, using the empirical relation by Natta et al. (2004), $\log \dot{M}_{ac} = -12.89 + 9.7 \cdot 10^{-3} H\alpha$ 10%. Table 3.1 also provides information on the exposure times and the number of exposures per nodding position used during the observation run.

3.3 Data reduction using the ESO pipeline

The ESO offers a dedicated data reduction pipeline (Modigliani et al. 2010) for the X-Shooter instrument. To reduce the data set described above the pipeline version 1.5.0 (ESO 2012) is used. Each arm is reduced individually following the standard steps of spectroscopic data reduction. First of all, several instrumental effects need to be corrected. The count rate the CCD detector shows at zero exposure time is called the bias. Its average is measured and subtracted. For the NIR arm the dark current created by the random generation of electrons in the CCD is measured

for each exposure time and subtracted. The flat field is an exposure of a slit using a continuum lamp. This provides information on the response of the detector and measures the efficiency of the CCD on different scales. The efficiency changes due to pixel-to-pixel variations on small scales. On intermediate scales, fringing affects the efficiency in the red. Fringing originates in interferences of the incident light and light that is reflected from the layers of the CCD structure. Finally, on large scales the efficiency is affected by the blaze function. The science observations are divided by the flat field to correct for these effects.

Next, the 2D CCD image needs to be transformed into a 1D spectrum. The locations of the echelle orders on the CCD are determined from an exposure of a pinhole illuminated by a continuum lamp. The wavelength calibration and the determination of the 2D transformation needed to rectify the X-Shooter spectral format is done using two exposures of an Thorium-Argon (ThAr) arc lamp, one of a slit and one of 9 pinholes. To account for small changes in the spectral format due to temperature, pressure, and instrument flexure associated to the telescope pointing, for each science exposure an additional pinhole exposure of an arc lamp is taken.

The science targets were observed in nodding mode. Here, exposures are taken in pairs at different positions A and B so that the object spectrum falls on different positions on the CCD. If several exposures are taken at each position, these are co-added before the difference frame A-B is determined to remove the contribution of sky emission and cosmic ray hits are corrected. The frame is divided by the flat field, rectified, and both spectra are then localised on the CCD. The difference frame B-A is determined, rectified, and shifted to the position of A. This procedure is repeated for all nodded pairs. Finally, all frames are combined into a single frame and the spectrum is extracted by summing the individual pixels.

The flux standard stars were observed in offset mode. Here, exposures are also taken in pairs, one with the object and one with sky only. The difference frame on-off is calculated to remove the contribution of sky emission. The inter-order background is estimated and subtracted. Cosmic ray hits are corrected, the frame is divided by the flat field, rectified, and the spectrum is localised on the CCD. Finally, the spectrum is extracted.

The data reduction is carried out using the default parameters except for a few occasions where I deviate from them to obtain better results. For example, in the recipe *xsh_2dmap*, which determines the 2D transformation, I change the parameter *detectarclines-findlines-center*. This parameter states the method used to find the arc lamp lines. The standard is 'gaussian'. I use 'barycenter', because only very few lines are detected using the standard value.

3.4 Flux calibration

The ESO pipeline can be used to determine a response curve to flux-calibrate the spectra. This flux calibration includes a correction for the atmospheric extinction via a tabulated extinction curve for the Paranal Observatory. The method I use to remove the telluric lines from the spectrum, described in detail in Chapter 4, uses a model of the transmission of Earth's atmosphere and also takes into account the atmospheric extinction. Applying the telluric line removal to flux-calibrated spectra would incorporate the atmospheric extinction twice. Therefore, I determine the flux calibration myself from spectra that are cleaned of telluric lines and corrected for the atmospheric extinction losses using the method described in Chapter 4.

3.4.1 Using the white dwarf standards

For each of the two nights one white dwarf standard star was observed for flux calibration purposes, GD 153 for the first and EG 274 for the second night. Both stars are part of the X-Shooter spectrophotometric standard stars catalogue (Hamuy et al. 1994; Vernet et al. 2010). The observed spectra are normalised to 1 s exposure time. The response curve is obtained by dividing the catalogued spectrum by the normalised observed spectrum. The response curve is smoothed to reduce the noise. For the NIR arm the spectra are more noisy and show residuals of sky emission lines that have not been removed properly during the reduction. To exclude portions

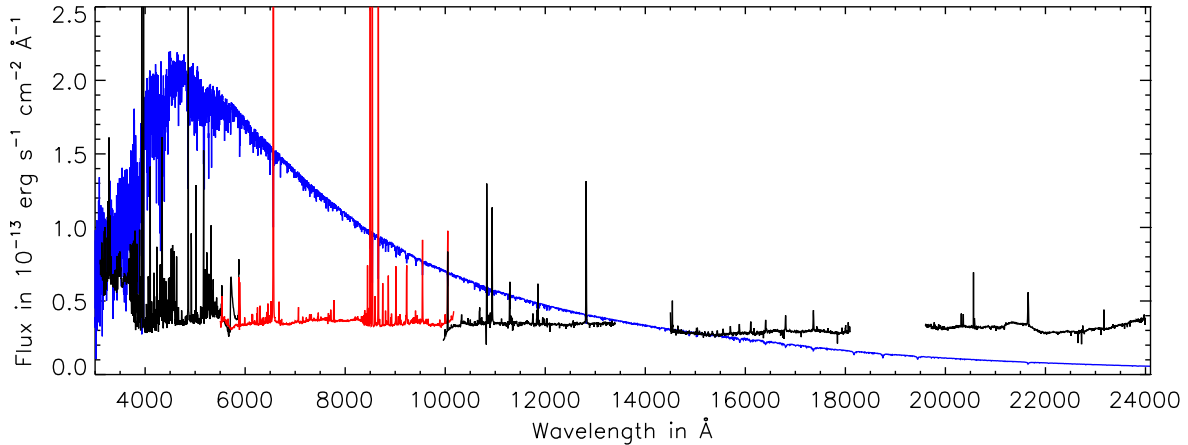


Figure 3.1: The tentative spectrum of RU Lup (G5, *black* UVB and NIR arm, *red* VIS arm), flux-calibrated using a white dwarf standard star, together with the scaled PHOENIX model with $T_{\text{eff}} = 5800$ K (*blue*).

of the spectrum that do not follow the overall shape of the spectrum, I use sigma-clipping. For GD 153 the NIR observation is underexposed so that despite all efforts no reasonable response curve could be determined. The difference between the response curves for each night of the other arms is very small, therefore the response curve determined for the NIR arm for the second night can also be used for the first night. To flux-calibrate a spectrum, the telluric line corrected spectrum is normalised to 1 s exposure and multiplied by the response curve.

Unfortunately, the resulting response curves do not produce correctly flux-calibrated spectra. The overall shape of a spectrum with a coverage as large as X-Shooter’s should show the underlying black body of the star. This is not the case as can be seen in Figure 3.1 for the tentative spectrum of RU Lup, a CTTS, and in Figure 3.2 for IM Lup, a WTTS. The observed spectra, flux-calibrated using the response obtained from the white dwarfs, are shown together with a model from the Göttingen Spectral Library by PHOENIX (Husser et al. 2013) appropriate for their spectral type. The model spectra are scaled to match the observed spectrum at $\sim 15\,000$ Å. Although the model spectra are unreddened, it is obvious that the apparent spectrum of RU Lup is very flat and the black body shape exists only approximately for IM Lup. Applying reddening to the model spectrum does not lead to a better match for IM Lup. For the CTTS, the flat shape could be produced by disk emission but according to the models of Robitaille et al. (2006) Class II objects should not be dominated by the disk at the wavelengths we are looking at. Hence, the reason for the atypical shape of the tentative spectra must be in the flux calibration. The flux standards were observed with a slit width of $5''$, but the science spectra were taken with $0.4''$ and $0.5''$, respectively. The response curve, as determined above, does not take into account the flux losses due to the smaller slit and therefore does not correctly reproduce the spectral shape. This problem is usually solved by observing the flux standard star twice, once with the broad slit to catch all the flux and once with the same slit width as the targets. This was unfortunately not done in this observation run.

To obtain a flux calibration nonetheless, the stars observed as telluric standards will be used as described in following Section 3.4.2.

3.4.2 Using the telluric standards

During the observation run 12 stars of spectral type late B were observed to serve as telluric standard stars. These are listed in Table 3.2. In total there are 14 spectra, with one star, HIP 079631, observed three times. Although their spectra are not as well understood as those of white dwarfs, they have a relatively simple shape enabling their use for flux calibration purposes. There are no catalogued reference spectra available for the late B stars that could be used to

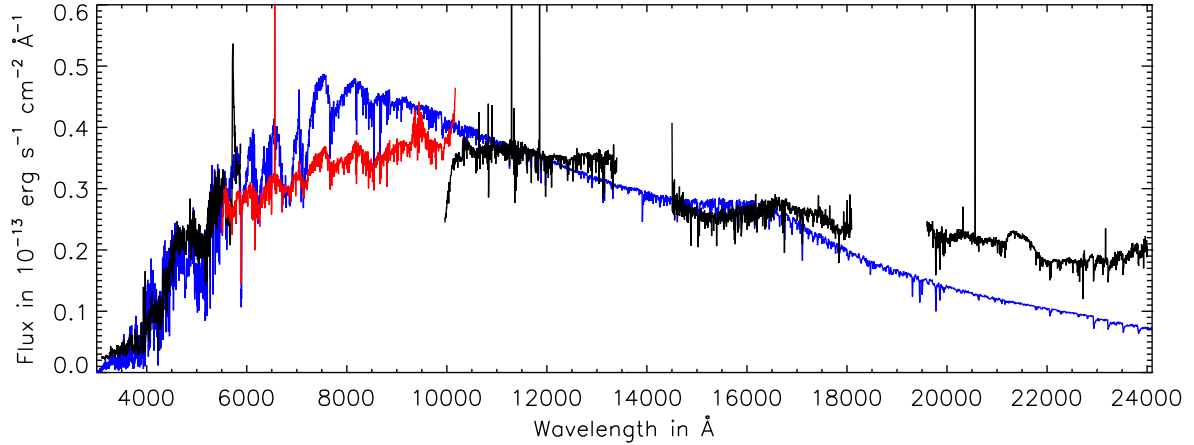


Figure 3.2: The tentative spectrum of IM Lup (M0, *black* UVB and NIR arm, *red* VIS arm), flux-calibrated using a white dwarf standard star, together with the scaled PHOENIX model with $T_{\text{eff}} = 3800$ K (*blue*).

determine the response in the same manner as for the white dwarfs. To overcome this I use model spectra from the Göttingen Spectral Library by PHOENIX and observed photometric data of the stars. Magnitudes are available from Tycho-2 (Høg et al. 2000) in B_T and V_T , from USNO B1.0 (Monet et al. 2003) in R , and from 2MASS (Skrutskie et al. 2006) in J , H , and K . The first step towards a flux calibration is the determination of the appropriate model spectrum for each star that provides the relative flux calibration, i.e. the shape of the spectrum. From the library, I take a subset of model spectra with $\log g = 4$, metallicity $[\text{Fe}/\text{H}] = 0$, and effective temperatures T_{eff} between 9000 K and 12 000 K (in steps of 200 K) to represent late B stars. Several approaches seem possible to find the appropriate model for each star from this subset: the equivalent width (EW) of the hydrogen lines, the Balmer jump, and the colours.

The EWs of the hydrogen lines in the model spectra decrease with increasing T_{eff} . Comparing the observed EWs to the model EWs does not lead to a clear determination of the appropriate model spectrum, because the observations do not follow the model trends. Another approach is to use the Balmer jump, by comparing the flux level at ~ 3600 Å to that at ~ 4040 Å. While the models show a visible, but small trend with T_{eff} for the ratios of the fluxes and a clear trend with T_{eff} for the ratios of the spectral slopes, the detector efficiency deforms the spectra in this region, so that this diagnostic cannot be used, either.

The approach, I finally use to determine the appropriate model spectra, employs the available colour information ($B_T - V_T$, $V_T - R$, etc., listed in Table 3.2). For each model I calculate the absolute magnitudes using the filter profiles and flux zero points, i.e. the flux corresponding to a magnitude of zero, given by Maíz Apellániz (2006) for B_T and V_T from Tycho-2, by Cohen et al. (2003) for J , H , and K from 2MASS, and by the Spanish Virtual Observatory Filter Profile Service¹ for R from USNO B1.0. Using the Hipparcos parallaxes (van Leeuwen 2007) to obtain the distances (both given in Table 3.2), I determine the absolute magnitudes of the objects. Comparing these to the model absolute magnitudes does not offer a clear identification of the appropriate model because the uncertainties of the distances are too large. Nevertheless, this comparison reveals that for several objects the apparently closest model effective temperature is considerably lower for the B_T , V_T , and R magnitudes, than for the J , H , and K magnitudes due to interstellar reddening. The determination of the appropriate template has to take this into account.

Colours are independent of the distance. For a comparison of the observed and the model colours, the observed colours are expressed in terms of the model effective temperature T_{eff} and the extinction value A_V . The observed magnitude in one of the filters is the sum of the intrinsic magnitude of the star and the extinction in this filter, e.g. $B_{T,\text{obs}} = B_{T,*} + A_{B_T}$. For colours,

¹<http://svo2.cab.inta-csic.es/theory/fps/>

Table 3.2: The telluric standard stars used for the flux calibration.

Object	Night	SpT	Parallax in mas	Distance in pc	$B_T - V_T$	$V_T - R$	$R - J$	$J - H$	$H - K$	$T_{\text{eff, fit}}$ in K	$T_{\text{eff, mod}}$ in K	A_V
HIP 052453	1	B9.5	3.99 ± 0.5	251 ± 31	-0.001	0.000	0.091	-0.073	0.067	10122	10200	0.1
HIP 066050	1	B8	2.95 ± 0.73	339 ± 84	0.200	0.114	0.527	0.005	0.097	10437	10400	0.9
HIP 078046	1	B6	5.77 ± 0.42	173 ± 13	0.140	0.085	0.364	0.019	0.053	10354	10400	0.6
HIP 078306	2	B9	3.76 ± 0.57	266 ± 40	0.019	-0.003	0.178	0.009	0.007	10949	11000	0.4
HIP 078324	2	B9	5.98 ± 0.93	167 ± 26	0.160	0.095	0.442	0.083	0.087	10631	10600	0.8
HIP 079473	2	B9.5	2.56 ± 1.28	391 ± 195	0.163	0.092	0.333	0.063	0.009	11342	11400	0.8
HIP 079622	2	B8	6.72 ± 0.4	149 ± 9	0.031	0.017	0.180	-0.044	0.082	10310	10400	0.3
HIP 079631	1	B9.5	7.82 ± 0.61	128 ± 10	0.023	0.013	0.154	0.143	0.185	10389	10400	0.3
HIP 079739	1	B8	6.66 ± 0.9	150 ± 20	0.224	0.127	0.580	0.066	0.149	10286	10200	1.0
HIP 080493	1	B9.5	7.43 ± 0.89	135 ± 16	0.229	0.144	0.682	0.123	0.099	10872	10800	1.1
HIP 081208	1	B9	6.61 ± 0.52	151 ± 12	-0.064	-0.033	-0.071	-0.042	0.005	10473	10400	0.0
HIP 086507	1	B9	2.68 ± 0.88	373 ± 123	0.187	0.106	0.490	0.013	0.111	10510	10600	0.8

Note. Spectral types are from the SIMBAD Astronomical Database.

e.g. $B_T - V_T$, this leads to

$$(B_T - V_T)_{\text{obs}} = (B_T - V_T)_* + A_{B_T} - A_{V_T}. \quad (3.1)$$

The intrinsic colours of the star, e.g. $(B_T - V_T)_*$, are expressed as a function of the model effective temperature T_{eff} by fitting a third order polynomial to the colours that results from the calculated magnitudes for each PHOENIX model, i.e. $(B_T - V_T)_* = F(T_{\text{eff}})$. To lower the number of parameters, I express the extinction in a filter X , A_X , in terms of the extinction in the V filter, A_V : $A_X = f_{A_X} \cdot A_V$. I determine the factors f_{A_X} in the following way: I redden the model spectrum with $T_{\text{eff}} = 10\,000\text{ K}$ by $A_V = 1$ in the reddening parametrisation of Cardelli et al. (1989) and O'Donnell (1994). The difference between the magnitude calculated from the reddened spectrum and that from the unreddened spectrum is the factor f_{A_X} . By use of the factors, Equation 3.1 can be rewritten as

$$(B_T - V_T)_{\text{obs}} = F(T_{\text{eff}}) + A_V \cdot (f_{A_{B_T}} - f_{A_{V_T}}). \quad (3.2)$$

Fitting this equation to the observed colours results in a $T_{\text{eff,fit}}$ and an extinction value A_V for each object, listed in Table 3.2. To create the reference spectrum, I use the model spectrum with the closest available $T_{\text{eff,mod}}$ and redden it by the fitted extinction value A_V .

The second step towards a flux calibration is to obtain the absolute level of the spectra. I calculate for each observed magnitude the flux in the corresponding filter and compare the observed fluxes from all filters to the fluxes of the model in the filters. The ratios of the observed flux and the model flux yield factors to bring the model spectrum to an absolute flux scale for each filter. To obtain a reference spectrum on an absolute flux scale, I multiply the whole model spectrum by the mean of the factors.

To obtain a response curve from each object, the observed telluric line corrected spectrum is normalised to 1 s exposure time and the reference spectrum is divided by the normalised observed spectrum. In this response curve the regions around the hydrogen lines and a few other features are excluded because the models and the observations do not match well. The regions affected are listed in Table C.4 in Appendix C. The response is interpolated over these regions. Outliers are filtered using sigma-clipping and the response curve is smoothed to reduce the noise. The response curves obtained for each object are shown in Figures 3.3 and 3.4. The responses of the UVB arm are cut off at $10 \cdot 10^{-15} \text{ erg cm}^{-2} \text{ \AA}^{-1} \text{ ADU}^{-1}$. The maximum values of the response curves vary between $29 \cdot 10^{-15}$ and $97 \cdot 10^{-15} \text{ erg cm}^{-2} \text{ \AA}^{-1} \text{ ADU}^{-1}$. From the individual responses I determine the mean response (thick black dashed line in Figures 3.3 and 3.4) by calculating the mean of all responses in each wavelength bin.

The telluric line removal takes into account the airmass of the individual observation. Nevertheless, the response curves still show a dependency on airmass. On average the response curves from stars observed at lower airmass have a lower flux level. Additionally, the individual response curves show an airmass-dependent tilt. This tilt is more strongly pronounced in the UVB and VIS arms than in the NIR arm, because the atmospheric extinction more strongly affects shorter wavelengths. This is illustrated in Figure 3.5 showing the individual responses normalised at 4050 \AA in the UVB arm, at 7300 \AA in the VIS arm, $11\,100 \text{ \AA}$ in the NIR1 arm, $15\,400 \text{ \AA}$ in the NIR2 arm, and $22\,100 \text{ \AA}$ in the NIR3 arm and colour-coded with airmass. The tilt is taken into account in the following way: Each individual response in each arm is divided by the mean response of that arm. The results of this can be fitted with lines yielding slope and intercept as a function of the airmass, because each observation was taken at a different airmass. Both the intercept and the slope are fitted separately with another line. This results in the slope and intercept a line must have to correct the airmass-dependent tilt of the response for a given airmass.

The response curve used in each arm is the mean response curve determined above from the 14 individual response curves multiplied by the line correcting the airmass-dependent tilt for the airmass at which the science object was observed. The uncertainty of the flux calibration will be examined in Section 5.1.2. A flux-calibrated spectrum is obtained by normalising the telluric

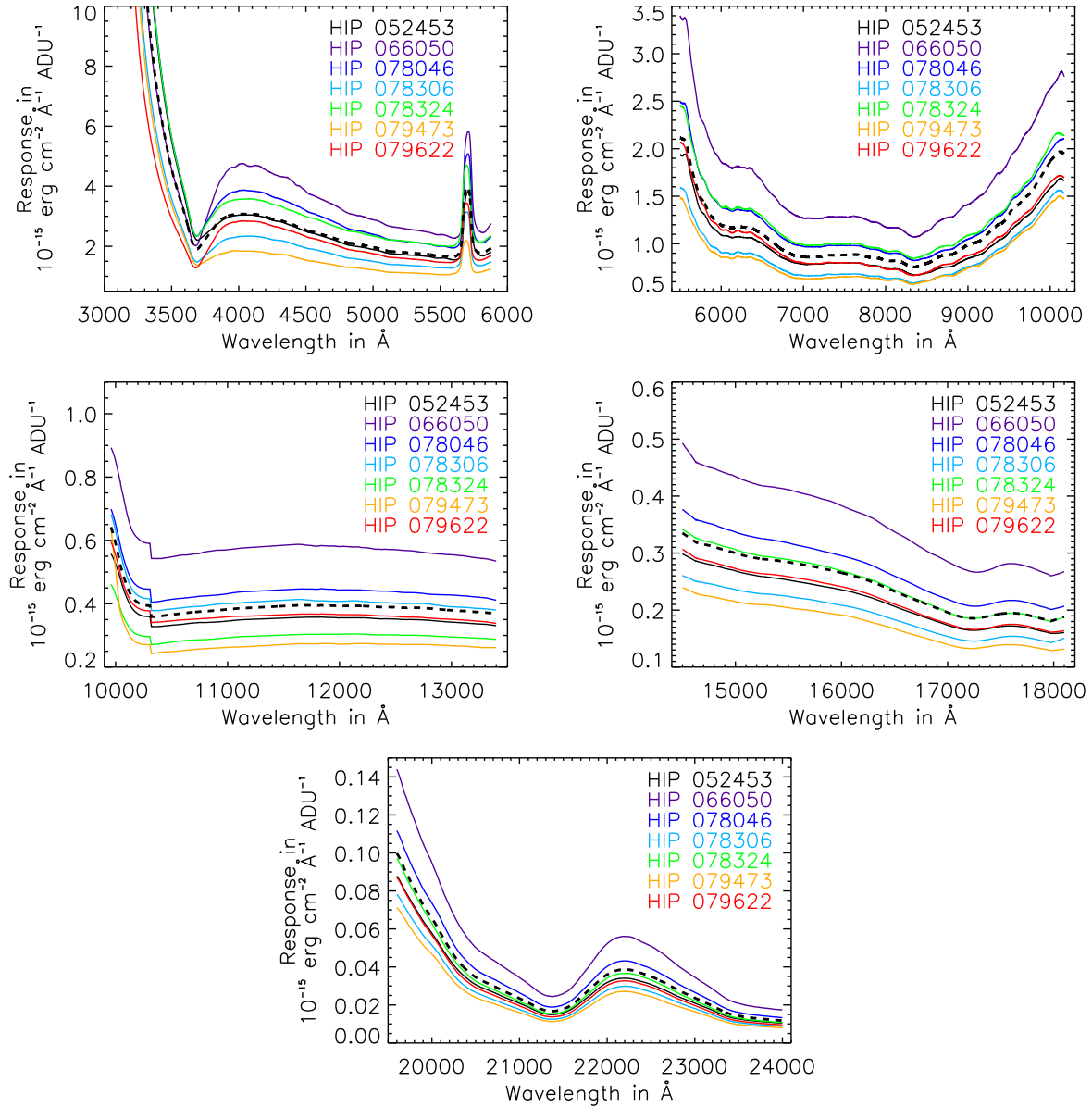


Figure 3.3: The individual response curves determined for each arm for the first 7 objects in Table 3.2: UVB (*top left*, cut off, see text), VIS (*top right*), NIR1 (*middle left*), NIR2 (*middle right*), and NIR3 (*bottom*). The *thick black dashed* line is the mean response.

line corrected spectrum to 1 s exposure time and multiplying by the response curve. Figures 3.6 and 3.7 show the spectra of RU Lup and IM Lup, respectively, flux-calibrated using the response curve determined in this section from the telluric standard stars together with the spectra shown in Figures 3.1 and 3.2 using the flux calibration from the white dwarfs. The latter spectra are multiplied by a factor of 2.5 and 2.7, respectively, to match them at $\sim 15000 \text{ \AA}$ to the former. This comparison illustrates that the spectral shape for both objects is appropriate when using the response curves determined from the telluric standard stars.

3.5 Additional reduction steps

An additional reduction step is the telluric line removal that is part of the data reduction but is discussed in the dedicated Chapter 4. Moreover, two other steps are necessary to complete the data reduction: correcting the mismatch of the flux level at the overlap of the VIS and the NIR arm and determining the radial velocity of the objects at the time of observation.

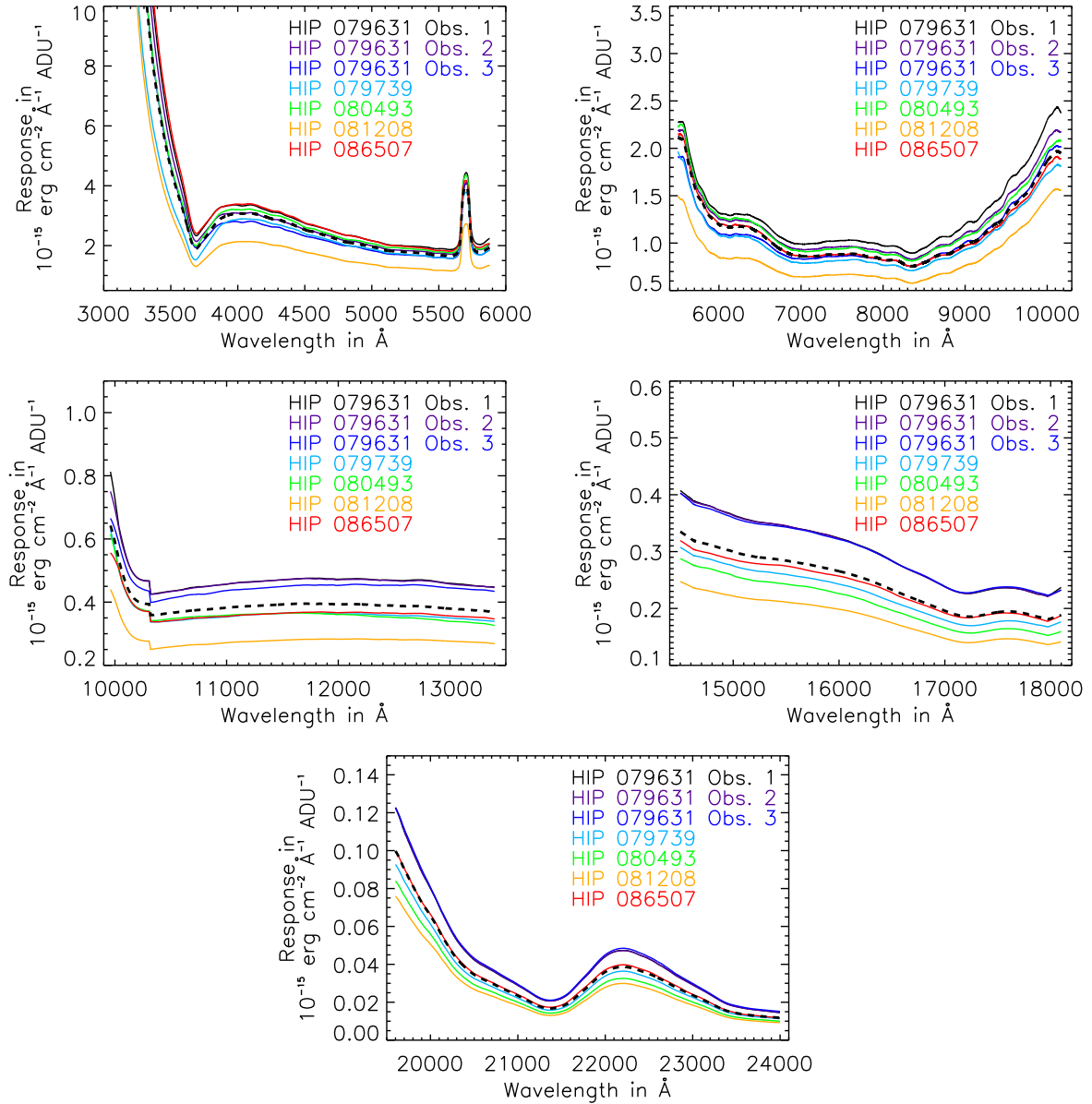


Figure 3.4: As Figure 3.3, but for the remaining 5 objects in Table 3.2. HIP 079631 was observed three times.

In the spectral region, where the coverage of the VIS arm and the NIR arm overlaps, the spectra from the two arms do not have the same flux level. This systematic shift is corrected in the following way: The wavelength range from 10 020 Å to 10 170 Å, which is part of both arms, is divided into 15 portions. In each portion the flux is measured in both arms. The ratio of the fluxes in the VIS arm and the NIR arm yields a factor to shift the NIR spectrum to the level of the VIS spectrum. The spectrum adjusted in this way is used in the further analysis. The overlap of the UVB and VIS arm does not show this problem.

The last step is the determination of the radial velocity of the objects at the time of observation to shift the wavelength array to the rest frame of the star. For this I use the Li I line at 6708 Å, a photospheric line, apart from potential veiling, not influenced by the environment. The observed line is fitted with a Gaussian. The difference between the central wavelength of this Gaussian and the tabulated wavelength yields the radial velocity. The radial velocities for each object are summarised in Table C.5 in Appendix C. Note, that no barycentric correction is applied.

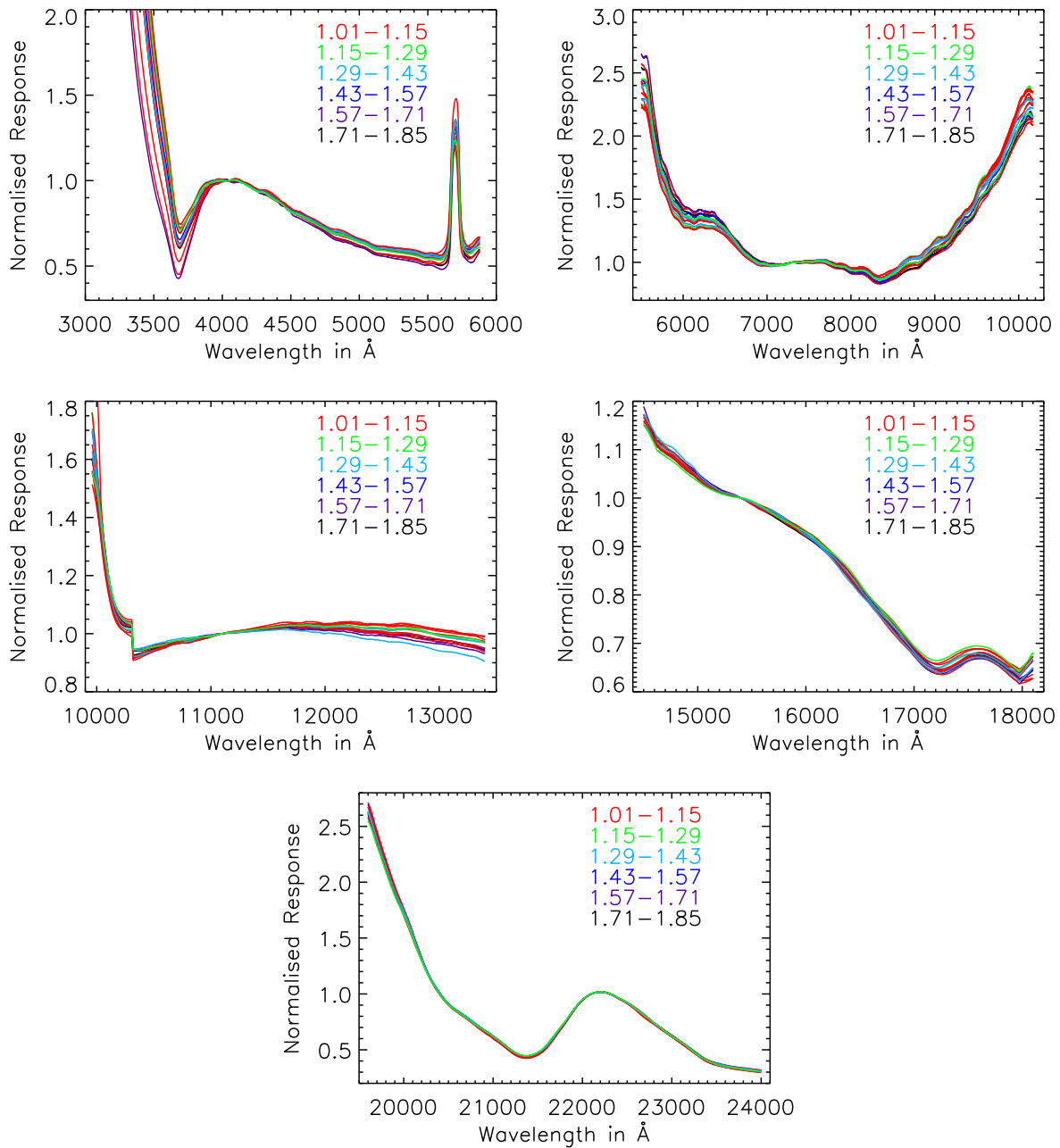


Figure 3.5: The individual response curves normalised (see text) and colour-coded by the airmass of the observation (see legend in the plots): UVB (*top left*, cut off), VIS (*top right*), NIR1 (*middle left*), NIR2 (*middle right*), and NIR3 (*bottom*).

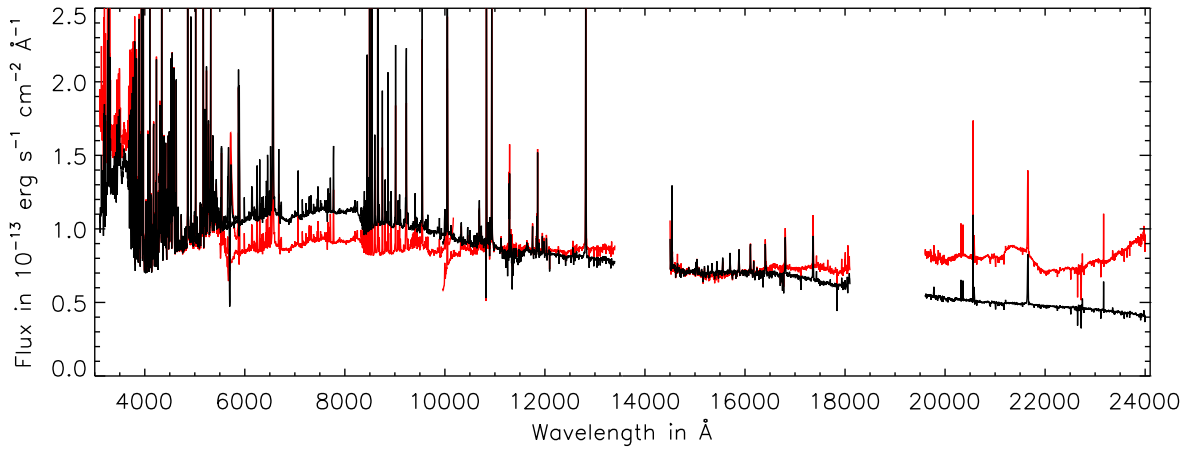


Figure 3.6: The spectrum of RU Lup, flux-calibrated using the response curve from the telluric standards (*black*), together with the spectrum from Figure 3.1, flux-calibrated using the response curve from the white dwarfs (*red*).

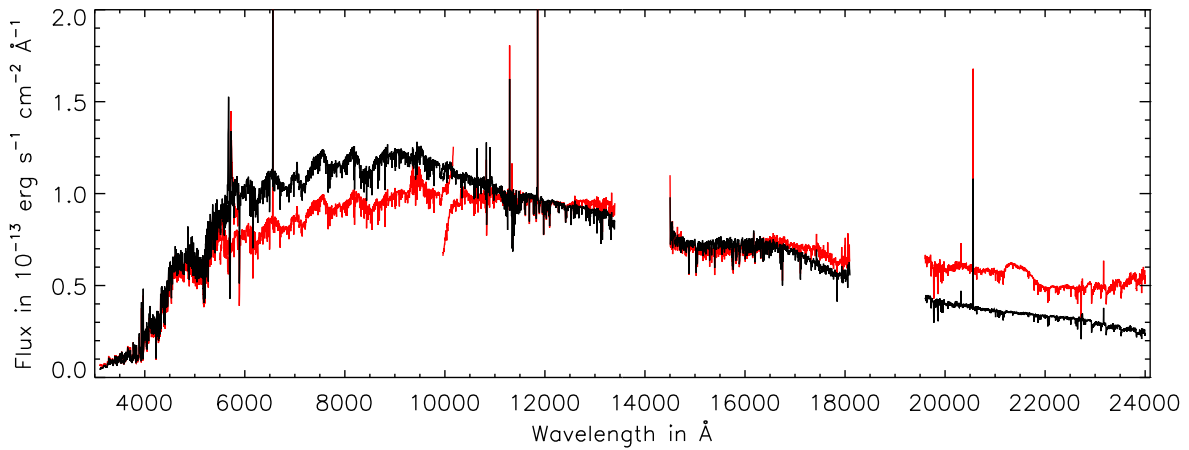


Figure 3.7: The spectrum of IM Lup, flux-calibrated using the response curve from the telluric standards (*black*), together with the spectrum from Figure 3.2, flux-calibrated using the response curve from the white dwarfs (*red*).

Chapter 4

Telluric Line Removal

For ground-based observations in the optical and infrared Earth's atmosphere influences the stellar light. Thus, before the scientific analysis can start, this influence needs to be considered and its imprint on the stellar spectrum must be removed as good as possible. This chapter describes the code package `tellrem` I developed to remove telluric absorption lines from the X-Shooter data. In Section 4.1 I reproduce the corresponding publication (Rudolf et al. 2014), submitted for publication to *Astronomy & Astrophysics*, preceded by a short description of my contribution as the paper lists several authors. The Sections 4.2 to 4.6 present the main content of the user manual accompanying the package describing its use.

4.1 Modelling telluric line spectra in the optical and infrared with an application to VLT/X-Shooter spectra

N. Rudolf, H. M. Günther, P. C. Schneider, and J. H. M. M. Schmitt
submitted to *Astronomy & Astrophysics*

I developed the code that is presented in the paper reproduced in this section. This code implements a method of telluric line removal based on the approach by Seifahrt et al. (2010) expanding it to a much larger wavelength range. As stated in the previous chapter I also carried out the reduction of the used data. H. M. Günther and P. C. Schneider provided ideas for optimising the code and the realisation of the error estimation. Together, we discussed the outcome and conclusions of the work, advised and supported by my supervisor J. H. M. M. Schmitt.

Modelling telluric line spectra in the optical and infrared with an application to VLT/X-Shooter spectra^{★,★★}

N. Rudolf¹, H. M. Günther², P. C. Schneider¹, and J. H. M. M. Schmitt¹

¹ Hamburger Sternwarte, University of Hamburg, Gojenbergsweg 112, 21029 Hamburg, Germany
e-mail: nrudolf@hs.uni-hamburg.de

² Harvard-Smithsonian Center for Astrophysics, 60 Garden Street, Cambridge, MA 02138, USA

Received 25 September 2013 / Accepted XXXX

ABSTRACT

Context. Earth's atmosphere imprints a large number of telluric absorption and emission lines on astronomical spectra especially in the near infrared.

Aims. These are typically removed by comparison to A or B stars used as telluric standard that themselves have strong hydrogen lines which complicates the removal of telluric lines from those regions. We develop a method to circumvent that problem.

Methods. For our IDL software package `tellrem` we use the approach by Seifahrt et al. (2010) to model telluric absorption features with the code LBLRTM (Line-By-Line Radiative Transfer Model). The broad wavelength coverage of VLT/X-Shooter allows us to expand their technique by determining the abundances of the most important telluric molecules H₂O, O₂, CO₂, and CH₄ from sufficiently isolated line groups. For individual observations we build a telluric absorption model for most of the spectral range that is used to remove the telluric absorption from the object spectrum.

Results. We remove telluric absorption from both continuum regions and emission lines without residuals for most of the processable spectral range. The method does not increase the errors noticeably.

Conclusions. Modelling telluric absorption can be an alternative to the observation of standard stars to remove the contamination.

Key words. atmospheric effects – instrumentation: spectrographs – methods: observational – methods: data analysis

1. Introduction

The strong and variable absorption of Earth's atmosphere interferes with almost all ground based astronomical observations. In the optical and infrared spectral range the flux of a celestial body is not only diminished by extinction, also so-called telluric lines are imprinted on the spectra, a fact particularly relevant for high-resolution spectroscopy. The number of telluric lines depends on the wavelength and for the specific case of the VLT/X-Shooter with its wavelength coverage ranging from 3100 Å to 24 700 Å, starting from around 6000 Å bands of water (H₂O) and molecular oxygen (O₂) are predominantly present, accompanied by large contributions of carbon dioxide (CO₂) above 12 000 Å and of methane (CH₄) above 16 000 Å. As is well known, already in the infrared range, the atmospheric transmission becomes quite small in some restricted wavelength bands.

The typical procedure to remove telluric absorption features and recover the original spectrum is to observe a standard star close in time and airmass to the object of interest. Then, the spectrum of the object is divided by the spectrum of the standard star. Early-type stars of spectral type B or A are usually chosen as standard stars because their spectra show only few and rather weak metal lines. Unfortunately, these stars have strong intrinsic photospheric hydrogen absorption features causing severe difficulties if one is interested in the Paschen and Brackett lines of

the science object. The simplest solution for this problem would be to interpolate over the hydrogen absorption and accept the resulting uncertainties. Yet several more sophisticated methods have been developed, e.g., (a) using solar-like stars as telluric standards and a high-resolution solar spectrum (Maiolino et al. 1996); (b) combining the former method, the standard early-type star method and fitting of the hydrogen line profiles (Hanson et al. 1996, 2005); and (c) using A0 stars as telluric standards and a high-resolution model spectrum of Vega (Vacca et al. 2003). Each of these methods has disadvantages and limitations that render the analysis of near-infrared hydrogen lines still difficult.

An alternative approach to the observations of telluric standards is the use of theoretical models of the atmospheric transmission. This idea was successfully pursued before, e.g., by Lallement et al. (1993), Widemann et al. (1994), Bailey et al. (2007), or Seifahrt et al. (2010). The technique to remove telluric absorption presented by Seifahrt et al. (2010) was used, e.g., by Bean et al. (2010) and Rodler et al. (2012). Based on their technique we developed a method to remove telluric lines from VLT/X-Shooter spectra.

Our paper is structured as follows. In Sect. 2 we describe the observations taken with VLT/X-Shooter and their reduction. In Sect. 3 we describe the spectral modelling of the telluric absorption. We restrict ourselves to describing the general functionality of the package and refer to the user manual accompanying the package for details on its use, which we demonstrate in Sect. 4. We present a summary and our conclusions in Sect. 5.

* Based on observations collected at the European Southern Observatory, Paranal, Chile, 085.C-0764(A) and 60.A-9022(C)

** The `tellrem` package is available at the CDS via (link to CDS) and at (link TBD) where also updated versions will be placed.

Table 1. Literature colours and fitted parameters used to create reference spectra for flux calibration.

Object	$B - V$	$V - R$	$R - J$	$J - H$	$H - K$	$T_{\text{eff, fit}} [\text{K}]$	$T_{\text{eff, mod}} [\text{K}]$	A_V
HIP 052453	-0.001	0.000	0.091	-0.073	0.067	10122	10200	0.1
HIP 066050	0.200	0.114	0.527	0.005	0.097	10437	10400	0.9
HIP 078046	0.140	0.085	0.364	0.019	0.053	10354	10400	0.6
HIP 078306	0.019	-0.003	0.178	0.009	0.007	10949	11000	0.4
HIP 078324	0.160	0.095	0.442	0.083	0.087	10631	10600	0.8
HIP 079473	0.163	0.092	0.333	0.063	0.009	11342	11400	0.8
HIP 079622	0.031	0.017	0.180	-0.044	0.082	10310	10400	0.3
HIP 079631	0.023	0.013	0.154	0.143	0.185	10389	10400	0.3
HIP 079739	0.224	0.127	0.580	0.066	0.149	10286	10200	1.0
HIP 080493	0.229	0.144	0.682	0.123	0.099	10872	10800	1.1
HIP 081208	-0.064	-0.033	-0.071	-0.042	0.005	10473	10400	0.0
HIP 086507	0.187	0.106	0.490	0.013	0.111	10510	10600	0.8

2. Observations and data reduction

We observed a sample of 20 T Tauri stars with the VLT/X-Shooter instrument (Vernet et al. 2011). Our observations were carried out in visitor mode during the nights of 2010 May 4 and 5. X-Shooter is a multi-wavelength medium-resolution spectrograph consisting of 3 arms; each arm is an independent cross dispersed echelle spectrograph equipped with optimized optics, dispersive elements and detectors. The UVB arm covers the wavelength range between 3100–5900 Å, the VIS arm that between 5400–10 100 Å, and the NIR arm that between 9900–24 700 Å. The objects were observed in nodding mode with the $0.5'' \times 11''$ slit in the UVB arm and the $0.4'' \times 11''$ slit in the VIS and NIR arms. This instrumental setup results in a resolution of $R \sim 10\,000$ in the UVB arm, $R \sim 18\,000$ in the VIS arm, and $R \sim 10\,000$ in the NIR arm. Additionally, the flux standard star EG 274, a white dwarf, was observed in offset mode with the $5.0'' \times 11''$ slit in all arms.

The data reduction was carried out with the X-Shooter pipeline (Modigliani et al. 2010) version 1.5.0 for the nodding mode for each spectrographic arm individually, following the standard steps which include bias subtraction, sky subtraction via differencing the images from the nodding position A and B, flat-fielding, order-tracing and merging, wavelength calibration, and extraction. However, instead of using the pipeline flux calibration we carry out our own procedures. For the flux standard star EG 274 we first remove the telluric lines from the spectrum using the method described in this paper. Then, we determine the response curve by dividing the corresponding spectrum from the X-Shooter spectrophotometric standard stars catalogue (Hamuy et al. 1994; Vernet et al. 2010) by the observed telluric line corrected spectrum normalised to 1 s exposure time. This ratio is smoothed to reduce the noise and used to flux-calibrate the spectrum.

Unfortunately, we cannot use this flux calibration for the object stars because it does not reproduce the correct spectral shape probably because of the different slit widths. Instead, we use the late B stars that were observed as telluric standard stars in the same setup as the object stars. There are 14 such spectra of 12 stars, with one star observed three times. Because there are no catalogued spectra for the observed stars we use model spectra from the Göttingen Spectral Library by PHOENIX (Husser et al. 2013), observed magnitudes in B and V by Tycho-2 (Høg et al. 2000), R by USNO B1.0 (Monet et al. 2003), and J , H , and K by 2MASS (Skrutskie et al. 2006) as well as reddening according to Cardelli et al. (1989) and O'Donnell (1994) to create a reference spectrum. To find the appropriate model spectrum for each star,

we use the available colour information ($B - V$, $V - R$, etc.). We determine the colours of each model in the filters of the observed magnitudes resulting in a relation between colour and effective temperature T_{eff} of the model. The observed colours are compared to the model colours modified by reddening. This fit yields a $T_{\text{eff, fit}}$ and the extinction value A_V by which the spectrum has to be reddened to create a reference spectrum. We use the model spectrum with the closest available T_{eff} . The determined A_V values for the telluric standards vary between 0 and 1.1. A summary of the used colours, used model T_{eff} , and A_V is presented in Table 1. For each observed spectrum we create a response curve by dividing the reference spectrum by the observed telluric line corrected spectrum normalised to 1 s exposure time. As above this ratio is smoothed to obtain a relative response curve, i.e. the shape of the spectrum. For the absolute flux calibration we compare the model magnitudes to the observed magnitudes. We determine a mean response from the 14 individual responses. Although the reduction takes into account the airmass of the individual observations there still is an airmass-dependent tilt in the individual response curves that is more strongly pronounced in the UVB and VIS arms than in the NIR arm. To correct for this we divide each individual response by the mean response and measure slope and intercept. From these we determine an airmass-dependent relation that is applied to the mean response. To obtain a flux-calibrated spectrum of an object star its telluric line corrected spectrum is normalised to 1 s exposure time and multiplied by the response curve appropriate for the airmass of the observation.

3. Spectral modelling of Earth's atmosphere

In order to compute the theoretical transmission of Earth's atmosphere we apply the technique presented by Seifahrt et al. (2010). Here we provide an overview of this technique and refer to their paper for a more detailed description. Basically the transmission of Earth's atmosphere is computed using the radiative transfer code LBLRTM¹ (Line-By-Line Radiative Transfer Model), which in turn is based on FASCODE (Clough et al. 2005, 1992). The code requires a model of Earth's atmosphere and line data as input.

The required model of the atmosphere provides the vertical temperature, pressure, and molecular abundance profiles. It is built by combining two models: The meteorological models from the Air Resources Laboratory (ARL) at the US National Oceanic and Atmospheric Administration (NOAA) provide tem-

¹ http://rtweb.aer.com/lblrtm_frame.html

N. Rudolf et al.: Modelling telluric line spectra in the optical and infrared with an application to VLT/X-Shooter spectra

Table 2. Spectral ranges used to determine the abundances of H₂O, O₂, CO₂, and CH₄.

Wavelength range [Å]	Abundance fitted
7590–7660	O ₂
9040–9210	H ₂ O
9270–9510	H ₂ O
12 550–12 775	O ₂
13 160–13 280	H ₂ O
14 470–14 685	H ₂ O
14 685–14 900	H ₂ O
19 950–20 300	CO ₂
20 450–20 800	CO ₂
22 850–23 110	CH ₄
23 370–23 630	CH ₄
23 630–23 900	CH ₄

perature, pressure, and dew point temperature for surface heights ≤ 26 km. These so-called sounding files are available at the Global Data Assimilation System (GDAS)² in 3 h intervals. For each object we use the model closest in time to the observation. The information for molecules other than H₂O and surface heights above 26 km is provided by an equatorial MIPAS model atmosphere³, constructed by John Remedios (U. Leicester). The required line data comes from the molecular line database HITRAN in its 2008 edition (Rothman et al. 2009), which provides frequency, line strength, and pressure broadening coefficients for spectral lines of 42 different molecules.

To actually compute a telluric model spectrum for a specific observation taken at an observation altitude h several parameters need to be adjusted. We use the least-squares fitting code MPFIT (Markwardt 2009) to minimise the difference between the observed and the telluric model spectrum. For this purpose the transmission spectrum is adjusted to the slope of the observed spectrum through multiplication by a straight line. In the observed spectrum no distinction is made between regions in the continuum or with absorption or emission lines. During the minimisation the telluric transmission spectrum is (a) shifted in wavelength to match the observed features, the abundances of the main contributing molecules (H₂O, O₂, CO₂, and CH₄) are (b) scaled to the actual observed conditions, and (c) the width of a Gaussian, representing the instrumental profile of X-Shooter, is determined and the high-resolution telluric transmission spectrum is convolved with it. Thus the procedure in principle also yields a radial velocity as well as a set of molecular abundances.

The fit cannot be performed for the whole spectral range at once because, first, LBLRTM can only compute a wave number segment of 2020 cm⁻¹ in one run (~ 1000 Å around 7000 Å, ~ 5300 Å around 16000 Å), second, the continuum approximation by a straight line is only reasonable on local scales, and, third, because of changes in the accuracy of the wavelength calibration along the different X-Shooter orders, which lead to slightly different wavelength shifts of a few tenth of Å and the widths of the Gaussian needed to adjust the telluric transmission spectrum to the observed spectrum, mainly due to the different resolutions in the arms. Within segments of 300 Å length we found the continuum approximation by a straight line to be reasonable and the wavelength calibration to be stable. We thus split the spectrum of an object into such segments and compute for each segment a telluric transmission spectrum.

Instead of refitting the molecular abundances of the main contributors in each segment we make use of the broad wavelength coverage of X-Shooter and the fact that the abundances do not depend on wavelength. We searched for regions in the spectral range of X-Shooter free of stellar features where only one of the main contributors generates lines. We found several spectral regions, where this is the case or the only other contributor is H₂O. For each molecule we determine the abundances in the individual wavelength regions listed in Table 2. The abundances found for each molecule in each region typically differ by less than 10%. We use the mean of these values as the abundance of each molecule during the computation of the telluric transmission spectra for the individual segments thus reducing the number of fitted parameters. The computation time needed on a standard desktop PC to remove the telluric lines from one X-Shooter spectrum is about 45 min.

Finally, the observed spectrum is divided by the computed telluric transmission spectrum to actually remove the telluric features from the observed spectrum.

4. Results

We applied the method described in Sect. 3 to a spectrum of the white dwarf EG 274 and several spectra of classical T Tauri stars (CTTS) obtained with X-Shooter. Telluric absorption lines are only visible in the VIS and NIR arms of X-Shooter. Telluric emission lines are removed by the noded observation mode. The regions between 13 400 Å and 14 500 Å as well as 18 100 Å and 19 600 Å cannot be corrected with this method because they are too heavily contaminated to obtain a reasonable fit of the telluric lines (see Fig. 1). This divides the spectrum of the NIR arm into three parts ranging from 9900–13 400 Å, 14 500–18 100 Å, and 19 600–24 700 Å, respectively.

4.1. Telluric line removal

The performance of the telluric line removal method is illustrated in Fig. 1. Here, the corrected VIS (upper panel) and NIR (lower panel) arm spectrum of EG 274 is shown in black together with the pipeline flux-calibrated spectrum in red and the catalogued flux in blue; the lower parts of the plot show the modelled telluric transmission spectra. An inspection of the modelled transmission spectrum shows that in the wavelength regions between 13 400 Å and 14 500 Å and between 18 100 Å and 19 600 Å the transmitted flux is essentially zero, and therefore the true flux cannot be reconstructed. For most of the spectrum no residuals of telluric lines are visible making the corrected spectrum indistinguishable from the catalogued flux. The emission-like features visible in the observed spectrum longward of 15 000 Å are sky emission that was not entirely removed by the pipeline. Note also the differences between the pipeline flux calibration (red) and our flux calibration (black). These differences are mostly due to the interpolation performed by the pipeline in regions with telluric lines. As we remove the telluric lines before we determine the response, we can use these regions and accurately follow the response over the entire spectral region reaching a better flux calibration than the ESO pipeline.

The method works successfully both in continuum regions and at emission lines. Figure 2 shows some examples. Due to the differences between our flux calibrations and the pipeline flux calibration, the pipeline spectrum had to be shifted (for EG 274), because our flux calibration more accurately follows the catalogue spectrum, or multiplied by a factor (other stars), because

² <http://ready.arl.noaa.gov/READYamet.php>

³ <http://www-atm.physics.ox.ac.uk/RFM/atm/>

A&A proofs: manuscript no. tellrem

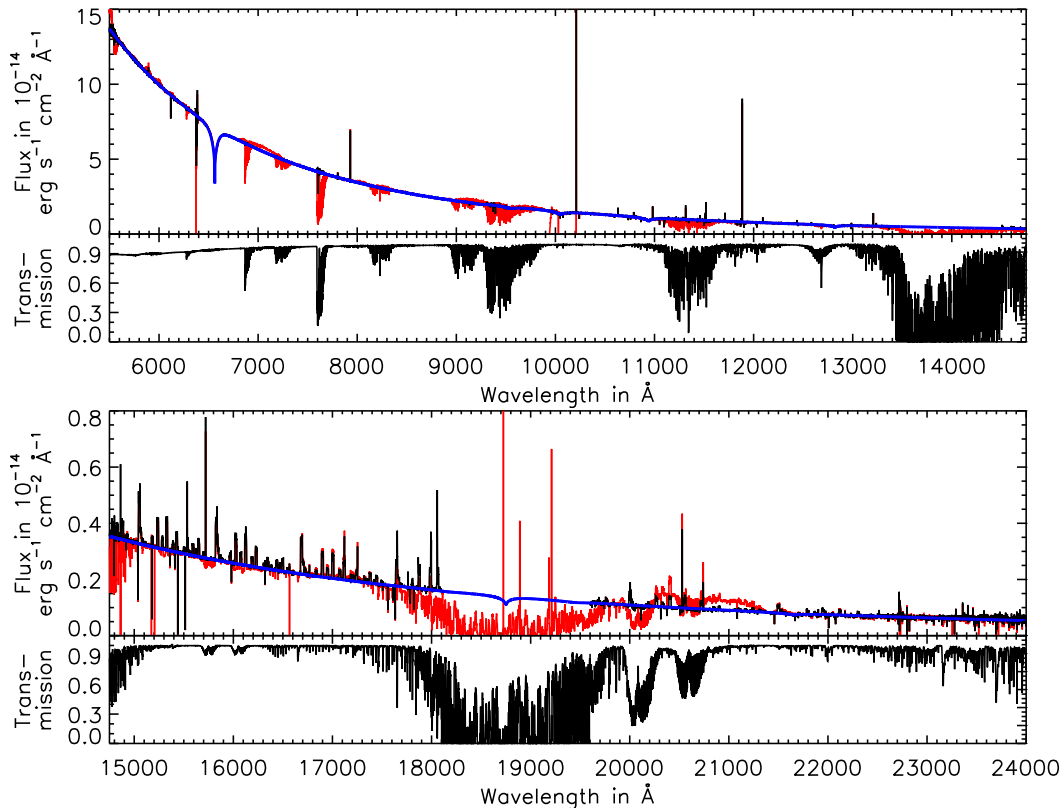


Fig. 1. Telluric line corrected spectrum of the flux standard white dwarf EG 274 (black), pipeline flux-calibrated spectrum (red) for comparison, and catalogued flux (blue) in the upper panel as well as the telluric transmission model in the lower panel of the plots.

the responses are determined for different slit widths, to make the two spectra lie approximately on top of each other in the segment shown. While Figs. 2 (a) to (c) show various hydrogen emission lines of CTTS, Fig. 2 (d) shows a continuum segment of the white dwarf EG 274.

Seifahrt et al. (2010) pointed out that using telluric transmission models to remove telluric lines is mainly limited by the accuracy of the information in the HITRAN database, especially for water lines, which they say are "the hardest to model". Not surprisingly, also our method fails to provide a good fit of the telluric lines in some spectral ranges. These failures are illustrated in the following examples. In Fig. 3 we show the region around 9400 Å, which is dominated by water absorption lines. Both in the continuum segment of the weak-lined T Tauri star (WTTS) MV Lup (Fig. 3 (a)) and the hydrogen emission line Paschen 8 of CTTS V895 Sco (Fig. 3 (b)) there are obvious residuals from poorly modelled water lines. We tried to obtain a better fit of the telluric lines, e.g., by narrowing the fitted region, but did not succeed. We conclude that inaccuracies in the HITRAN database are the likely cause for our failure to reach a better fit.

Apart from the few segments where the telluric line removal cannot be performed or is unsuccessful for the reasons stated above the telluric lines are removed successfully.

4.2. Error estimation

In order to evaluate the performance of our method in a statistical sense we use the spectrum of the white dwarf EG 274. Using the

catalogued flux F_{cat} as the true model and the observed telluric line corrected flux $F_{\text{obs}}^{\text{t.c.}}$ as "data", we studied the distribution of the quantity

$$\chi_{F,i} = \frac{F_{\text{obs},i}^{\text{t.c.}} - F_{\text{cat},i}}{\sigma_{\text{obs},i}^{\text{t.c.}}}, \quad (1)$$

where $\sigma_{\text{obs},i}^{\text{t.c.}}$ denote the statistical errors of the observed telluric line corrected flux. If there was no additional error contribution by the telluric line removal, the distribution should be a Gaussian with the same width in regions without telluric lines and with telluric lines in the original spectrum. In the VIS arm we find a standard deviation of the Gaussian of 1.05 for the regions without telluric lines and 1.19 for the regions which are affected by telluric lines. Thus, the standard deviation increases by 13 %, implying that the errors in the regions containing telluric lines are underestimated by this amount. In the first part of the NIR arm we find standard deviations of 1.16 and 1.81, respectively, resulting in an underestimation of 55 %. We show the corresponding distributions in Fig. 4. The mean relative statistical error is 0.7 % in the VIS arm and 1.1 % in the first part of the NIR arm. Adding the factors derived above increases the errors to 0.8 % and 1.7 %, respectively. For the other parts of the NIR arm this procedure cannot be used because the residuals of the sky lines already cause a deviation from the catalogued flux that would be mixed with the residuals of the telluric line removal.

As an example of practical application, we consider flux ratios. We randomly select from the spectrum two non-overlapping

N. Rudolf et al.: Modelling telluric line spectra in the optical and infrared with an application to VLT/X-Shooter spectra

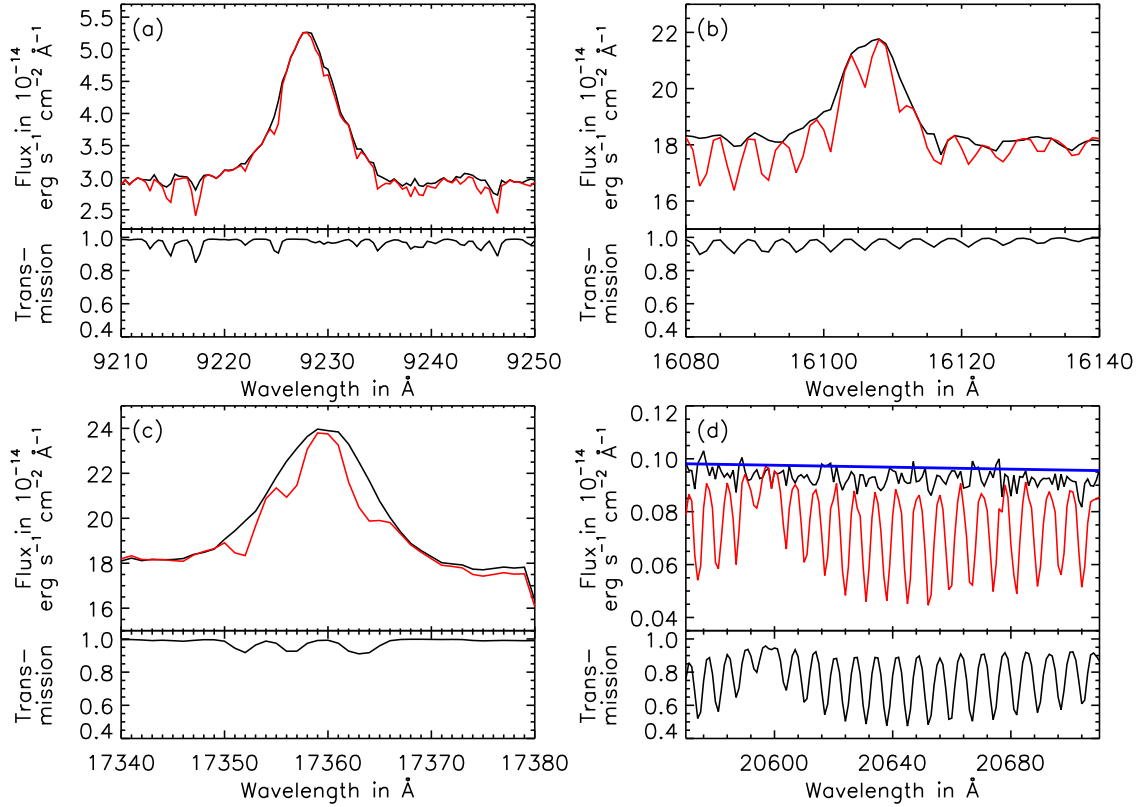


Fig. 2. Examples of telluric line removal leaving no residuals. Corrected spectrum (*black*) and for comparison pipeline flux-calibrated spectrum (*red*) in the upper panels as well as corresponding telluric model in the lower panels of the individual plots: hydrogen lines (a) Paschen 9 of CTTS V895 Sco, (b) Brackett 13 and (c) 10 of CTTS S CrA as well as (d) continuum region of the flux standard white dwarf EG 274 together with catalogued flux (*blue*).

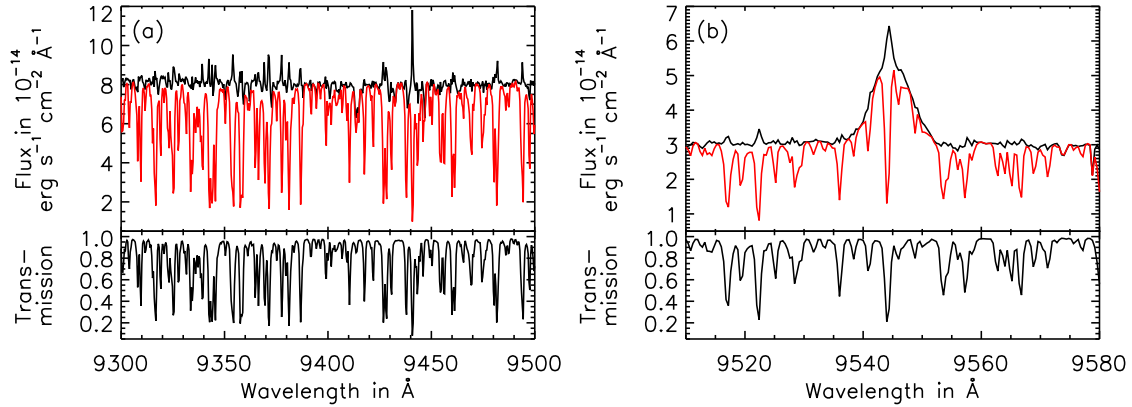


Fig. 3. Examples of telluric line removal leaving residuals. Corrected spectrum (*black*) and for comparison pipeline flux-calibrated spectrum (*red*) in upper panels as well as corresponding telluric model in lower panels of the individual plots: (a) continuum region of WTTS MV Lup, (b) hydrogen line Paschen 8 of CTTS V895 Sco.

regions *a* and *b* of spectral width *w*, integrate the flux in the observed telluric line corrected spectrum and in the model spectrum and calculate the flux ratio of the two regions. We repeat

this for *n* ratios and calculate the quantity

$$\chi_{\text{rat}} = \frac{\left(\frac{a}{b}\right)_{\text{obs}} - \left(\frac{a}{b}\right)_{\text{cat}}}{\sigma_{\left(\frac{a}{b}\right)_{\text{obs}}}}. \quad (2)$$

A&A proofs: manuscript no. tellrem

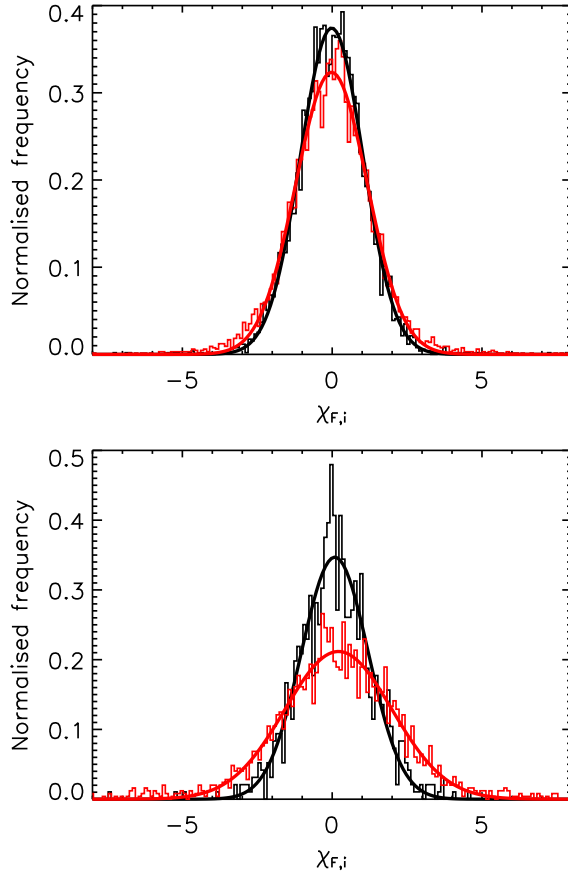


Fig. 4. Distribution of $\chi_{F,i}$ for VIS arm (*top*) and first part of NIR arm (*bottom*), both together with Gaussian fit. *Black*: regions without, *red*: regions with telluric lines in the uncorrected spectrum.

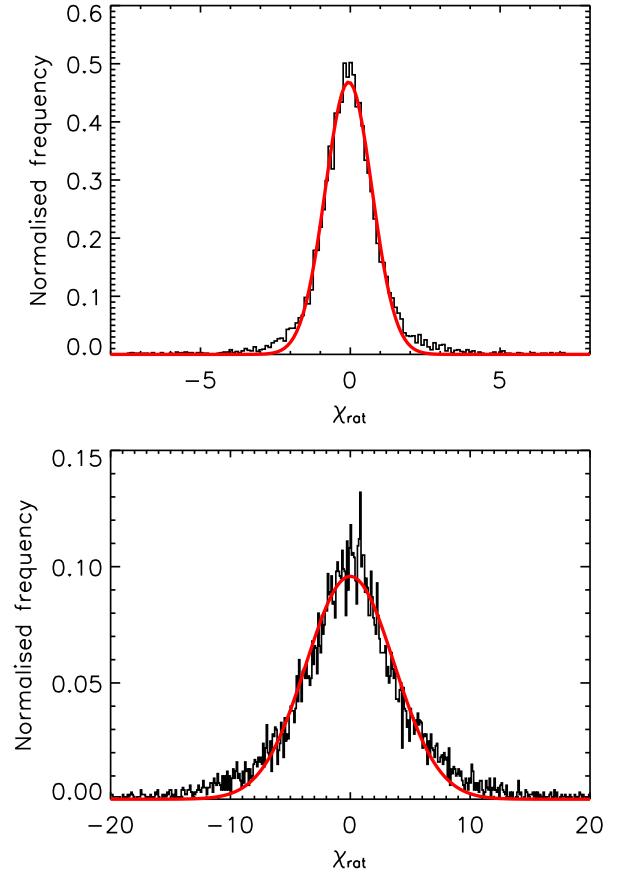


Fig. 5. Distribution of χ_{rat} (*black*) for VIS arm (*top*) and first part of NIR arm (*bottom*), both together with Gaussian fit (*red*).

For $w = 16 \text{ \AA}$, a typical width for hydrogen emission lines in CTTS, and $n = 10000$, the distribution of χ_{rat} is approximately Gaussian. In an optimal case the width of the Gaussian should be 1. Figure 5 shows the distributions. We find a standard deviation of 0.79 in the VIS arm and 3.68 in the first part of the NIR arm, pointing toward an overestimation of the errors for the VIS arm by $\sim 20\%$ from this view. The mean relative statistical error of the n ratios is 0.17%, decreased to 0.14% when subtracting the above factor. In the first part of the NIR arm the standard deviation of the Gaussian is not dominated by the residuals of the telluric line removal any more but by the inferior data quality when compared to the VIS arm due to e.g., detector artefacts.

Combining the results from the two estimators we conclude that the method of telluric line removal presented here does not influence the statistical errors noticeably.

5. Summary and conclusions

We present a method to remove telluric lines from VLT/X-Shooter spectra based on the approach originally put forward by Seifahrt et al. (2010) in the context of CRIRES. In addition to using the line-by-line radiative transfer code LBLRTM and a model of Earth's atmosphere to compute telluric transmission spectra, we utilise the very broad wavelength coverage of X-Shooter to determine the abundances of the most dominant

producers of telluric lines (i.e., H_2O , O_2 , CO_2 , and CH_4) from sufficiently isolated line groups.

The computational effort to implement the telluric line modelling is manageable on a standard desktop PC. Our method removes telluric lines from both continuum regions and emission lines in general without significant residuals. The analysis of two error estimators shows only a marginal additional contribution to the statistical errors due to the telluric line removal for the data used here and the relative statistical error of the telluric line corrected flux is on the order of 2%. There are, however, a few exceptions where probably the accuracy of the line database sets the limits of a successful modelling.

The method works successfully both on high resolution data ($R \sim 70000$) as used by Seifahrt et al. (2010) and the medium resolution data ($R \sim 10000$) provided by the VLT/X-Shooter instrument. In addition to saving precious observing time it also circumvents the difficulties arising from the use of A or B stars as telluric standards for certain scientific applications. These stars are chosen because they have relatively featureless spectra, but they still show hydrogen lines. This complicates the situation once one is precisely interested in these lines in the object stars. Therefore, the use of telluric transmission models to remove telluric lines from observations is a worthwhile alternative to the observation of telluric standard stars.

N. Rudolf et al.: Modelling telluric line spectra in the optical and infrared with an application to VLT/X-Shooter spectra

Acknowledgements. NR acknowledges support by the DLR under project no. 50OR1002, a “DAAD-Doktorandenstipendium” as well as the RTG 1351/2 “Extrasolar planets and their host stars”. This research has made use of NASA’s Astrophysics Data System and of the SIMBAD database, operated at CDS, Strasbourg, France.

References

- Bailey, J., Simpson, A., & Crisp, D. 2007, *PASP*, 119, 228
- Bean, J. L., Seifahrt, A., Hartman, H., et al. 2010, *ApJ*, 713, 410
- Cardelli, J. A., Clayton, G. C., & Mathis, J. S. 1989, *ApJ*, 345, 245
- Clough, S. A., Iacono, M. J., & Moncet, J.-L. 1992, *J. Geophys. Res.*, 97, 15761
- Clough, S. A., Shephard, M. W., Mlawer, E. J., et al. 2005, *J. Quant. Spec. Radiat. Transf.*, 91, 233
- Hamuy, M., Suntzeff, N. B., Heathcote, S. R., et al. 1994, *PASP*, 106, 566
- Hanson, M. M., Conti, P. S., & Rieke, M. J. 1996, *ApJS*, 107, 281
- Hanson, M. M., Kudritzki, R.-P., Kenworthy, M. A., Puls, J., & Tokunaga, A. T. 2005, *ApJS*, 161, 154
- Høg, E., Fabricius, C., Makarov, V. V., et al. 2000, *A&A*, 355, L27
- Husser, T.-O., Wende-von Berg, S., Dreizler, S., et al. 2013, *A&A*, 553, A6
- Lallement, R., Bertin, P., Chassefiere, E., & Scott, N. 1993, *A&A*, 271, 734
- Maiolino, R., Rieke, G. H., & Rieke, M. J. 1996, *AJ*, 111, 537
- Markwardt, C. B. 2009, in *Astronomical Society of the Pacific Conference Series*, Vol. 411, *Astronomical Data Analysis Software and Systems XVIII*, ed. D. A. Bohlender, D. Durand, & P. Dowler, 251
- Modigliani, A., Goldoni, P., Royer, F., et al. 2010, in *Society of Photo-Optical Instrumentation Engineers (SPIE) Conference Series*, Vol. 7737, *Society of Photo-Optical Instrumentation Engineers (SPIE) Conference Series*
- Monet, D. G., Levine, S. E., Canzian, B., et al. 2003, *AJ*, 125, 984
- O’Donnell, J. E. 1994, *ApJ*, 422, 158
- Rodler, F., Deshpande, R., Zapatero Osorio, M. R., et al. 2012, *A&A*, 538, A141
- Rothman, L. S., Gordon, I. E., Barbe, A., et al. 2009, *J. Quant. Spec. Radiat. Transf.*, 110, 533
- Seifahrt, A., Käufel, H. U., Zängl, G., et al. 2010, *A&A*, 524, A11
- Skrutskie, M. F., Cutri, R. M., Stiening, R., et al. 2006, *AJ*, 131, 1163
- Vacca, W. D., Cushing, M. C., & Rayner, J. T. 2003, *PASP*, 115, 389
- Vernet, J., Dekker, H., D’Odorico, S., et al. 2011, *A&A*, 536, A105
- Vernet, J., Kerber, F., Mainieri, V., et al. 2010, *Highlights of Astronomy*, 15, 535
- Widemann, T., Bertaux, J.-L., Querci, M., & Querci, F. 1994, *A&A*, 282, 879

4.2 Preface of the user manual

The `tellrem` package is designed to remove telluric absorption lines from nodded VLT/X-Shooter spectra using atmospheric transmission spectra modelled by the radiative transfer code LBLRTM (Line-By-Line Radiative Transfer Model, Clough et al. 2005). The nodding already removes the telluric emission. Since the models include atmospheric extinction the spectra are also corrected for this effect.

The `tellrem` package is presented in Rudolf et al. (2014). It is based on the approach presented by Seifahrt et al. (2010). If you use this package, please also cite their paper.

While Rudolf et al. (2014) describes the general process, this document describes how to use the package. Section 4.3 explains the installation and the other steps you have to take before you can use the package. Section 4.4 introduces you to the routines in the package and explains how to use them. Section 4.5 gives some introduction to LBLRTM. Although this package was designed for use with X-Shooter spectra, its routines can in principle be used for any spectrum. Section 4.6 gives some advice for this. In Appendix A you can find the documentation of the functions and procedures included in the `tellrem` package.

The design is optimised for running on Linux with IDL in command line mode. The package was tested using Ubuntu 10.04.4, IDL Version 7.1.1., the IDL Astronomy User's Library in the version as of June 2010, MPFIT Version 1.75, and LBLRTM Version 12.0 with LNFL Version 2.6 and AER line parameter database Version 3.0.

4.3 Preparations

Before you can use the package a few preparations are required. These are discussed here.

The first step is to download and prepare software and data that are copyrighted by others, so they are not included in this package:

- LBLRTM (see Sect. 4.3.1)
- line database for LBLRTM (see Sect. 4.3.2)
- MIPAS model atmosphere (see Sect. 4.3.3.2)
- MPFIT and IDL Astronomy User's Library (see Sect. 4.3.4)

The second block of steps is related to your observations, so if you want to use the package on another X-Shooter data set you just have to redo these steps:

- obtain GDAS sounding files (Sect. 4.3.3.1)
- data reduction (Sect. 4.3.5)
- adapt `tellrem` input file (Sect. 4.3.6)

4.3.1 Installation of LBLRTM

LBLRTM can be downloaded for free from the website of Atmospheric & Environmental Research (AER) (http://rtweb.aer.com/lblrmt_frame.html → Code & Examples) for non-commercial use. You need to build the program from the source code before using it. In the LBLRTM package you find three `.tar.gz` archives (`aer_vXXX.tar.gz`, `aerlbl_vXXX.tar.gz`, and `aerlnfl_vXXX.tar.gz`).

`aerlbl_vXXX.tar.gz` contains LBLRTM. Once you unpacked it, you find building instructions in the subfolder `build` where you have to choose the appropriate Makefile for your system. You should choose a double precision one.


```

YR: 2010  MON: 05  DAY: 04  HOUR: 00  AT POSITION: 290.6  66.4  LAT.: -24.63  LON.: -70.40

PRESS HGT(MSL) TEMP DEW PT  WND DIR  WND SPD
HPA      M      C      C      DEG      M/S
E = Estimated Surface Height

 915.   916.   14.2   10.8   191.7    2.7
 900.  1030.   20.3    4.3   129.3    1.3
 850.  1518.   17.8   -0.6    41.5    2.1
 800.  2033.   15.2   -6.2    27.3    4.1
 750.  2576.   12.0  -11.4    16.8    5.7
 700.  3149.    8.6  -16.4    9.5    5.0
 650.  3756.    5.1  -19.4   325.4    3.2
 600.  4405.    1.4  -21.3   251.8    4.7
 550.  5099.   -3.0  -30.0   250.4    7.1
 500.  5845.   -8.4  -32.1   256.1    8.1
 450.  6654.  -13.5  -38.9   247.9    9.9
 400.  7540.  -19.2  -40.2   250.2   14.2
 350.  8517.  -27.2  -44.7   252.2   15.5
 300.  9606.  -36.3  -50.3   245.2   18.7
 250. 10843. -46.0  -61.0   241.9   22.4
 200. 12302. -53.1  -70.5   233.3   28.7
 150. 14121. -62.3  -99.4   237.8   37.7
 100. 16552. -73.1 -273.1   248.4   18.5
  50. 20656. -62.3 -273.1   276.0    4.9
  20. 26520. -48.4 -273.1   126.7    7.0

```

Figure 4.1: Example of GDAS sounding data text file. Its name would be GDAS2010_05_04_00.

- choose the start time of the animation, activate it by choosing “Animation: GIF” and set the duration you need to cover all your observations. The package will search for the sounding file closest to your observation from the files provided
- set “Output Options” to “Text only” and “Graphics” to “Text Listing”
- enter the displayed access code into the text box and click “Get sounding”

From the page, you now see, you have to extract the data for pressure (PRESS), height (HGT(MSL)), temperature (TEMP), dew point temperature (DEW PT), wind direction and speed (WND DIR, WND SPD) and copy it to individual text files for the individual time steps. One file should look like the example in Figure 4.1 (see also file `GDASexample` in the package). Name the individual files `GDASYYYY_MM_DD_HH`, where `YYYY` is the year (e.g. 2010), `MM` the month (e.g. 05 for May), and `DD` the day (e.g. 04 for the fourth). `tellrem` expects the first 6 lines to be comments and the data to begin in line 7. Put all files you created into a folder that contains nothing else.

4.3.3.2 MIPAS model atmosphere

The equatorial MIPAS model atmosphere, constructed by John Remedios (U. Leicester), can be obtained from <http://www-atm.physics.ox.ac.uk/RFM/atm/>. From the “MIPAS Model Atmospheres (2001)” section download `equ.atm`, the equatorial, day-time model.

4.3.4 MPFIT and IDL Astronomy User’s Library

The `tellrem` package makes use of the MPFIT package by Markwardt (2009) as well as several procedures and functions from the IDL Astronomy User’s Library. If you do not already use them download them from <http://purl.com/net/mpfit> and <http://idlastro.gsfc.nasa.gov/>, respectively.

Table 4.1: Content of the `tellrem` input file (see also `info_for_tellrem_example` in the package)

```

/here/lie/the/GDAS/soundingdata/ ; path of folder containing GDAS files
/here/is/the/MIPAS/model/equ.atm ; path to MIPAS model atmosphere
lblrtm_vXX.X_linux_xxx_dbl      ; name of LBLRTM executable
/here/are/the/fits/subfolders/   ; path to folder containing reduced spectra
SCI                               ; type of observation, i.e. SCI, FLUX, TELL

```

4.3.5 Reduction of the spectra

`tellrem` expects the spectra to be reduced but not flux-calibrated. All other steps of the data reduction should be completed, i.e. bias, sky, and dark subtraction, flat-fielding, wavelength calibration, and extraction and merging to 1D spectra. Since the flux calibration also includes an extinction correction using the package on flux-calibrated spectra would take into account the extinction twice.

4.3.6 `tellrem` input file

`tellrem` necessitates several pieces of information for running. These are summarised in a text file that will be read by the procedure `LOADTELLREMINFO`. An example file called `info_for_tellrem_example` is part of the package. You have to adapt it to your setup. The content of this file is shown in Table 4.1. The format needs to be adhered to. The first line contains the folder with the GDAS sounding files you created in Section 4.3.3.1. The second line holds the absolute path to where you saved the MIPAS model atmosphere in Section 4.3.3.2. In the third line you have to enter the name of the LBLRTM executable you built in Section 4.3.1. The fourth line is the path to where your X-Shooter data is stored. The package expects subfolders for each individual observation within this folder. It uses the folder name as object identifier that will be put as auxiliary information into the structure containing the final spectrum (see Section 4.4). Within the subfolder the `.fits` files of the merged 1D spectrum are expected to have the default pipeline file name, i.e. `TYPE_SLIT_MERGE1D_ARM.fits`. While `ARM` will be replaced by the package itself, you have to specify in line 5 of the input file what kind of observation you took. This usually is one of `SCI` for science observations, `FLUX` for flux calibration observations, or `TELL` for telluric standard observations.

4.3.7 Testing the package

Finally, the package provides a test run to check whether the main preparatory steps have been successful. The test is performed by the procedure `TELLREM_TEST_RUN`. It needs 3 inputs: first, the absolute path to where you saved the `tellrem` package, second, the name of the LBLRTM executable, that you built in Section 4.3.1, and, third, the absolute path to where you saved the MIPAS model atmosphere in Section 4.3.3.2. Create a folder and put the customised line database `TAPE3`, that you created in Section 4.3.2, into it. Then you start IDL on the command line in this folder and start the test by typing

```
TELLREM_TEST_RUN, '/the/tellrem/package/is/here/', 'lblrtm_executable',
'/MIPAS/model/is/here/equ.atm'
```

The test will take about an hour on a standard desktop PC. It removes the telluric lines from an observation of MP Mus that is provided with the package and creates the plot file `Tellrem_test_run_comparison.ps` comparing the just determined telluric line removed spectrum to the spectrum provided in the package. Both spectra should be very similar. They probably will not be exactly the same since creating the spectra involves fitting which might lead to slightly different results on different computers and you are probably using an updated version of LBLRTM and the line database, so there might be changes introduced through that. If the

comparison plots look suspicious to you, take a look at the plot file *tellrem_test_run_MPMus.ps* that the procedure also created. Here, you see the fit of the telluric model to the data and the cleaned spectrum. For comparison with the successful run provided in the package, this plot file is also available in the folder *example_files/Test_Run*.

If the test was not successful, you will have to check and redo, if applicable, the preparatory steps to find the specific problem.

4.4 The program package

Once you completed the preparations in Section 4.3, create a folder where you put the customised line database TAPE3, that you created in Section 4.3.2. This is the first input for running LBLRTM. Then you start IDL on the command line in the folder the TAPE3³ is in and run the procedure TELLREM by typing

```
TELLREM, '/path/to/your/info_for_tellrem', telluricremovedspectra
```

and wait for it to finish. Handling one spectrum usually takes between 45 min and 1.5 h. The IDL variable *telluricremovedspectra* will then contain a structure (or an array of structures in case of more than one observation) with the tags explained in Table 4.2. Additionally, two IDL *.sav* files are created (*tellremparams.sav* and *spectra_tellrem.sav*) that contain the parameters and the cleaned spectra, respectively, as well as plots for each object/observation showing the fits of the model to the data and the cleaned spectrum to enable quality control.

TELLREM does the following: First, it calls LOADTELLREMINFO to set the information required for running. These are stored in the common block TELLREM_INFO so that every routine can access them. After calling GETOBJECTS to determine the “objects”, i.e. the folder names, it runs TELLREMPARAMETERS. This function determines the parameters needed to create telluric models matching the observation. After reading the auxiliary information, GETABUNDANCES determines the abundances of the dominant molecules (H₂O, CO₂, CH₄, and O₂) from sufficiently isolated line groups.

The fit is done by FITTELL. It uses MPFIT to fit the model produced by TELL to the data. Free parameters are the abundance relative to the atmospheric model of the molecule to be fitted, the wavelength shift to match the observed features (to allow for uncertainties in the wavelength solution), slope and intercept of the straight line used to adjust the transmission spectrum to the observed spectrum, and the width of the Gaussian, representing the instrumental profile of X-Shooter. TELL calls RUNLBLRTM to calculate the model for a specific set of abundances and then applies the adjustments to the observed data. RUNLBLRTM itself first creates the second input file for LBLRTM, the so-called TAPE5 (see Section 4.5.1 for how this is created), and then runs LBLRTM.

The abundances are then fixed and TELLREMPARAMETERS calls FITTELL repeatedly to fit the remaining parameters (wavelength shift, slope and intercept, width of Gaussian) for the VIS and NIR spectra. The fits are done in 300 Å long segments.

The parameters are then handed over to TELLREMSPECTRA which creates the telluric line removed spectra. For the UVB spectra an extinction curve is determined by UVEXTINCTION. It calculates an appropriate LBLRTM model in this region. As there are no strong lines in this region that would be distinguishable from noise with X-Shooter’s resolution so no fitting is necessary here. The model is smoothed to avoid introducing artefacts by the small lines present in the high-resolution model spectrum. Since there are no lines in the database below 3963 Å, no model can be calculated below 3672 Å. Thus, a fourth order polynomial is fitted to the region between 3700 Å and 4600 Å. This polynomial is then interpolated down to 3100 Å and used as extinction. The wavelength coverage of X-Shooter reaches down to 3000 Å, but the first 100 Å are cut off because they contain in most cases only low and noisy signal. The observed spectrum and the pipeline error are divided by this extinction to create the extinction-corrected spectrum. For the

³LBLRTM searches for its input files in the folder it is called from and quits with an error if it does not find them.

Table 4.2: Structure tags and their content of the output of TELLREM

Tag name	Meaning and content
object	object name (string), i.e. the name of the subfolder the data were read from
obsdate	Julian Date of observation (double scalar), taken from header of VIS data
obsaltitude	altitude the observation was taken at (double scalar), taken from header of VIS data
exptimeu	exposure time in seconds in the UVB arm (double scalar)
exptimev	exposure time in seconds in the VIS arm (double scalar)
exptimen	exposure time in seconds in the NIR arm (double scalar)
wclu	wavelength array in Å for the UVB data (3100 Å–5880 Å)
clu	flux array in ADU of UVB corrected for extinction
eclu	error ^a array in ADU of the UVB flux
wclv	wavelength array in Å for the VIS data (5500 Å–10 170 Å)
clv	flux array in ADU of VIS corrected for extinction and telluric absorption
eclv	error ^a array in ADU of the VIS flux
wcln1	wavelength array in Å for the NIR data in region 1 (9960 Å–13 400 Å)
cln1	flux array in ADU of NIR in region 1 corrected for extinction and telluric absorption
ecln1	error ^a array in ADU of the NIR flux in region 1
wcln2	wavelength array in Å for the NIR data in region 2 (14 500 Å–18 100 Å)
cln2	flux array in ADU of NIR in region 2 corrected for extinction and telluric absorption
ecln2	error ^a array in ADU of the NIR flux in region 2
wcln3	wavelength array in Å for the NIR data in region 3 (19 600 Å–24 000 Å ^b)
cln3	flux array in ADU of NIR in region 3 corrected for extinction and telluric absorption
ecln3	error ^a array in ADU of the NIR flux in region 3

Notes. (a) The errors are propagated pipeline errors, there is no additional contribution to the errors by the telluric line removal considered; (b) Although X-Shooter’s wavelength coverage goes in principle up to 2.5 μm the part above 2.4 μm was omitted due to low data quality in this region in the spectra on whose basis this package was designed.

other spectral parts TELLREMSPECTRA runs RECRFITTELLRES to recreate the model. The observed spectrum and the pipeline error are divided by the model to remove the telluric absorption from the spectra. Finally, the structure or array of structures described in Table 4.2 is returned. For more details on the individual routines take a look at the documentation of the routines in Appendix A and the code itself.

4.5 Basics of using LBLRTM

This Section is intended to give you an introduction into the use of LBLRTM, not to explain how it works in detail. If you are interested in details and the other capabilities and applications of LBLRTM, the paper by Clough et al. (2005) is a good starting point. Some basic introduction to its attributes is also available on the AER website (http://rtweb.aer.com/lblrtn_frame.html → Description). The `FAQ_LBLRTM.pdf` and the `lblrtn_instructions.html` documents available in the `docs` subfolder of the LBLRTM package provide some help and guidance. The HTML is the main source for information on the large number of input parameters available.

4.5.1 The TAPE5

The TAPE5 is the input file for running LBLRTM. It contains all parameters that control its operation. It consists of a number of **records**. It is created by RUNLBLRTM. You find an example TAPE5 in Appendix B where each **record** is indicated so that you can look it up easily in the instructions. Each **record** has a specified format given in the instructions. If you enter a blank or a zero at the position of a parameter, the default value will be chosen by the program, if there is one.

The first group of **records** (**records 1.1 to 1.4**, line 1 to 4 in uncommented TAPE5) set up the general information on which modules to use and for which wave number region to calculate the model. **Records 1.1** has to start with \$ which signals the start of input. Depending on the modules activated in **record 1.2** a certain set of records has to be present (see `lblrtm_instructions.html` for details) in addition to the mandatory ones. Important switches in **record 1.2** that are set to 1 are IHIRAC and ILBLF4 activating the line-by-line calculation using Voigt profiles and ICNTM activating calculation of all continua including Rayleigh extinction where applicable. IEMIT activates the calculation of transmittance and radiance. IATM activates automatic or user-supplied layering of the atmospheric model. The remaining switches are set to zero, except for MPTS and NPTS which are set to 5. **Record 1.3** contains the start and end of the calculation ($V1, V2$). These need to be less than 2020 cm^{-1} apart. **SAMPLE** is the number of sample points per mean halfwidth of a line and is set by default to 4.0. This should be kept to get full accuracy. All other parameters are set to their defaults by either setting to zero, entering the default value, or omitting (i.e. a blank). **Record 1.4** is required in conjunction with IATM=1. The only important parameter is TBOUND which is the temperature in Kelvin at the upper boundary of the atmosphere. It is set to zero here.

The second group of **records** (line 5 to 209, **records 3.1 to 3.6.3**) determines the model atmosphere used. The model atmosphere is composed of N layers at different heights. For each layer temperature, pressure, and the densities of all molecules are provided. One can either use an included atmospheric profile or provide one (switch MODEL in **record 3.1**, line 5). We provide our own, i.e. MODEL=0. The model uses a slant path through the atmosphere (switch ITYPE=3), starting at the observatory altitude (H1 in **record 3.2**, line 6) and ending in space (defined to start at 75 km, HSPACE), and taking into account the zenith angle of the observation (ANGLE in **record 3.2**) to determine the atmospheric layers crossed by the stellar light. NMOL is set to 19 as the highest-ranking molecule we use is number 19 (OCS). We actually only use 13 molecules (H_2O , CO_2 , O_3 , N_2O , CO , CH_4 , O_2 , NO , SO_2 , NO_2 , NH_3 , HNO_3 , OCS). The available ones and their positioning is detailed in Table I of `lblrtm_instructions.html`. The remaining switches of **records 3.1** and **3.2** and all switches of **record 3.3A** (line 7) are set to default. **Record 3.4** (line 8) defines the number of layers in the model (IMMAX=50). **Record 3.5** (line 9) defines the altitude (ZM), pressure (PM), and temperature (TM) at the first boundary as well as information on the units the data is provided in (JCHARP, JCHART, JLONG, JCHAR(M), see Table I of `lblrtm_instructions.html`). **Records 3.6.1 to 3.6.3** (line 10 to 12) provide the density data for each molecule (VMOL(M)). Since the 13 molecules used here are not the first 13, we have to "use" 19 molecules (switch NMOL=19 in **record 3.1**) and set the non-used ones to zero. The information in **record 3.5 to 3.6.3** is then repeated for the remaining 49 layers. The -1. in line 209 signals the end of the repetition. The data put in these **records** is combined from the GDAS sounding data and the MIPAS model in the following way: First, the height, temperature, pressure, and dew point temperature from the GDAS sounding data are used. The dew point temperature serves as density information for water. The densities of the other molecules are interpolated from the MIPAS model to the heights of the GDAS data. After the end of the GDAS data (usually somewhere between 26 km and 27 km) the data from the MIPAS model is used in its 1 km spacing up to 48 km, followed by using it in 5 km spacing up to 88 km. The density profiles of the individual molecules can be changed by multiplying with a factor. RUNLBLRTM has keywords for this purpose for H_2O , CO_2 , CH_4 , O_2 , O_3 , NO , and NH_3 .

In principle the TAPE5 could end here. LBLRTM outputs TAPE12 containing the monochromatic results for the transmittance (and the radiance). Since this file is unformatted, another step is necessary to transform it into an ASCII file. The next group of `records` is doing that. Here, LBLRTM is restarted (`records 1.1` and `1.2` with only `IPL0T=1` to activate “plotting”, i.e. extracting, line 210 and 211). `Record 12.2A` (line 213) tells LBLRTM to extract the wave number range determined by `V1` and `V2` from the TAPEXX specified by `LFILE` (TAPE12 in our case) in standard output (`IOPT=0`). The remaining parameters are arbitrary. They were used when LBLRTM still had actual plotting capabilities. `JEMIT=0` and `JOUT=3` in `record 12.3` (line 214) state to extract the transmittance and write it to the TAPEXX specified by `JPLTFL`, set to `99` here. Again, the remaining parameters are arbitrary. TAPE99 is read by `RUNLBLRTM`. The `-1.` in line 215 signals the end of the “plotting”. The `%` in line 216 signals the end of the TAPE5.

4.5.2 Other points to know

LBLRTM calculates the radiative transfer line-by-line, meaning that the spectral resolution is only limited by the actual width of the Voigt profiles used in the calculations. The parameter `SAMPLE` in `record 1.3` sets the number of sample points per mean halfwidth of a line. This parameter is set to 4, the maximum it can take. For NIR the models have resolutions above 500 000. The models are calculated with an almost equidistant spacing in wave number of $\sim 0.0027 \text{ cm}^{-1}$. Thus, after converting to wavelength you do not have equidistant bins. As mentioned above, LBLRTM can be used for many more applications and thus has a lot of modules not used here. For example, it can take into account effects like aerosol contribution, clouds, and rain.

4.6 Using tellrem for other spectra

Although this package is designed for use on X-Shooter spectra, it can in principle be used for any spectrum. This Section intends to assist you to adapt it for your situation.

4.6.1 Input

The model atmosphere is optimised for the VLT site, so you might want to consider using a different model than the MIPAS equatorial model if your data was not taken there. The observatory elevation is an important input to the model. Its by default set to that of the VLT at Paranal. Use the keyword `OBSELEVATION` in `RUNLBLRTM` to set another one.

You should create a new TAPE3 only encompassing the wavelength region you are interested in (see Section 4.3.2).

4.6.2 Adapting the routines

You cannot use TELLREM to run all the steps at once, but you have to create your own versions of TELLREMPARAMETERS and TELLREMSPECTRA adapted to your data. You might need your own routine to read the data from the `.fits` files. Reading the data is done by `RDDAT`. It should work with ESO data, but better check.

Most importantly, the abundance determination for H_2O , CO_2 , CH_4 , and O_2 done by `GET-ABUNDANCES` will not work if your spectra do not cover the wavelength ranges it requires. Within the X-Shooter spectral range and for X-Shooter resolution the contribution by other molecules is only marginal. For other spectra you may want to check the contributions of other molecules. Currently, `RUNLBLRTM` only has keywords for adjusting the abundance of H_2O , CO_2 , CH_4 , O_2 , O_3 , NO , and NH_3 . If you want to check other molecules, just add keywords to the code to access the other available molecules. The model does not use all molecules available in the MIPAS model, so if you think one of them might be important for you, adjust the code to take it into account too.

To check which molecules contribute in your wavelength range, use `RUNLBLRTM` to calculate transmission spectra. Calculate one that contains all molecules, one that contains only water (by setting the others to a very small value, e.g. 10^{-20} , **but not to zero**), and one that contains water and the molecule in question. Setting the water abundance to a very small value crashes `LBLRTM`. Overplot them to see the contributions. Once you identified the important molecules either adapt `GETABUNDANCES` and the `parinfo` structure handed over to `FITTELL` to your situation by using different molecules and/or regions or skip the predetermination of the abundances and set them as free parameters in the fit by adjusting the `parinfo` structure accordingly. If you can avoid setting the abundances as free parameters you should do so because the fitting tends to get unstable with many free parameters. In the `parinfo` structure, also check the start values and limits. Additionally, take a look at `TELL`. You might have to adjust the factors in the parameter assignment to match your spectra so that the numerical values of the parameters `MPFIT` hands over to it have the same order of magnitude. This is recommended by C. Markwardt for stability. Then, you need to run `FITTELL` with your data and the adjusted `parinfo` structure. Another issue to look at is the length of the segments in which the model is fitted. The choice of 300 Å for X-Shooter was mainly based on the instrument stability, so for another instrument you might be able to use longer ones, but keep in mind that the adjustment of the model to the data is done by multiplication with a straight line. This approximation is only valid on local scales. Finally, either save the cleaned spectrum directly from the output of `FITTELL` or adjust `TELLREM-SPECTRA` to feed your data to `RECRFITTELLRES`.

Chapter 5

Relevant Theories and Methods

For the interpretation of the CTTS spectra I employ the fluxes of hydrogen emission lines. The measurement of these fluxes and the estimation of their uncertainties are described in Section 5.1. To examine the temperature T and electron density n_e in the emitting gas in the vicinity of CTTSs, I use models for the level populations in recombining hydrogen that are detailed in Section 5.2, while their usage will be explained in Section 5.4.1. The reddening that the light experiences on its way from the star to the observer and how common upper level hydrogen lines can be used to express it, is depicted in Section 5.3. How this can be used to examine the extinction value A_V and the exponent α of the reddening power law follows in Section 5.4.2.

5.1 Hydrogen emission line fluxes

For the analyses described in this chapter the fluxes of the hydrogen emission lines in the spectra of the sample objects need to be measured. The Paschen and Brackett lines present in each object are summarised in Table C.1 and C.2 in Appendix C.1. Section 5.1.1 describes the method used to measure the line flux, while Section 5.1.2 details the estimation of the uncertainties of the measured line fluxes.

5.1.1 Measuring the line fluxes

Regarding the measurement of the fluxes of the hydrogen emission lines in the spectra the following items need to be taken into account. The emission lines are formed on top of a photospheric absorption line, i.e. the absorption line first needs to be filled up before the line goes into emission. The observed sample contains three stars that do not show emission in the Paschen and Brackett lines: IM Lup (M0), Sz77 (M0), and MV Lup (K2). These stars can be used as templates to factor in the photospheric absorption. This is illustrated in Figure 5.1 (upper panel) using the example of RU Lup and the template IM Lup. Using the radial velocities determined from the spectrum (see Section 3.5) the x-axis is given in velocities with reference to the rest velocity of the line. In the region of the Br11 and Br12 lines there is recognisable photospheric structure in the spectrum of IM Lup, most pronounced in the Br12 between -500 km s^{-1} and 0 km s^{-1} . The emitted line flux is thus the difference between the photospheric spectrum given by the template spectrum and the observed signal.

Prior to the measurement of the line fluxes the best matching template out of the three non-emitting stars in the sample is determined for each object. This is done by determining fluxes at 25 wavelength positions in the spectrum using each template. These fluxes measure the deviation between the object spectrum and the templates. They will be called deviation fluxes in the following for clarity. The positions, listed in Table C.3 in Appendix C, were chosen so that they do not fall in the vicinity of emission lines in the object spectra, but otherwise randomly. Measuring deviation fluxes and actual line fluxes is done the same way: The template spectrum is first multiplied by a factor to match the flux level of the object spectrum. This factor

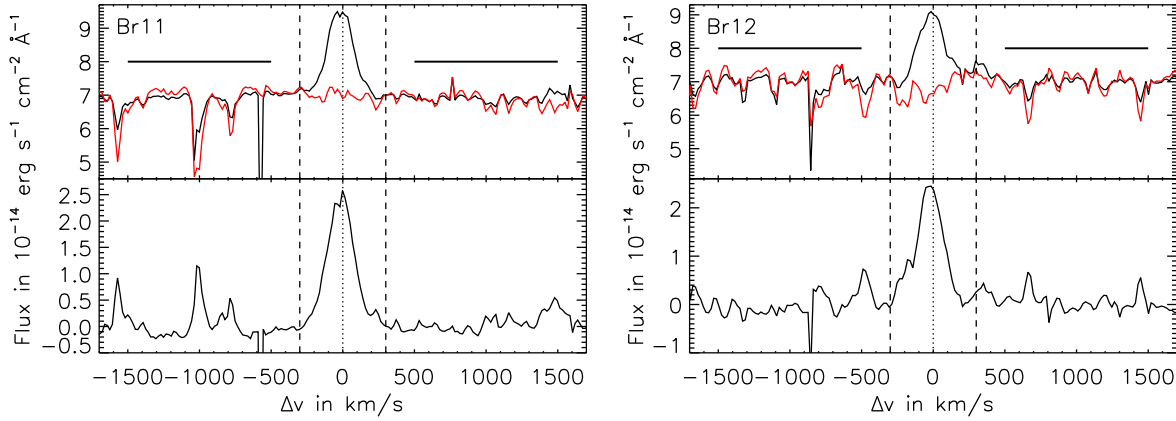


Figure 5.1: The Br11 (*left*) and Br12 (*right*) lines of RU Lup (*black*) together with the template IM Lup (*red*) in the *upper* panel and the residual spectrum in the *lower* panel. The *horizontal* lines denote the continuum areas, the *dashed* lines border the area in which the flux is determined.

Table 5.1: The template spectra used for the object spectra in the line flux determination.

Object name	Template name	Object name	Template name
S CrA	Sz77	V2062 Oph	IM Lup
TW Hya	IM Lup	V2129 Oph	IM Lup
EX Lup	IM Lup	V2251 Oph	IM Lup
GQ Lup	IM Lup	V2252 Oph	IM Lup
HO Lup	IM Lup	VV Sco	Sz77
RU Lup	IM Lup	V895 Sco	Sz77
MP Mus	MV Lup	V1279 Sco	IM Lup
V853 Oph	IM Lup	V4046 Sgr	Sz77
V2058 Oph	IM Lup		

is determined by dividing the mean of the object spectrum in a velocity range next to the individual line or position in question (denoted by the horizontal lines in Figure 5.1) by the mean of the template spectrum in the same area. This velocity range serves as estimate of the continuum around the position or line although this region is not necessarily free of absorption lines. The adjusted template spectrum is subtracted from the object spectrum and the flux is measured by adding up this residual spectrum (lower panel in Figure 5.1) in a velocity range around the line or position (denoted by the dashed lines in Figure 5.1).

The velocity ranges used in the determination of the best template are the following: for the continuum $\mp 500 \text{ km s}^{-1}$ to $\mp 1500 \text{ km s}^{-1}$ is used, while the flux summation is done in the range -400 km s^{-1} to $+400 \text{ km s}^{-1}$. For each template the 25 deviation fluxes are squared and summed. The template amounting to the smallest sum has on average the smallest deviation from the object spectrum. This template is used in the determination of the emission line fluxes. The templates used for each object are summarised in Table 5.1.

For the line flux determination the velocity ranges $\mp 500 \text{ km s}^{-1}$ to $\mp 1500 \text{ km s}^{-1}$ are used for the continuum, while values between $\mp 300 \text{ km s}^{-1}$ and $\mp 500 \text{ km s}^{-1}$ border the flux summation range, depending on the behaviour of the surrounding spectrum (see Table 5.2). This simple approach to measure the line fluxes cannot be used for blended lines (e.g. Pa13, Pa15) or lines that are not sufficiently isolated (e.g. Pa17 and higher, Br18 and higher).

Another complication arises from the environment the lines are produced in. The line profile is complicated. Several lines show absorption in the red side of the lines. Figure 5.2 shows this for the Br11 and Br12 lines of RU Lup. It is clearly visible that using the flux of the whole line underestimates the total emitted flux, since this absorption is most likely produced

Table 5.2: The velocity ranges used as continuum and line in the line flux measurements of Paschen and Brackett lines.

Line	Wavelength in Å	Continuum start in km s ⁻¹	Continuum end in km s ⁻¹	Flux summation start/end in km s ⁻¹
3-14	8598.4	500	1500	300
3-12	8750.5	500	1500	400
3-11	8862.9	500	1500	400
3-10	9014.9	500	1500	400
3-9	9229.0	500	1500	400
3-8	9546.0	500	1500	400
3-7	10049.4	500	1500	400
3-6	10938.2	500	1500	500
3-5	12818.1	500	1500	500
4-17	15438.9	500	1500	300
4-16	15556.5	500	1500	300
4-15	15700.7	500	1500	300
4-14	15880.6	500	1500	300
4-13	16109.3	500	1500	300
4-12	16407.2	500	1500	300
4-11	16806.5	500	1500	300
4-10	17362.1	500	1500	300
4-7	21655.3	500	1500	300

by kinematic components (e.g. other accretion funnels, see Section 2.1) and not in the regions where the emission is originating from. To avoid this, only the flux in the blue side of the line is used in the further analysis. In principle one would have to use twice the blue side flux as the total line flux, but since the analyses are based on ratios of line fluxes, there is no need to do this.

5.1.2 Estimating the uncertainties of the line fluxes

The total uncertainty of the line flux measurements (see Section 5.1.2.5) consists of several components: the statistical uncertainty (Section 5.1.2.1), the uncertainty due to the subtraction of a template (Section 5.1.2.2), and the uncertainties of the relative and the absolute flux calibration (Sections 5.1.2.3 and 5.1.2.4). The quantity of these individual uncertainties needs to be examined before further analyses using the fluxes and flux ratios can be conducted.

5.1.2.1 Statistical uncertainty

The ESO pipeline provides the uncertainty associated to each detector pixel. This uncertainty is propagated at all stages of the pipeline using the standard error propagation formulae and results in a statistical uncertainty of the flux in each spectral bin of the reduced spectrum. I propagate these uncertainties through the flux calibration. The uncertainty of a flux measurement consists of the uncertainties of the template $\sigma_{\text{templ},i}$ and the observed spectrum $\sigma_{\text{obs},i}$. The line flux F is measured from the residual spectrum, thus the uncertainty of the flux σ_F is

$$\sigma_F = \Delta\lambda \cdot \sqrt{\sum (\sigma_{\text{obs},i}^2 + \sigma_{\text{templ},i}^2)}, \quad (5.1)$$

with $\Delta\lambda$ the constant bin size of the data. Figure 5.3 (*left*) shows the relative statistical uncertainty $\frac{\sigma_F}{F}$ as a function of flux for all measured Paschen and Brackett lines of all objects. The relative uncertainty is in most cases below 1% (see Figure 5.3, *right*).

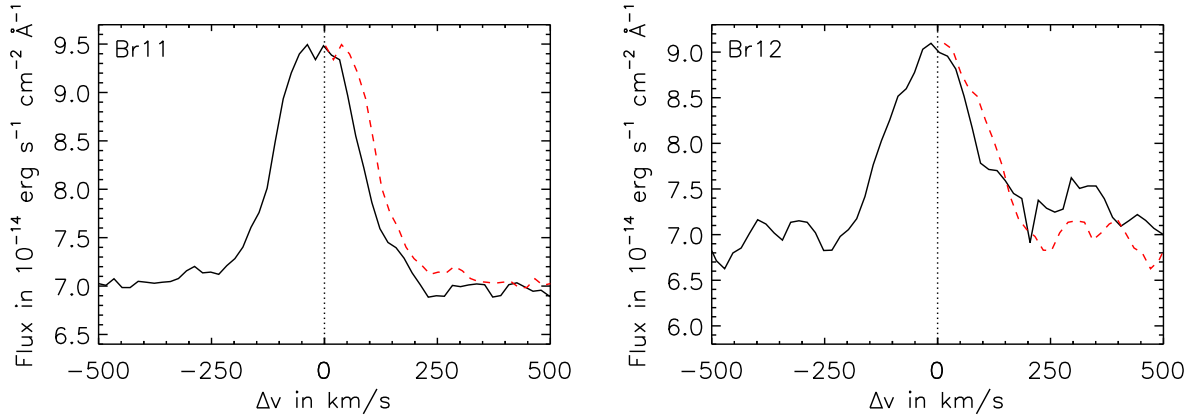


Figure 5.2: The Br11 (*left*) and Br12 (*right*) lines of RU Lup (*black*). The blue side of the line is mirrored to the red side (*red dashed*) to reveal the line asymmetry.

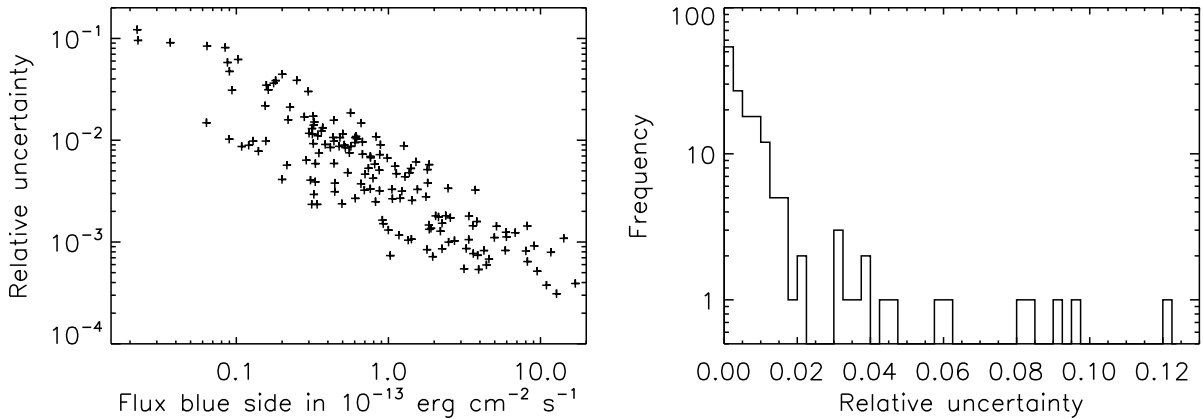


Figure 5.3: The relative statistical uncertainty as a function of flux for all measured line fluxes (*left*) and a histogram of the relative uncertainties (*right*).

5.1.2.2 Uncertainty due to the template subtraction

The template subtraction introduces an additional uncertainty, because the selected template is not a perfect match to the object spectrum. I employ the deviation fluxes used to determine the best template (see Section 5.1.1) to examine this uncertainty. These fluxes characterise the deviation of the template and the object spectrum, i.e. the amount of flux erroneously added or removed by subtracting the template. If the spectra were identical, the fluxes would be zero. To estimate the magnitude of the relative uncertainty introduced by this procedure, I compare each deviation flux with the surrounding continuum. For the continuum I use the mean level of the object spectrum in the region that was used to match the template spectrum to the object spectrum. This level is integrated to a flux in the same width as the deviation flux. Using the same regions, which have been used to determine the best template, to estimate the uncertainty created by the template subtraction is of course statistically not correct. In principle, I should use another set of emission line free regions for this. However, there is only a limited number of such regions in the spectrum. The more of these I can use for the determination of the best template the more reliable this determination is.

Figure 5.4 (*left*) shows the relative uncertainty as a function of the continuum flux for all measured deviation fluxes. For most cases the relative uncertainty lies below 1% (see Figure 5.4, *right*). For the further analysis I use 1% of the flux value to represent the uncertainty due to the template subtraction, i.e. $\sigma_{F, \text{templ sub}} = 0.01 F$.

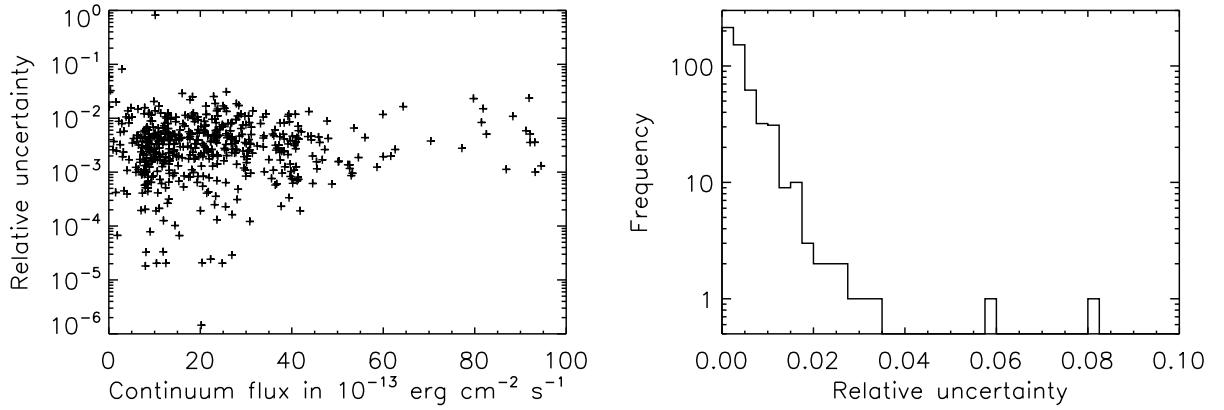


Figure 5.4: The relative uncertainty due to the template subtraction as a function of the continuum flux for all deviation fluxes (*left*) and a histogram of the relative uncertainties (*right*).

Table 5.3: The regions excluded in the determination of the mean of the individual responses.

Arm	Excluded region(s)
UVB	$\lambda < 4000 \text{ \AA}$
UVB	$5600 \text{ \AA} < \lambda < 5800 \text{ \AA}$
NIR1	$\lambda < 10150 \text{ \AA}$
NIR2	$\lambda > 17900 \text{ \AA}$

5.1.2.3 Uncertainty of the relative flux calibration

The uncertainty of the relative flux calibration, i.e. the general shape of the response curve, is important not only for the flux measurement itself, but also for the accuracy of ratios of lines. As described in Section 3.4.2, I use the mean response curve multiplied by a first order polynomial dependent on the airmass AM of the individual observation in the flux calibration. To examine the uncertainty of the relative flux calibration I have to examine the individual responses that build the mean response. First, I bring all the individual responses to $AM = 1$ by dividing them by the correction line to remove this effect from the uncertainty estimation. Second, to remove the influence of the absolute flux calibration I normalise each response in each arm by dividing by the mean of the arm excluding regions which show obvious systematic effects like the bump around 5700 \AA . These regions are summarised in Table 5.3. The spectral coverage of the arms can be found in Section 3.1. From these normalised responses I determine the mean \bar{r}_{norm} and the standard deviation $\sigma_{r_{\text{norm}}}$ at each wavelength point. The relative uncertainty of the relative flux calibration is given by $\frac{\sigma_{r_{\text{norm}}}}{\bar{r}_{\text{norm}}}$. Figure 5.5 (*left*) shows the relative uncertainties for the VIS arm. The plots for the other arms can be found in Figure D.1 in Appendix D.1. Within an arm the typical uncertainty of the relative flux calibration is 2% (see Figure 5.5, *right*, and Figure D.1). The peak around 0.18 in the distribution of the relative uncertainty comes from the UVB response. Here, the region between 3000 \AA and 4000 \AA shows a large spread between the individual responses because the efficiency of the detector is dropping of very steeply to bluer wavelengths. For the further analysis I use 3% of the flux value to represent the uncertainty of the relative flux calibration, i.e. $\sigma_{F, \text{rel fluxcalib}} = 0.03 F$.

Because I am interested in line ratios from different arms, I also need an estimate of the quality of the relative flux calibration between arms. For this inter-arm deviation I look at the means used to normalise the responses above. For ratios of these means from different arms the influence of the absolute flux calibration is removed. The ratio of means from two arms R_{arms} is calculated for each individual response. The mean \bar{R}_{arms} and standard deviation $\sigma_{R_{\text{arms}}}$ of the ratios allow an estimation of the relative uncertainty of the inter-arm flux calibration by using $\frac{\sigma_{R_{\text{arms}}}}{\bar{R}_{\text{arms}}}$. The analyses presented in this chapter require ratios R of lines from the VIS arm and NIR1, NIR2,

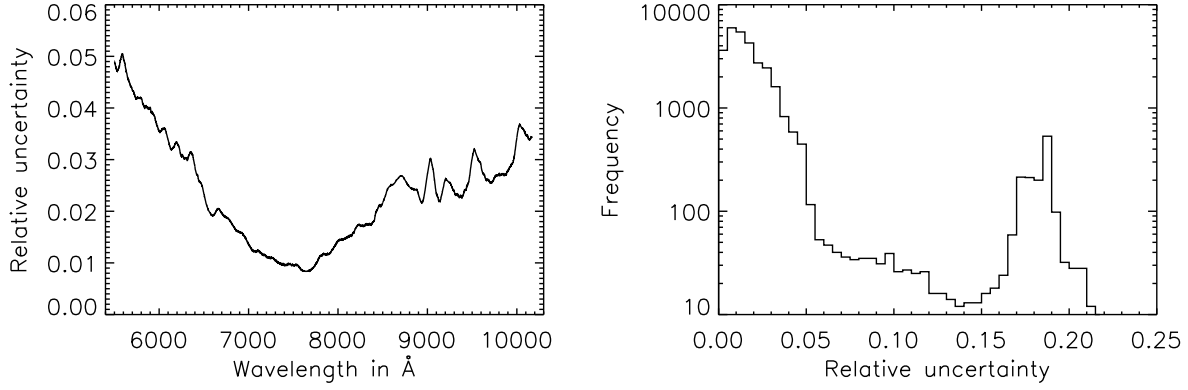


Figure 5.5: The relative uncertainty of the relative flux calibration for the VIS arm (*left*) and a histogram of all relative uncertainties in all arms (*right*).

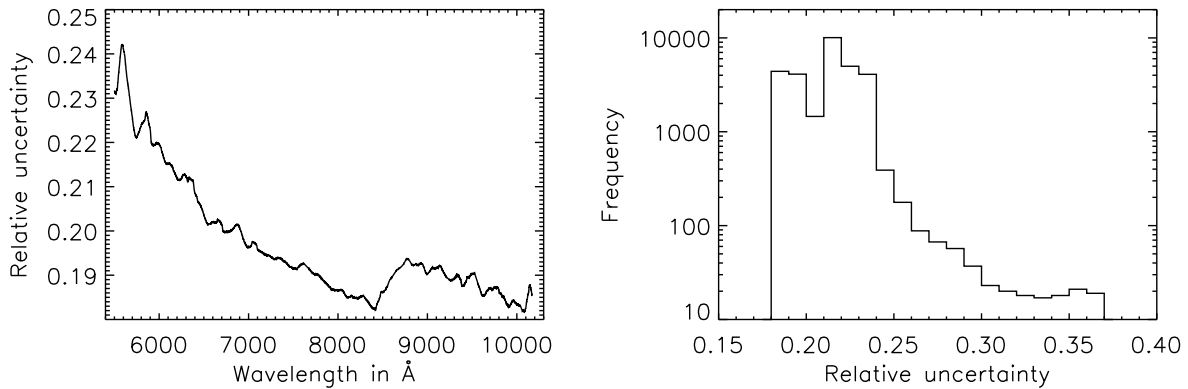


Figure 5.6: The relative uncertainty of the absolute flux calibration for the VIS arm (*left*) and a histogram of all relative uncertainties in all arms (*right*).

and NIR3 arms as well as from the NIR3 arm and the NIR1 arm (which technically are the same arm, but treated individually). The relative uncertainty for these combinations of arms varies between 5% and 11%. For the further analysis I use 10% of the ratio value to represent the uncertainty of the relative inter-arm flux calibration, i.e. $\sigma_{R, \text{rel fluxcalib}} = 0.1 R$.

5.1.2.4 Uncertainty of the absolute flux calibration

The accuracy of the line flux measurements depends also on the accuracy of the absolute flux calibration. For the analysis of line ratios the uncertainty of the absolute flux calibration is not relevant. Nevertheless, I estimate the uncertainty of the absolute flux calibration by determining the mean \bar{r} and the standard deviation σ_r of the responses obtained from the 14 telluric standard observations at each wavelength point. Figure 5.6 (*left*) shows the relative uncertainty $\frac{\sigma_r}{\bar{r}}$ for the VIS arm. The plots for the other arms can be found in Figure D.2 in Appendix D.2. As can be seen from the histogram of all relative uncertainties (see Figure 5.6, *right*), the relative uncertainty lies in most cases between 20% and 25%.

5.1.2.5 Total uncertainty

The uncertainty of a flux ratio consists of two parts. The first part is the uncertainty σ_F of a flux measurement F :

$$\sigma_F^2 = \sigma_{F, \text{stat}}^2 + \sigma_{F, \text{templ sub}}^2 + \sigma_{F, \text{rel fluxcalib}}^2, \quad (5.2)$$

where the uncertainty of the absolute flux calibration has been neglected as it is not relevant for flux ratios. The second part is the uncertainty of the relative flux calibration between two

arms, $\sigma_{R, \text{rel fluxcalib}}$. Thus, the total uncertainty of a ratio $R = \frac{F_1}{F_2}$ is given by

$$\sigma_R^2 = \frac{\sigma_{F_1}^2}{F_2^2} + \left(\frac{\sigma_{F_2} \cdot F_1}{F_2^2} \right)^2 + \sigma_{R, \text{rel fluxcalib}}^2, \quad (5.3)$$

using error propagation for the uncertainties of the fluxes.

5.2 Models for the level populations N_{nl} in recombining hydrogen

The population N_{nl} of a level with the principal quantum number n and the azimuthal quantum number l is described by the Boltzmann equation for thermodynamic equilibrium. The fraction of atoms excited to the level nl is given by

$$N_{nl} \propto g_{nl} e^{-\frac{E_{nl}}{k_B T}}, \quad (5.4)$$

where g_{nl} is the statistical weight that accounts for the degeneracy of the levels, i.e. the number of levels with the same energy, E_{nl} the excitation energy of the level nl , k_B the Boltzmann constant, and T the temperature. For hydrogen E_{nl} is independent of l , but l will be important for non-thermodynamic equilibrium processes that will be described below. The ratio of populations in two levels nl and $n'l'$ is then

$$\frac{N_{nl}}{N_{n'l'}} = \frac{g_{nl}}{g_{n'l'}} e^{-\frac{\Delta E}{k_B T}}, \quad (5.5)$$

with $\Delta E = E_{nl} - E_{n'l'}$. If one of the levels is the ionisation state with population N_+ , we need to know the statistical weight $g = g_+ g_e$ composed of the statistical weight g_+ of the ionised atom and the statistical weight g_e of its free electron. The electron has two possibilities to orientate its spin. In addition we have to consider the factor $\frac{(2\pi m_e k_B T)^{3/2}}{h^3 N_e}$, where m_e is the mass of the electron, h Planck's constant, and N_e the number of electrons, for its movement in momentum and position space. Thus, the statistical weight of an ion plus its free electron is given by

$$g = g_+ \cdot 2 \cdot \frac{(2\pi m_e k_B T)^{3/2}}{h^3 n_e}. \quad (5.6)$$

Using this in Equation 5.5 results in the Saha-Boltzmann equation

$$\frac{N_+}{N_{nl}} = \frac{2g_+}{g_{nl}} \frac{(2\pi m_e k_B T)^{3/2}}{h^3 N_e} e^{-\frac{\chi_{nl}}{k_B T}}, \quad (5.7)$$

where $\chi_{nl} = \Delta E = E_+ - E_{nl}$ is the ionisation energy of the level nl .

One possibility to describe the population N_{nl} in recombining hydrogen under conditions not in thermodynamic equilibrium is the approach by Baker & Menzel (1938). They divide their models into two distinct approximations, case A and case B. In case A all transitions are considered to be optically thin. In case B the gas is optically thick for the Lyman series photons and optically thin for all other photons. In general, a gas being optically thick means that photons emitted within it get absorbed or scattered before they can leave the gas. In the description of the cases this means that the rate equations of the level populations N_{nl} contain all transitions in case A. In case B transitions to the ground level ($n = 1$, Lyman series) are omitted, because these photons are re-absorbed almost immediately after being emitted (“on-the-spot-approximation”). Subsequently, they are converted to photons of other series once the de-excitation occurs on another path than immediately to the ground level.

The case A and B models were extended by Storey & Hummer (1995), based on Hummer & Storey (1987), Storey & Hummer (1988), and Hummer & Storey (1992). These authors additionally incorporate radiative processes like recombination and bound-bound transitions as well as collisional effects like ionisation, three-body recombination, and transitions between

individual n and l states for hydrogen-like atoms with $Z \leq 8$. Their calculations for the level populations N_{nl} therefore depend on the temperature T and the electron density n_e of the gas. In the Baker & Menzel (1938) approximation the level populations N_{nl} are expressed using the Saha-Boltzmann equation (Eq. 5.7) and the so-called departure coefficients b_{nl} describing the departure from thermodynamic equilibrium, i.e. $b_{nl} \equiv 1$ in thermodynamic equilibrium:

$$\frac{N_{nl}}{N_e N_+} = b_{nl} \frac{g_{nl}}{2g_+} \left(\frac{h^2}{2\pi m_e k_B T} \right)^{\frac{3}{2}} e^{\frac{\chi_{nl}}{k_B T}}. \quad (5.8)$$

The main computational effort of Storey & Hummer (1995) is in the determination of the b_{nl} incorporating the processes described above that are responsible for the deviation from thermodynamic equilibrium. The differentiation between case A and B is accomplished by adapting the rate equations as described above. The methods of calculation are described in detail in the mentioned publications and the references therein, describing them here goes beyond the scope of this chapter.

Storey & Hummer (1995) provide files containing the line emissivities for all transitions with $n \leq 25$ and total recombination coefficients. A Fortran programme extracts from these the ratio of the intensities of two specified transitions for all available temperatures ($T_{\min} = 500$ K, $T_{\max} = 30\,000$ K in 9 steps) and electron densities ($n_{e, \min} = 10^2$ cm $^{-3}$, $n_{e, \max} = 10^{14}$ cm $^{-3}$ in 12 steps). The data files and the Fortran programme are available as Vizier Online Data Catalogue VI/64¹.

5.3 Reddening of ratios of common upper level hydrogen lines

The flux F_{ub} emitted by a transition from an upper level with principal quantum number u to a lower (or bottom) level with principal quantum number b in an optically thin gas is in general described by

$$F_{ub} = N_u \cdot (A_{ub} + B_{ub} I_\nu) \cdot E_{ub}. \quad (5.9)$$

where N_u is the population of the upper level with principal quantum number u . The Einstein coefficients A_{ub} for spontaneous emission and B_{ub} for stimulated emission state the transition probabilities. I_ν is the intensity of the radiation field, while $E_{ub} = \frac{hc}{\lambda_{ub}}$ is the energy of the transition with Planck's constant h , the speed of light c , and the wavelength λ_{ub} of the transition. Compared to the level populations given by Equation 5.8 no distinction for different azimuthal quantum numbers l of the level is made since the energy levels only depend on the principal quantum number n . Stimulated emission becomes an important processes only if the gas is in a non-equilibrium state resulting in a population inversion, conditions not likely to appear in the gas in the vicinity of CTTS. Thus, this term can be omitted. The population density depends on the temperature and density of the gas (see Section 5.2). A ratio of lines that have a common upper level is given by

$$\frac{F_{ub_1}}{F_{ub_2}} = \frac{N_u \cdot A_{ub_1} \cdot \lambda_{ub_2}}{N_u \cdot A_{ub_2} \cdot \lambda_{ub_1}} = \frac{A_{ub_1} \cdot \lambda_{ub_2}}{A_{ub_2} \cdot \lambda_{ub_1}}. \quad (5.10)$$

This ratio is given by parameters known from atomic physics and independent of the way the upper level is populated and depopulated and thereby independent of the temperature and density of the gas. Any deviation of the measured line ratios from these has to be caused by reddening.

The degree of reddening (or selective extinction) is quantified by the colour excess

$$E_{B-V} = (B - V) - (B - V)_0, \quad (5.11)$$

where $(B - V)$ is the observed value of the colour index and $(B - V)_0$ is the intrinsic value of the colour index the object would have without reddening. The total extinction A_λ at a

¹<http://vizier.u-strasbg.fr/viz-bin/VizieR?-source=VI/64>

given wavelength for a corresponding colour excess depends on the wavelength dependence of the extinction, the extinction curve (see also Section 2.3). In the visual passband the extinction A_V , which is an individual characteristic of each object describing the extinction in the V band, can be given as

$$A_V = R_V \cdot E_{B-V}, \quad (5.12)$$

where R_V is the ratio of total to selective extinction which takes a value of $R_V \sim 3.1$ for diffuse dust. The relative extinction at a given wavelength can be expressed as

$$\frac{E_{\lambda-V}}{E_{B-V}} = \frac{A_\lambda - A_V}{E_{B-V}} = \frac{A_\lambda}{E_{B-V}} - R_V. \quad (5.13)$$

The reddening in the near-infrared wavelength region is typically described by a power law of the form $A(\lambda) \sim \lambda^{-\alpha}$, with the exponent α . Using various photometric data sets from U to M of diffuse and cloud extinction, Martin & Whittet (1990) find that for the wavelength region from I to M ($0.9 \mu\text{m}$ to $5 \mu\text{m}$) a universal extinction curve exists represented well by an exponent of $\alpha \approx 1.8$. Cardelli et al. (1989) find that an exponent of $\alpha = 1.61$ represents a mean extinction law in the wavelength region $0.9 \mu\text{m}$ to $3.3 \mu\text{m}$ using photometry from U to L ($0.36 \mu\text{m}$ to $3.5 \mu\text{m}$) of a sample of stars to determine the extinctions. Fitzpatrick (1999) uses synthetic photometry of a model stellar atmosphere to examine the wavelength dependence of the optical and infrared extinction curve. For wavelengths greater than $1 \mu\text{m}$ he finds an exponent of $\alpha \sim 1.5$. Comparing UKIDSS and 2MASS photometric data of several galactic regions to galactic population synthesis models reddened with different power laws Stead & Hoare (2009) find an exponent of $\alpha = 2.14$. Fitzpatrick & Massa (2009) introduce a different form of the near-infrared extinction curve that “mimics a power law whose exponent increases with wavelength” after analysing photometry and spectrophotometry from UV to NIR. This form is very similar to the simple power law with $\alpha = 1.84$ for $R_V \sim 3$. González-Fernández et al. (2014) conclude from their analysis of photometry of red clump giants that neither the simple power law with a single exponent nor the more complex form by Fitzpatrick & Massa (2009) seem to reproduce the overall shape of the extinction between $1 \mu\text{m}$ and $8 \mu\text{m}$.

For the further analysis, I will use the power law Martin & Whittet (1990) find from a fit to their diffuse extinction data from R to M ($0.5 \mu\text{m}$ to $5 \mu\text{m}$). The power law takes the form

$$\frac{E_{\lambda-V}}{E_{B-V}} = 1.19\lambda^{-1.84} - 3.05, \quad (5.14)$$

as given in Whittet (1992). Comparing Equations 5.13 and 5.14 yields $\frac{A_\lambda}{E_{B-V}} = 1.19\lambda^{-1.84}$ and $R_V = 3.05$. Using Equation 5.12 results in an expression for the total extinction A_λ (in mag) depending on the visual extinction A_V and the wavelength λ , given in μm :

$$A_\lambda = 0.39A_V\lambda^{-1.84}. \quad (5.15)$$

The emitted line flux F_{unred} is lowered by reddening A_λ to the observed line flux F_{obs} . Using the definition for magnitude differences, this can be expressed by:

$$A_\lambda = -2.5 \log \frac{F_{\text{obs}}}{F_{\text{unred}}} \rightarrow F_{\text{unred}} = F_{\text{obs}} \cdot 10^{\frac{A_\lambda}{2.5}}. \quad (5.16)$$

Thus, using the power law given in Equation 5.15 the extinction factor E_{cor} needed to correct observed fluxes F_{obs} to obtain the emitted fluxes F_{unred} is given by

$$E_{\text{cor}} = 10^{\frac{0.39}{2.5} A_V \lambda^{-\alpha}}, \quad (5.17)$$

with the extinction value A_V and $\alpha = 1.84$.

For the hydrogen atom, the wavelength λ of a transition can be expressed as

$$\frac{1}{\lambda} = R_\infty \left(\frac{1}{b^2} - \frac{1}{u^2} \right), \quad (5.18)$$

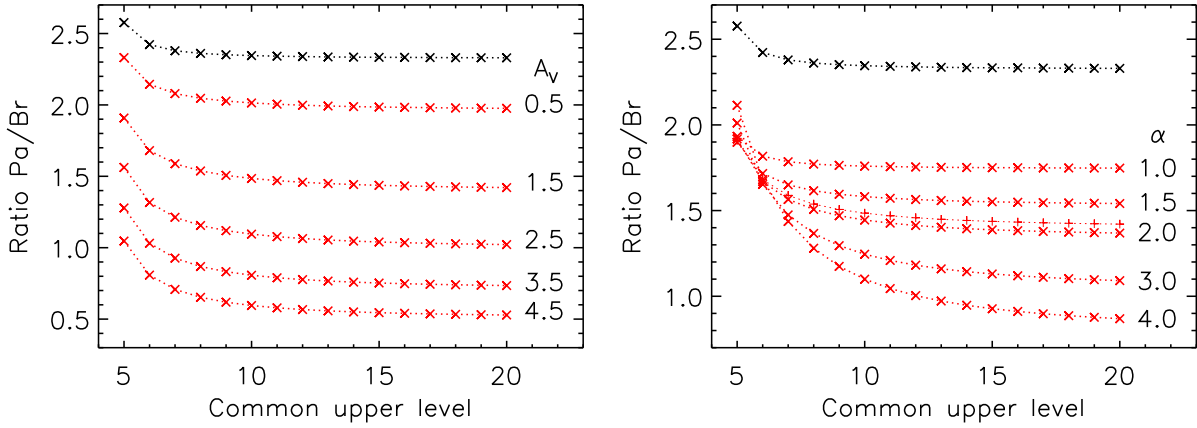


Figure 5.7: The ratios of Paschen and Brackett lines with a common upper level given by Equation 5.10 (*black*), for integer numbers only, reddened according to Equation 5.19 (*red*) with $\alpha = 1.84$ and varying A_V (*left*) and with $A_V = 1.5$ and varying α (*right*), the ratios denoted by *plus signs*, +, are reddened with $\alpha = 1.84$

where R_∞ is the Rydberg constant, b the lower and u the upper level of the transition. For ratios of Paschen ($b = 3$) and Brackett ($b = 4$) lines with a common upper level u this results in

$$\frac{F_{\text{cor, Pa}}}{F_{\text{cor, Br}}} = \frac{F_{\text{obs, Pa}}}{F_{\text{obs, Br}}} \cdot \frac{E_{\text{cor, Pa}}}{E_{\text{cor, Br}}} = \frac{F_{\text{obs, Pa}}}{F_{\text{obs, Br}}} \cdot 10^{\frac{0.39}{2.5} A_V R_\infty^\alpha \left(\left[\frac{1}{3^2} - \frac{1}{u^2} \right]^\alpha - \left[\frac{1}{4^2} - \frac{1}{u^2} \right]^\alpha \right)}. \quad (5.19)$$

Figure 5.7 illustrates the effect of reddening on the ratios of Paschen and Brackett lines with a common upper level. The ratios given by Equation 5.10 were reddened using the extinction factor given in Equation 5.19 varying either A_V or α . The left hand plot in Figure 5.7 shows the effect of different extinction values A_V for the exponent $\alpha = 1.84$. The higher A_V , the more flux is lost and the tilt of the graph grows slightly. The right hand plot in Figure 5.7 shows the effect of different exponents α of the extinction power law for an extinction value of $A_V = 1.5$. A variation in α changes the tilt of the graph affecting the amount of flux that is lost.

For a study of the reddening law using observed line ratios we can reorganise Equation 5.19, replacing the corrected fluxes F_{cor} with the theoretical fluxes F_{theo} given by Equation 5.10:

$$\frac{E_{\text{cor, Pa}}}{E_{\text{cor, Br}}} = \frac{F_{\text{theo, Pa}}}{F_{\text{theo, Br}}} = 10^{\frac{0.39}{2.5} A_V R_\infty^\alpha \left(\left[\frac{1}{3^2} - \frac{1}{u^2} \right]^\alpha - \left[\frac{1}{4^2} - \frac{1}{u^2} \right]^\alpha \right)}. \quad (5.20)$$

We now expressed the ratio of the extinction factors $\frac{E_{\text{cor, Pa}}}{E_{\text{cor, Br}}}$, given by the ratio of the theoretical fluxes $\frac{F_{\text{theo, Pa}}}{F_{\text{theo, Br}}}$ and the ratio of the observed fluxes $\frac{F_{\text{obs, Pa}}}{F_{\text{obs, Br}}}$, for Paschen and Brackett lines in terms of the extinction value A_V and the exponent α of the reddening power law.

5.4 Application to classical T Tauri stars

The theories described in the previous sections are used in this thesis to examine the temperature T and electron density n_e in the emitting gas (see Section 5.4.1) as well as the extinction value A_V and the exponent α of the reddening power law (see Section 5.4.2) using a data set of classical T Tauri stars (see Section 3.2).

5.4.1 The temperature T and the electron density n_e in the emitting gas

Using the case B models for the level populations N_{nl} in recombining hydrogen as described in Section 5.2, the physical conditions in terms of the temperature T and the electron density n_e in the emitting gas can be determined. The models and the observed ratios are statistically

compared using the reduced χ^2 (as in Bary et al. 2008).

If the densities are high, optical depth effects complicate the interpretation of line measurements and radiative transfer modelling is required. In CTTSs the Balmer emission lines, especially $H\alpha$, often seem to be optically thick (Kurosawa et al. 2006). Thus, for these lines the case B assumption of optically thin gas is likely not fulfilled. The optical depth is lower for near-infrared hydrogen lines (Folha & Emerson 2001). Hence, I use the Paschen and Brackett lines of the sample objects for the examination of temperature T and electron density n_e in the emitting hydrogen gas, although the spectra also contain the Balmer lines.

Before the measured line fluxes can be used they need to be dereddened. As described in Section 5.3 the observed fluxes F_{obs} are dereddened using Equations 5.16 and 5.17:

$$F_{\text{unred}} = F_{\text{obs}} \cdot 10^{\frac{0.39}{2.5} A_V \lambda^{-1.84}}. \quad (5.21)$$

The extinction factor E_{cor} contains the extinction value A_V , a quantity that is individual for each object. I searched the literature for extinction values A_V for each object. These are summarised in Table 5.4 with the used value marked in boldface. The main methods to determine A_V are photometry, fitting the spectral energy distribution, and spectroscopic template comparison requiring the knowledge of the spectral type of the object and the strength of the veiling. Spectroscopic template comparison usually yields more accurate results, because the reddening can be determined using several lines. Hence, I decided to use spectroscopically determined values wherever possible. For my further analysis, the literature values were used, although I could determine the extinction values from the spectra myself. This was planned to be done later on in the thesis, but unfortunately there was not enough time left.

5.4.2 The extinction value A_V and the exponent α of the reddening power law

For a few of the objects in the sample the conditions in the environment allow several hydrogen lines of the Paschen and Brackett series with a common upper level u to be formed (see Tables C.1 and C.2). Measuring the flux ratios of these lines allows the fitting of either the extinction value A_V for a fixed exponent α of the reddening power law or of both A_V and α using Equation 5.20.

Table 5.4: Literature extinction values A_V for each object.

Object	Extinction values A_V in mag			
S CrA	0.41 ^k	1.00 ^u	2.00 ^t	
TW Hya	0.00 ^d			
EX Lup	0.00 ^a	0.00 ⁱ		
GQ Lup	0.50 ^r	0.95 ^a		
HO Lup	1.25 ^a	1.60 ^e		
IM Lup [†]	0.80 ^c	0.98 ^a		
MV Lup [†]	0.07 ⁱ	0.32 ^h	0.36 ^j	
RU Lup	0.07 ⁿ	0.20 ^g	1.28 ^a	
MP Mus	0.17 ^g	0.70 ^s		
V853 Oph	0.14 ⁱ	0.29 ^k	2.30 ^f	
V2058 Oph	1.43 ⁱ	2.20 ^l	4.50 ^f	
V2062 Oph	1.16 ^b	1.38 ⁱ	3.30 ^l	4.40 ^f
V2129 Oph	0.60 ^o	0.60 ⁱ	1.60 ^l	2.30 ^f
V2251 Oph	1.89 ⁱ	2.30 ^l		
V2252 Oph	0.57 ⁱ	3.80 ^f	1.96 ^b	
VV Sco	0.50 ^l			
V895 Sco	0.83 ⁱ	1.67 ^b		
V1279 Sco	0.00 ^f	0.80 ^c	0.82 ^a	2.26 ⁱ
V4046 Sgr	0.00 ^m	0.00 ^p		
Sz77 [†]	0.79 ^a	0.90 ^c		

Notes. The used value of A_V is marked boldface; (†) shows no Paschen and Brackett lines, no dereddening needed, so no decision for a value.

References. (a) Hughes et al. (1994); (b) Cohen & Kuhl (1979); (c) Finkenzeller & Basri (1987); (d) Rucinski & Krautter (1983); (e) Hamann & Persson (1992); (f) Evans et al. (2009); (g) Mamajek et al. (2002); (h) Wichmann et al. (1997); (i) Sartori et al. (2003); (j) Krautter et al. (1997); (k) McCabe et al. (2006); (l) McClure et al. (2010); (m) Yang et al. (2012); (n) Herczeg et al. (2005); (o) Donati et al. (2007); (p) Stempels & Gahm (2004); (q) Stempels & Piskunov (2002); (r) Seperuelo Duarte et al. (2008); (s) Cortes et al. (2009); (t) Currie & Sicilia-Aguilar (2011); (u) Prato et al. (2003).

Chapter 6

Results and Discussion

In this chapter I present the analysis of the hydrogen emission line ratios measured for a sample of classical T Tauri stars. The measurement of the line fluxes is described in Section 5.1. Sections 6.1 and 6.2 deal with the determination of the temperature T and the electron density n_e in the emitting gas and the conclusions thereof, while the reddening is examined in Section 6.3 with conclusions thereof presented in Section 6.4.

6.1 The temperature T and the density n_e in the emitting gas

From the observed and dereddened line fluxes (see Section 5.4.1) for each object three different series of line ratios can be formed depending on the presence of the lines of the Paschen and Brackett series (see also Tables C.1 and C.2 in Appendix C.1): Pan_{up} , where n_{up} is the upper level of the transition, to $\text{Pa}\beta$ (15 of 20 objects), $\text{Br}\gamma$ to Pan_{up} (13), and $\text{Br}n_{\text{up}}$ to $\text{Br}\gamma$ (6). For the Paschen series, the highest used upper level is $n_{\text{up}} = 14$, while it is $n_{\text{up}} = 17$ for the Brackett series. The analysis uses case B models (see also Sections 5.2 and 5.4.1). Their sensitivity to the parameters temperature T and electron density n_e is illustrated in Figure 6.1. Here, the three measured series of line ratios of RU Lup are shown together with the best-fit models as well as four neighbouring models. The best-fit model is determined via calculating reduced χ^2 values between the data and the case B models. For RU Lup, the best-fit models are $T = 1000$ K and $n_e = 10^{10} \text{ cm}^{-3}$ for the Pan_{up} to $\text{Pa}\beta$ line ratios and $T = 3000$ K and $n_e = 10^9 \text{ cm}^{-3}$ for the $\text{Br}\gamma$ to Pan_{up} and the $\text{Br}n_{\text{up}}$ to $\text{Br}\gamma$ line ratios. These fit results are a good example of the range found predominantly (see below). The plots on the left hand side show models for the best-fit electron density and varying temperature, while the plots on the right show models for the best-fit temperature and varying electron density. From Figure 6.1 the following statements concerning the temperature and density sensitivity of the case B models can be deduced:

- For the Pan_{up} to $\text{Pa}\beta$ line ratios, the temperature sensitivity is most noticeable at the midrange n_{up} values (8 to 11) where the separation between the models is largest, while the higher or lower values only provide weak constraints. The density sensitivity is less clear, but there also is a noticeable spread between the models.
- For the $\text{Br}\gamma$ to Pan_{up} line ratios, the temperature and density sensitivity is most noticeable at the higher n_{up} values ($n_{\text{up}} \geq 10$) where the individual models show large differences. At lower n_{up} values the differences between the models are quite small.
- For the $\text{Br}n_{\text{up}}$ to $\text{Br}\gamma$ line ratios, the temperature sensitivity is most noticeable at the lower n_{up} values ($n_{\text{up}} < 15$), while the models converge for higher n_{up} values. A similar picture, though less clear, is visible for the density sensitivity.

The data of all objects is compared to the case B models to determine the temperature T and the density n_e in the emitting gas. Since two parameters are to be determined, there should be at least two ratios, so the two objects showing only $\text{Pa}\beta$ and $\text{Pa}\gamma$ (V2129 Oph, V1279 Sco) due

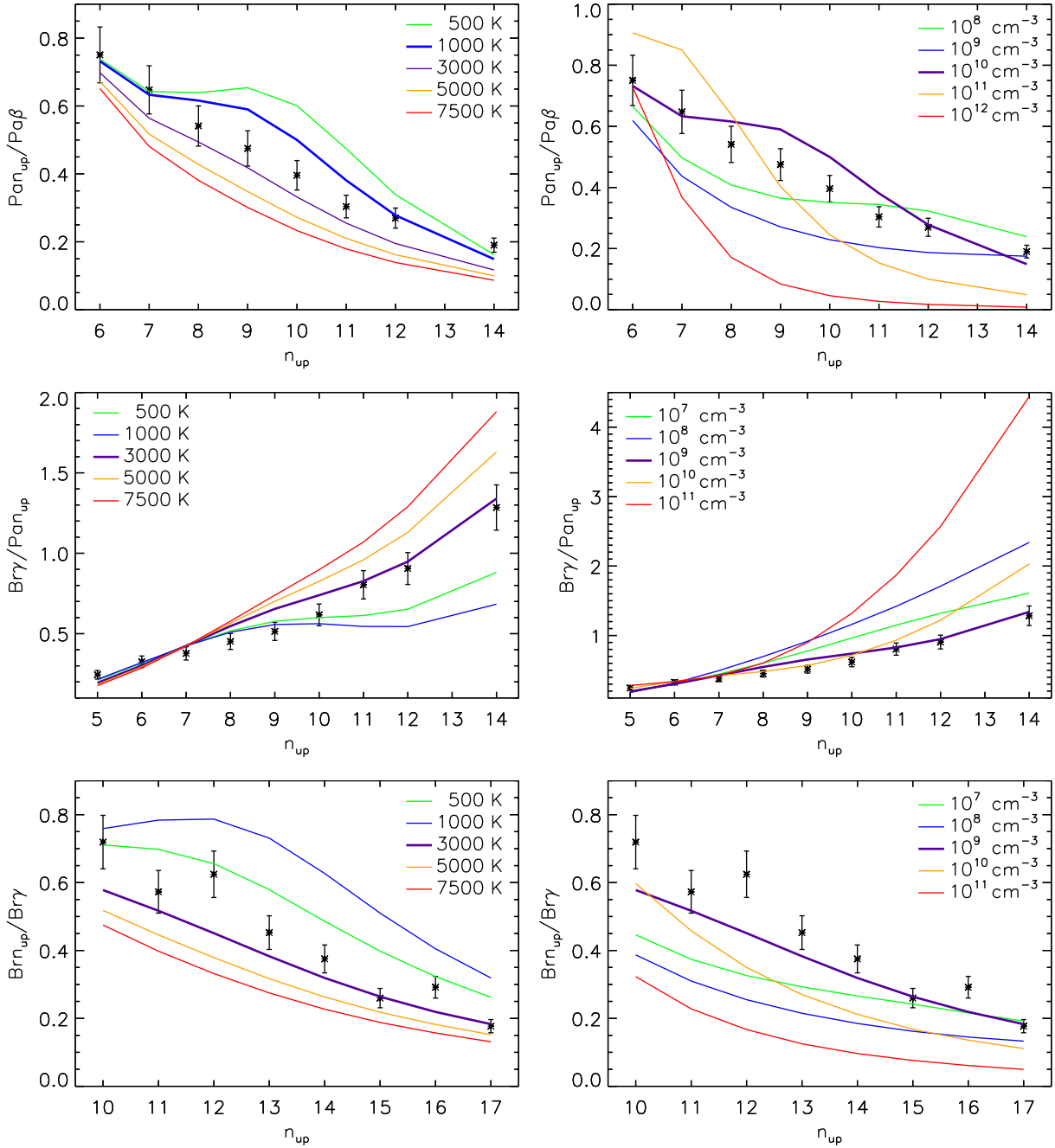


Figure 6.1: The sensitivity of the case B models illustrated using the example of the data of RU Lup. The best-fit model, indicated by a thicker line in each plot, has $T = 1000$ K and $n_e = 10^{10} \text{ cm}^{-3}$ for the Pan_{up} to $\text{Pa}\beta$ line ratios (*top*), $T = 3000$ K and $n_e = 10^9 \text{ cm}^{-3}$ for the $\text{Br}\gamma$ to Pan_{up} line ratios (*middle*), and for the Brn_{up} to $\text{Br}\gamma$ line ratios (*bottom*). For the plots on the *left*, models with the best-fit density and varying temperature are plotted (see legend). For the plots on the *right*, models with the best-fit temperature and varying density are plotted (see legend).

to their low accretion rate are not included. Figures 6.2 to 6.16 show the available series of line ratios for each object together with the five case B models with the smallest reduced χ^2 values. The figure legends state the temperature T and the electron density n_e for each model. For each object and each series of line ratios the models that best fit the data and their reduced χ^2 values are summarised in Table 6.1. The reduced χ^2 values of all models plotted in the figures are available in Appendix C.4. The corresponding table for each object is given in the figure caption and in the last column of Table 6.1.

Table 6.1: The temperature T and the electron density n_e of the best fitting model for each series of line ratios.

Object (1)	Figure (2)	Pan _{up} /Pa β		Br γ /Pan _{up}		Match Br γ /Pa δ		Brn _{up} /Br γ		Table of other χ^2_{red} (13)	
		T in K (3)	n_e in cm ⁻³ (4)	χ^2_{red} (5)	T in K (6)	n_e in cm ⁻³ (7)	χ^2_{red} (8)	Br γ /Pa δ (9)	T in K (10)	n_e in cm ⁻³ (11)	χ^2_{red} (12)
S CrA	6.2	1000	10 ¹⁰	2.57	3000	10 ¹⁰	2.03	y	5000	10 ⁹	3.19
TW Hya	6.3	7500	10 ¹²	0.86	30000	10 ¹⁴	2.42	y			
EX Lup	6.4	1000	10 ¹¹	2.63	500	10 ⁹	25.90	n			
GQ Lup	6.5	10000	10 ¹⁰	0.16	7500	10 ¹⁰	0.51	y			
HO Lup	6.6	5000	10 ¹⁰	0.51	1000	10 ⁹	11.67	n	5000	10 ¹⁰	0.25
RU Lup	6.7	1000	10 ¹⁰	3.10	3000	10 ⁹	2.36	y	3000	10 ⁹	2.80
MP Mus	6.8	5000	10 ⁸	0.29	12500	10 ⁹	6.97	n			
V853 Oph	6.9	1000	10 ¹⁰	5.61							
V2058 Oph	6.10	3000	10 ¹⁰	3.32	1000	10 ⁹	5.33	n	5000	10 ¹⁰	6.45
V2062 Oph	6.11	5000	10 ¹⁰	1.04	1000	10 ⁹	15.22	n	500	10 ¹¹	17.32
V2251 Oph	6.12	3000	10 ⁷	0.74	20000	10 ⁹	10.76	n			
V2252 Oph	6.13	12500	10 ¹⁰	1.10	3000	10 ⁹	13.30	n			
VV Sco	6.14	1000	10 ⁷	2.55	3000	10 ⁸	1.36	y			
V895 Sco	6.15	5000	10 ¹⁰	0.60	5000	10 ¹⁰	0.45	y	7500	10 ¹⁰	0.71
V4046 Sgr	6.16	1000	10 ¹⁴	24.65	7500	10 ¹⁴	18.13	y			

Notes. Column 2: label of the figure showing the data and the models; column 9: 'y', if observed and predicted Br γ /Pa δ ratio match within the uncertainties (see text for details); column 13: label of the table showing the χ^2_{red} of all models in the corresponding figure.

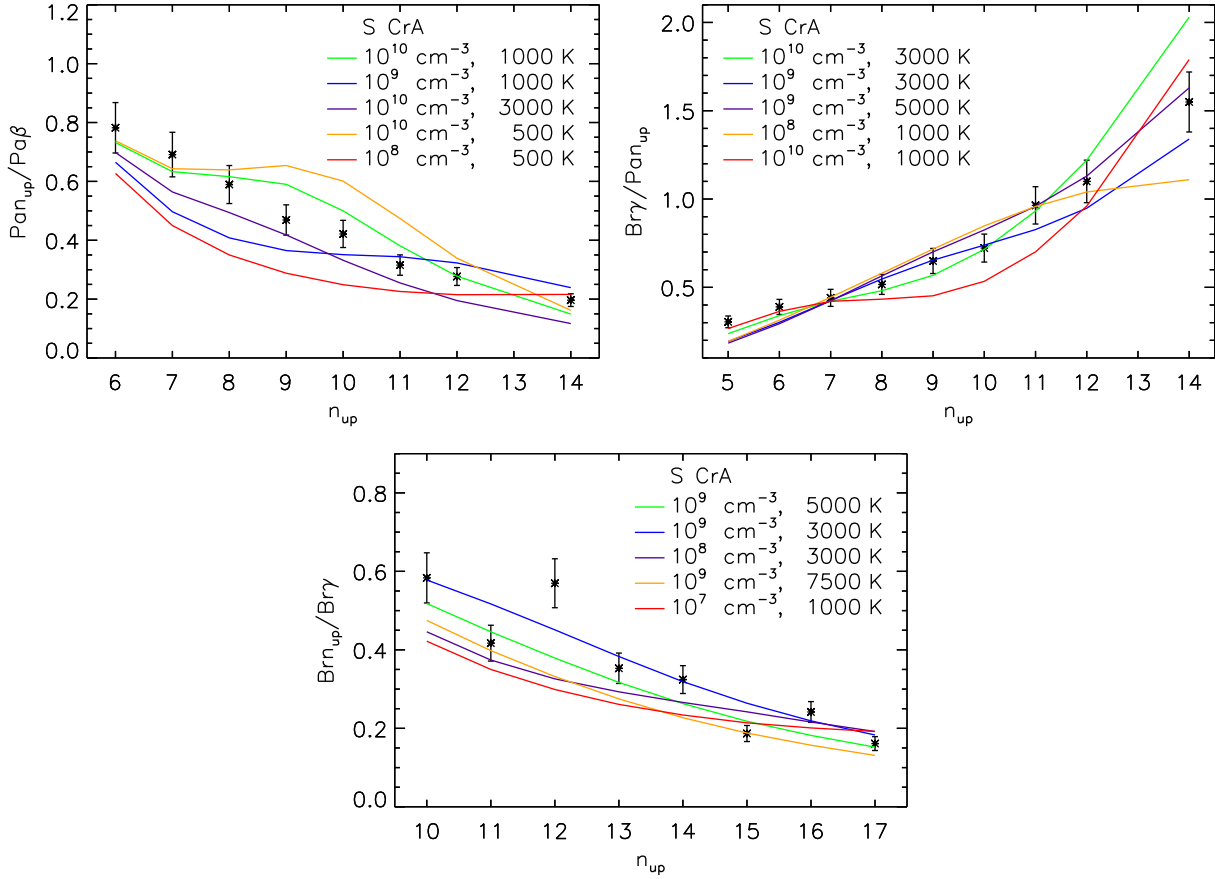


Figure 6.2: The observed line ratios of the Paschen lines using $Pa\beta$ as reference line (*top left*), the Paschen lines using $Br\gamma$ as reference line (*top right*), and the Brackett lines using $Br\gamma$ as reference line (*bottom*) of S CrA together with the five case B models with lowest χ_{red}^2 . The legend indicates the electron density n_e and temperature T for each model with χ_{red}^2 increasing from *green* to *red*. The χ_{red}^2 are summarised in Table C.6 in Appendix C.4.

The temperatures T of the emitting gas found from the three different series of line ratios predominantly lie between 500 K and 5000 K with a few cases of higher temperatures. The electron densities n_e predominately fall in the range of 10^9 cm^{-3} to 10^{10} cm^{-3} . Notable exceptions are TW Hya, with densities of 10^{12} cm^{-3} and 10^{14} cm^{-3} and temperatures of 7500 K and 30 000 K, and V4046 Sgr, with an electron density of 10^{14} cm^{-3} and temperatures of 1000 K and 7500 K. For TW Hya (Figure 6.3), the five best-fit models are very serried over most of the n_{up} range, while there are only 3 and 4 data points, respectively, for V4046 Sgr (Figure 6.16).

The best-fit reduced χ^2 values for all individual series of line ratios and objects vary between 0.16 and 24.65. In most cases the reduced χ^2 value is significantly higher for the $Br\gamma$ to Pan_{up} line ratios than for the Pan_{up} to $Pa\beta$ line ratios. A statistically good fit, i.e. $\chi_{red}^2 \approx 1$, is only reached in very few cases. A too small χ_{red}^2 points towards overestimated uncertainties. This may indeed be the case for ratios where both lines are in the NIR arm ($Pa\beta$, $Pa\gamma$, and all Brackett lines). The uncertainty of a ratio contains a component for the uncertainty of the relative flux calibration between the arms. The NIR arm was split into three arms which are treated individually. This might cause an overestimation of the uncertainty, but affects only one ratio in the Pan_{up} to $Pa\beta$ line ratio series and two ratios in the $Br\gamma$ to Pan_{up} line ratio series, while it affects all Brn_{up} to $Br\gamma$ line ratios. The overall effect seems to be limited since the χ_{red}^2 values for the Brn_{up} to $Br\gamma$ line ratio series spread between 0.25 and 17.32. A χ_{red}^2 much larger than 1 can have three reasons: an error in the measurement technique, underestimated uncertainties, or the used model is inappropriate to explain the data. I will come back to possible errors in the measurement technique later on in this section. An underestimation of the uncertainties

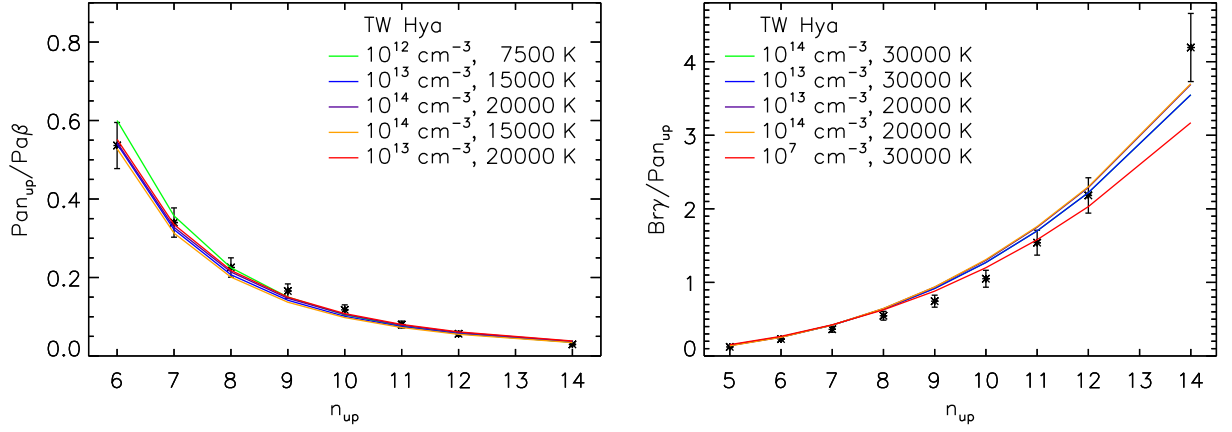


Figure 6.3: The observed line ratios of the Paschen lines using $Pa\beta$ as reference line (*left*) and the Paschen lines using $Br\gamma$ as reference line (*right*) of TW Hya together with the five case B models with lowest χ_{red}^2 . The legend indicates the electron density n_e and temperature T for each model with χ_{red}^2 increasing from *green* to *red*. The χ_{red}^2 are summarised in Table C.7 in Appendix C.4.

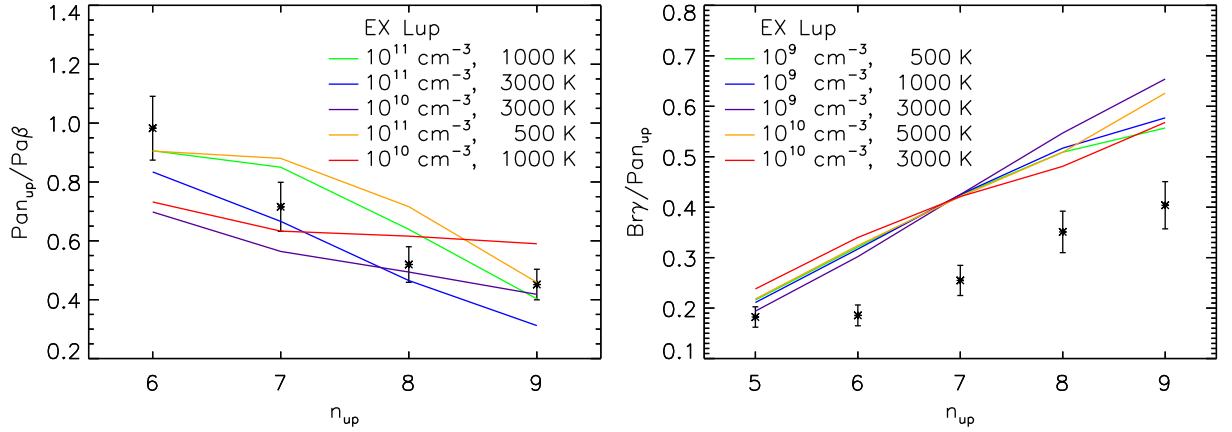


Figure 6.4: As Figure 6.3, but for EX Lup. The χ_{red}^2 are summarised in Table C.8 in Appendix C.4.

seems unlikely because the estimation of the uncertainties was done the same way for all ratios but still the resulting χ_{red}^2 values show a large spread. Finally, the model being inappropriate remains. This possibility will be discussed in Section 6.2.

The values for the temperature T and the electron density n_e obtained from the three different series of line ratios for each individual object do not offer a consistent picture for all objects. While the difference in the found electron density n_e never exceeds two model steps, i.e. two orders of magnitude, the temperature T differs by two or less model steps only for 8 of the 14 objects that have two or three series available. One model step in temperature corresponds to a change by about a factor of 1.5.

As pointed out in Section 5.3, for line ratios that have a common upper level the ratio is independent of the temperature and density if the gas is optically thin, as assumed by the case B models. The ratio $Br\gamma/Pa\delta$ with $n_{up} = 7$, which is part of the $Br\gamma$ to Pan_{up} line ratio series, is the only ratio involved for which this is the case. The middle panel of Figure 6.1 shows that all models displayed give a value of ~ 0.4 for $Br\gamma/Pa\delta$ with no visible scatter for fixed density and only a very small scatter for fixed temperature. This is also apparent for all models plotted in Figures 6.2 to 6.16 for the $Br\gamma$ to Pan_{up} line ratio series. Deviations from this value can either be caused by optical depth effects, i.e. the gas is not optically thin as assumed in case B, or by reddening. Inspection of the measured and dereddened $Br\gamma/Pa\delta$ ratios presented in Figures 6.2

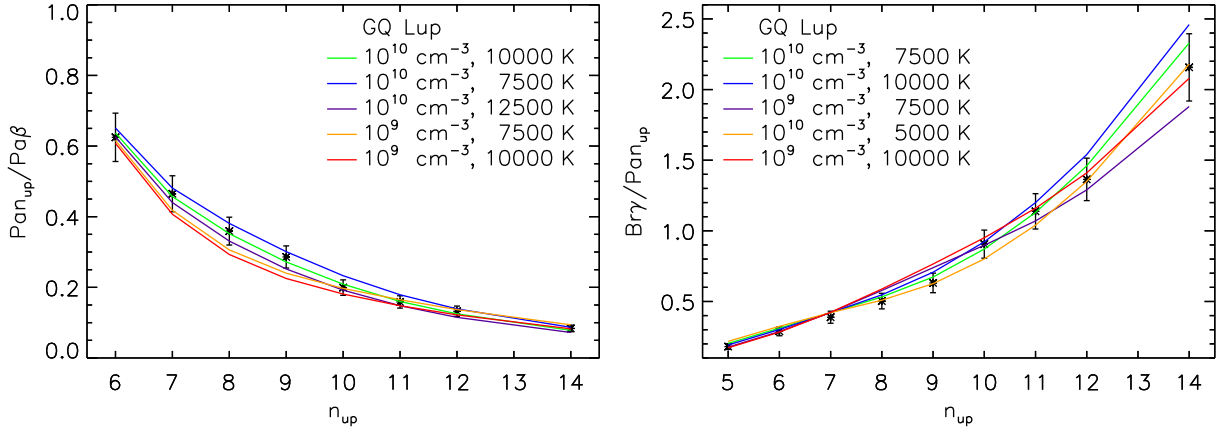


Figure 6.5: As Figure 6.3, but for GQ Lup. The χ_{red}^2 are summarised in Table C.9 in Appendix C.4.

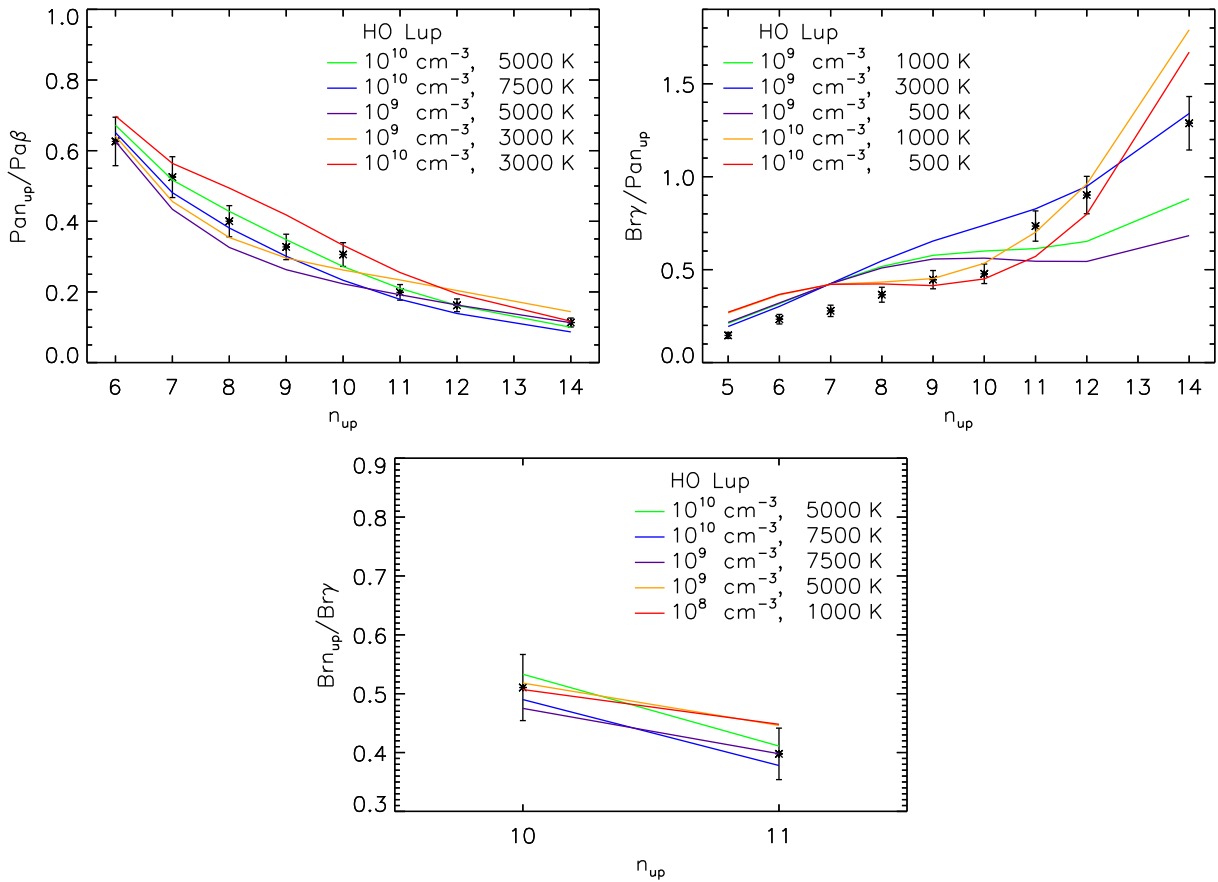


Figure 6.6: As Figure 6.2, but for HO Lup. The χ_{red}^2 are summarised in Table C.10 in Appendix C.4.

to 6.16 reveals that these match with the models only in a few cases. While both of the reasons stated for the cause of this deviation are possible, an incorrect dereddening is very likely to play a major role. Most importantly, the choice of the extinction value A_V will have a significant impact on the values of the ratios used for the analysis. The spread in the A_V values stated in the literature for the objects in the sample can be as high as 3.2 mag. Thus, a wrongly chosen A_V automatically causes a deviation of the observed ratio from the predicted one. This was already illustrated in Figure 5.7 in Section 5.3 showing the effect of different extinction values on the ratios of Paschen and Brackett lines with a common upper level. An extinction value different by 1 mag can cause the reddened ratio to be different by up to 0.5. The effect is stronger

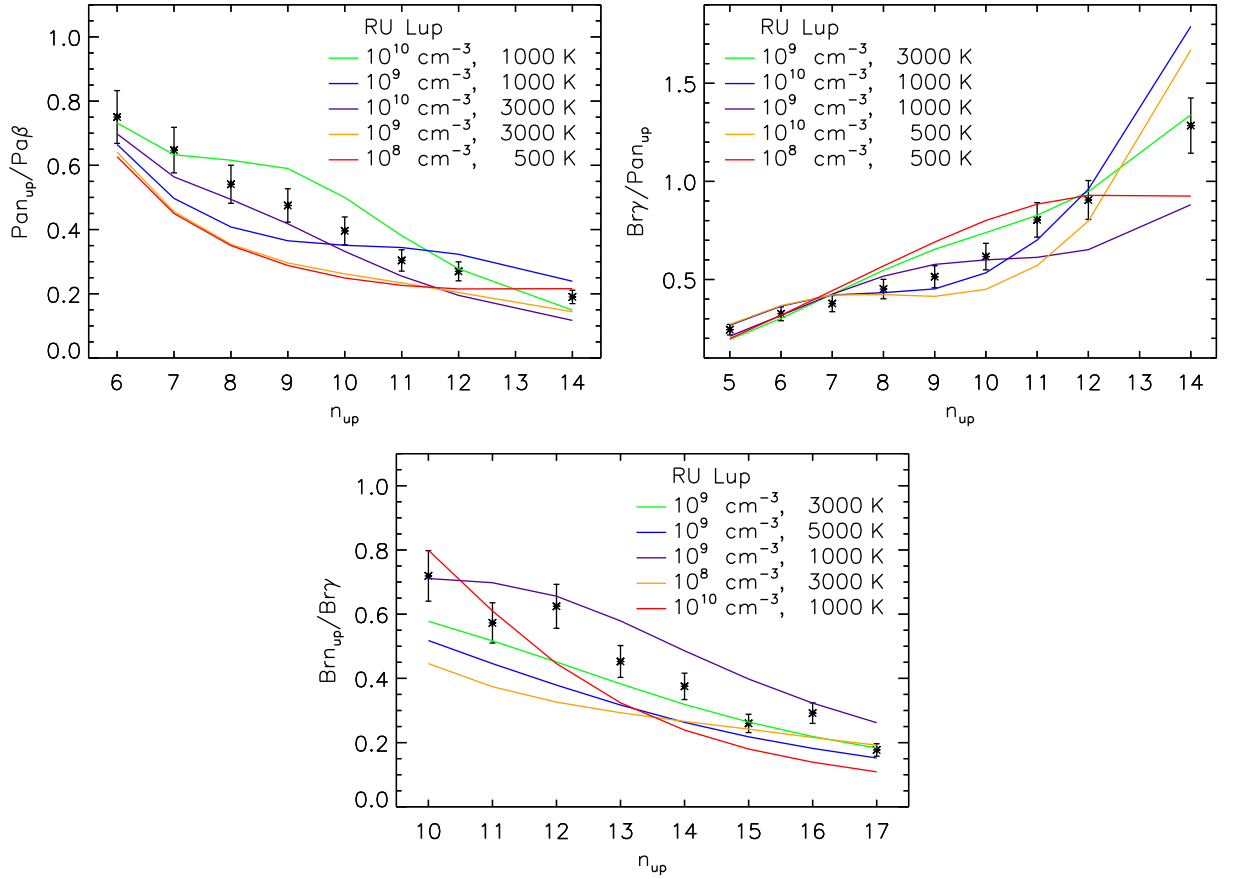


Figure 6.7: As Figure 6.2, but for RU Lup. The χ_{red}^2 are summarised in Table C.11 in Appendix C.4.

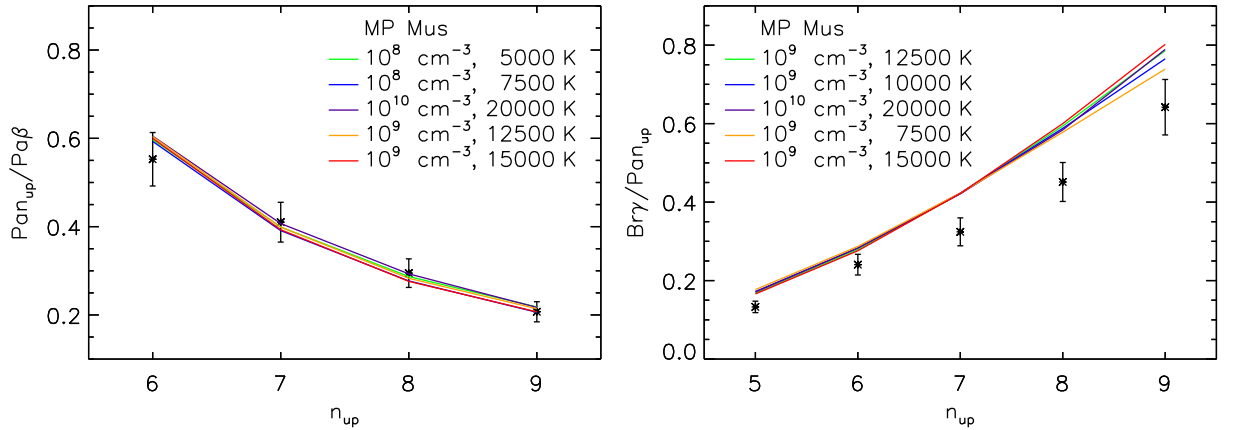


Figure 6.8: As Figure 6.2, but for MP Mus. The χ_{red}^2 are summarised in Table C.12 in Appendix C.4.

for lower extinction values. The reduced χ^2 values of the fits to the $Br\gamma$ to Pan_{up} line ratio series are unsurprisingly quite high for those objects where the observed $Br\gamma/Pa\delta$ ratio does not match up with the predicted one within the uncertainties (indicated with a 'n' in column 9 of Table 6.1). These objects are in most cases also the objects that show a large spread in the temperatures from the different series of line ratios. For these objects a main reason for the high χ_{red}^2 seems indeed to be an error in the measurement technique, namely a wrong dereddening, if the assumption of optically thin conditions in the gas is correct.

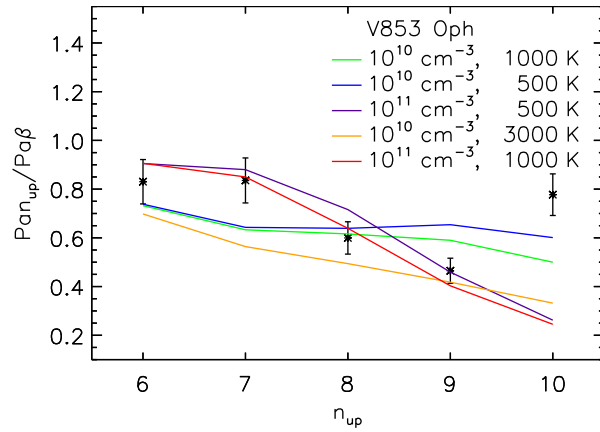


Figure 6.9: The observed line ratios of the Paschen lines using $\text{Pa}\beta$ as reference line of V853 Oph together with the five case B models with lowest χ_{red}^2 . The legend indicates the electron density n_e and temperature T for each model with χ_{red}^2 increasing from *green* to *red*. The χ_{red}^2 are summarised in Table C.13 in Appendix C.4.

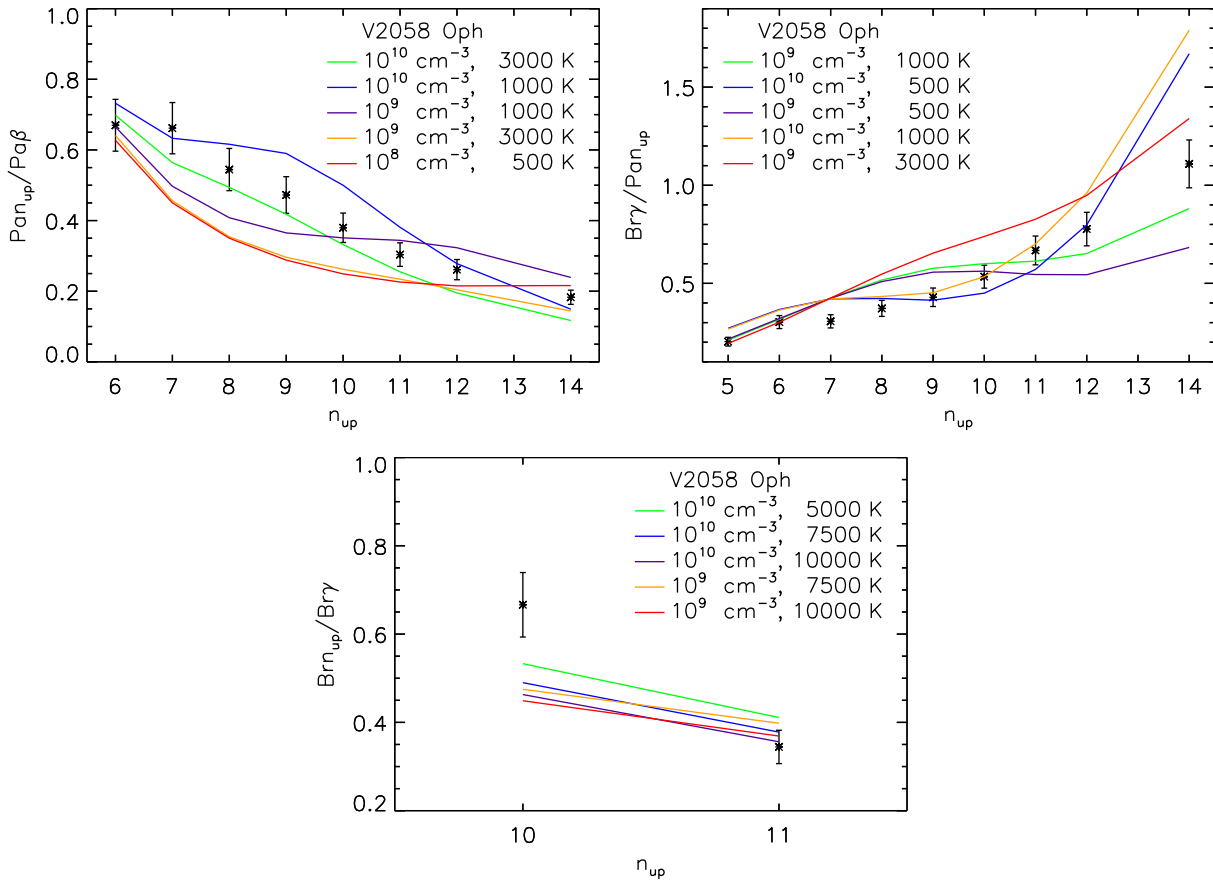


Figure 6.10: As Figure 6.2, but for V2058 Oph. The χ_{red}^2 are summarised in Table C.14 in Appendix C.4.

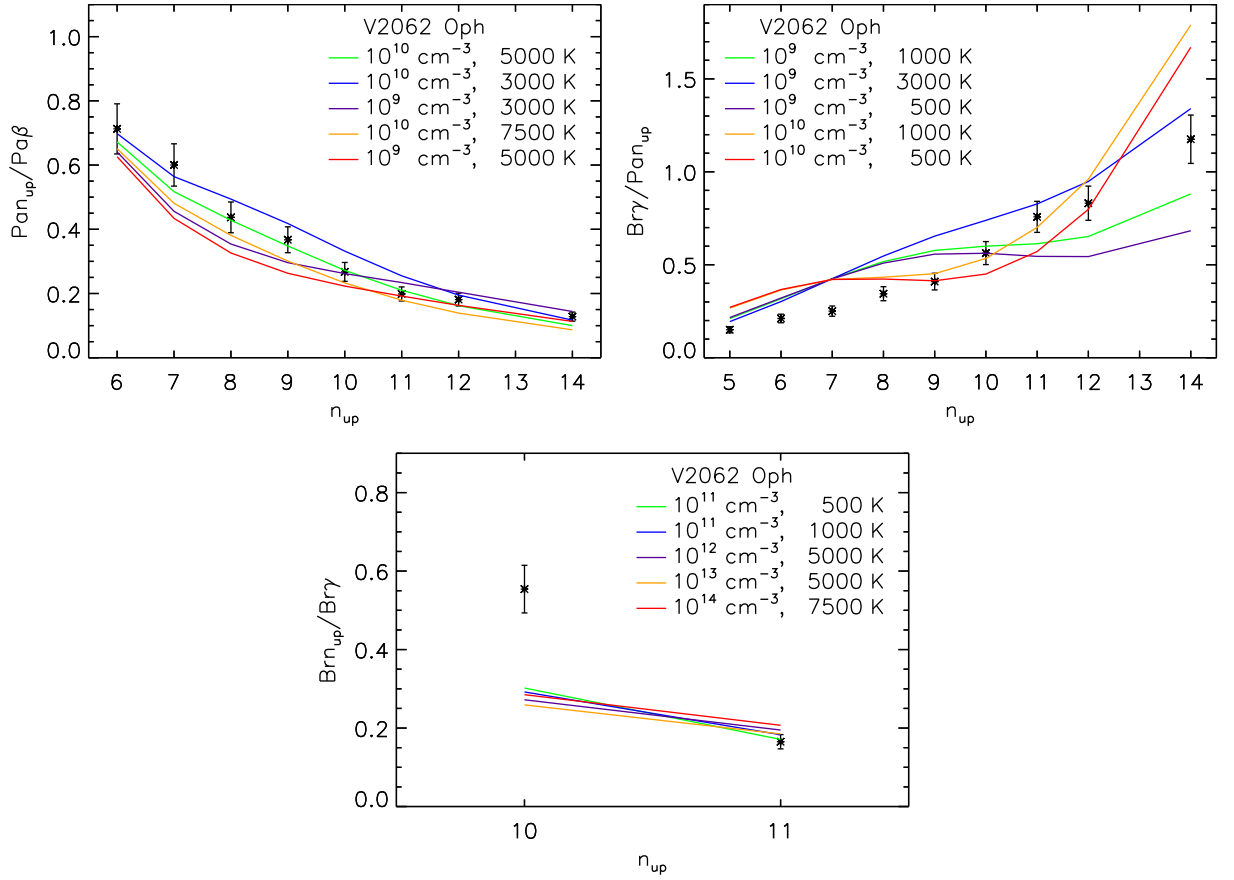


Figure 6.11: As Figure 6.2, but for V2062 Oph. The χ_{red}^2 are summarised in Table C.15 in Appendix C.4.

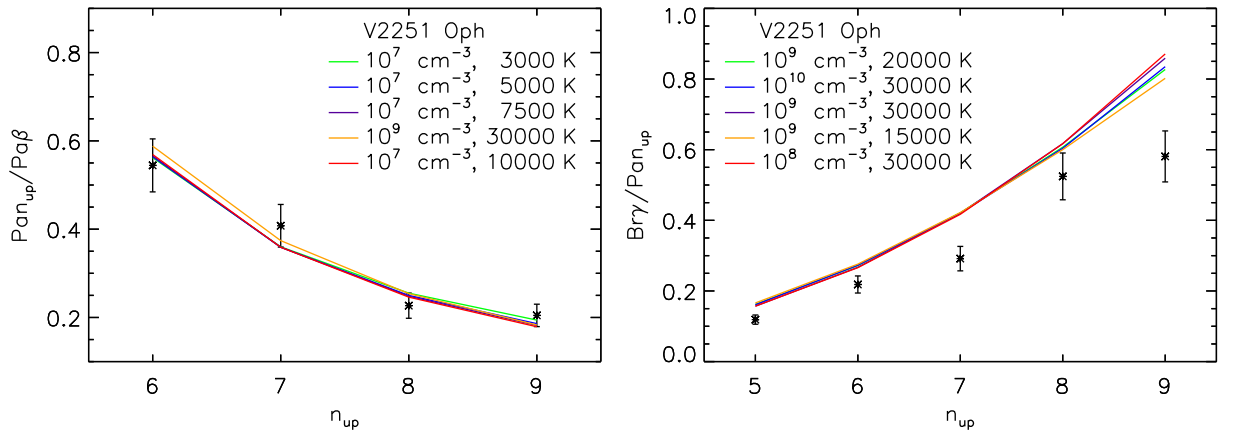


Figure 6.12: As Figure 6.3, but for V2251 Oph. The χ_{red}^2 are summarised in Table C.16 in Appendix C.4.

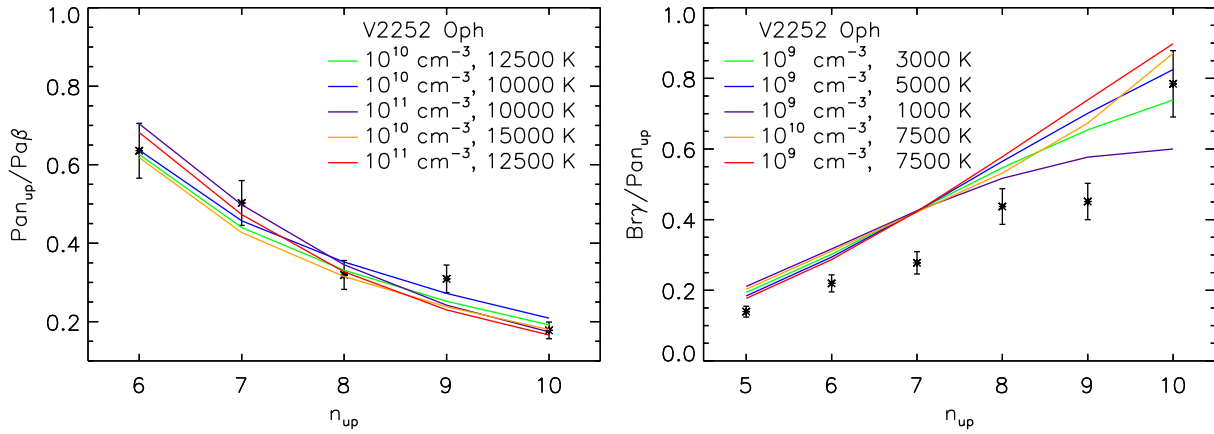


Figure 6.13: As Figure 6.3, but for V2252 Oph. The χ_{red}^2 are summarised in Table C.17 in Appendix C.4.

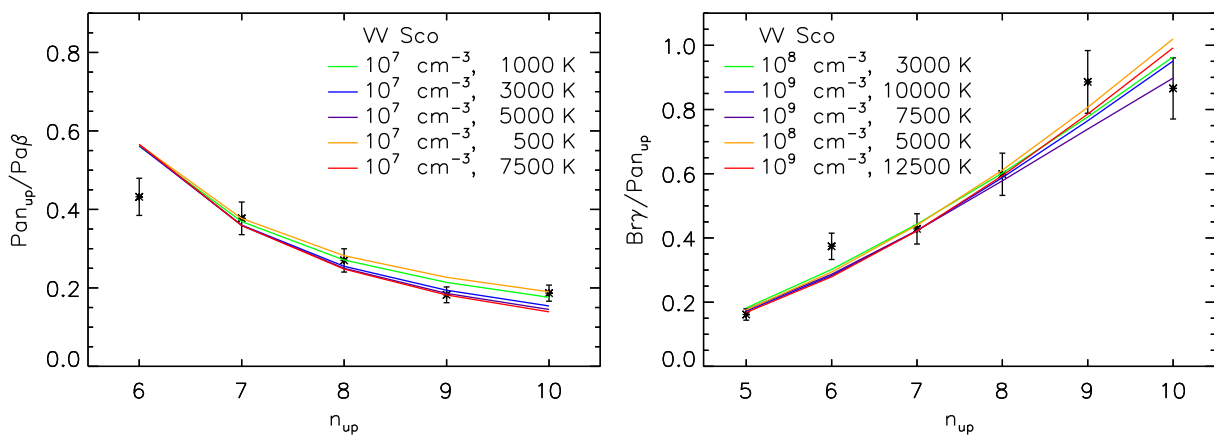


Figure 6.14: As Figure 6.3, but for VV Sco. The χ_{red}^2 are summarised in Table C.18 in Appendix C.4.

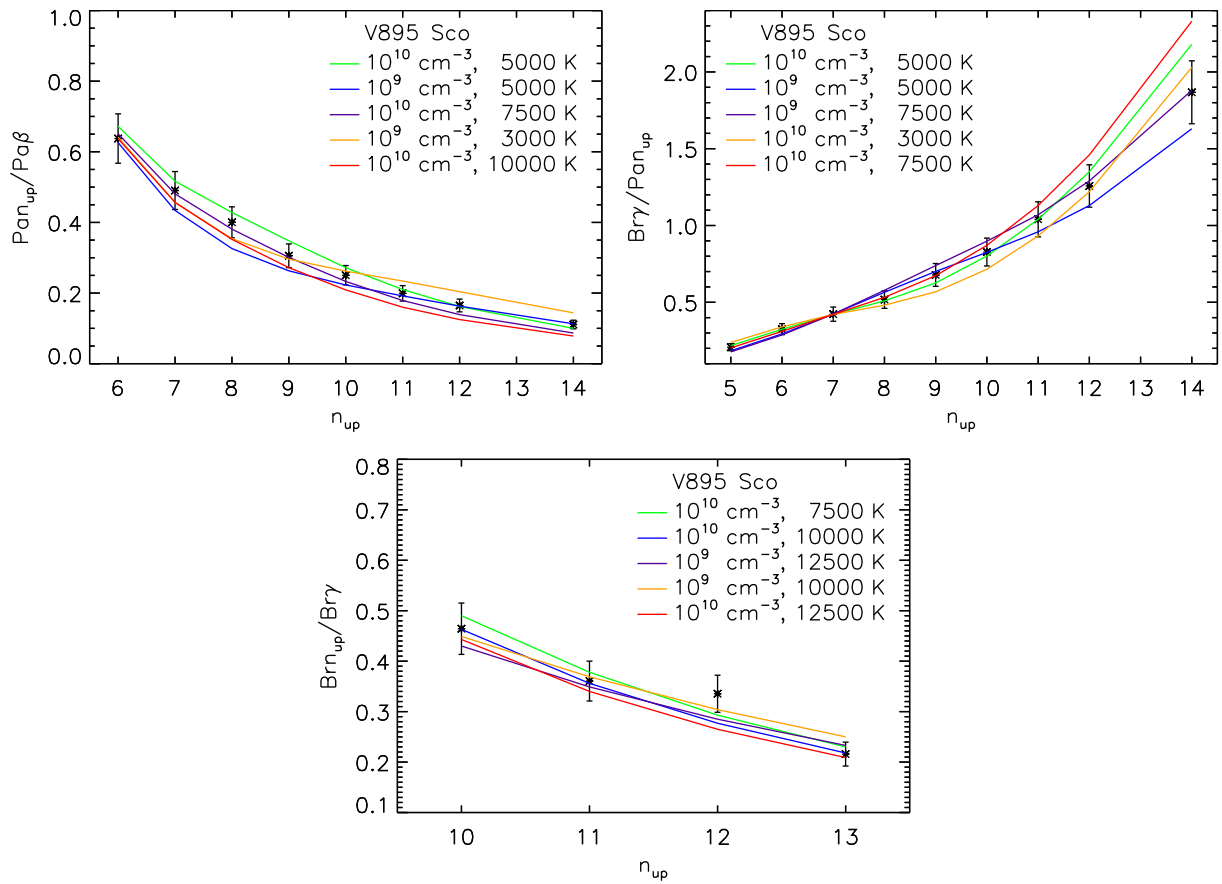


Figure 6.15: As Figure 6.2, but for V895 Sco. The χ_{red}^2 are summarised in Table C.19 in Appendix C.4.

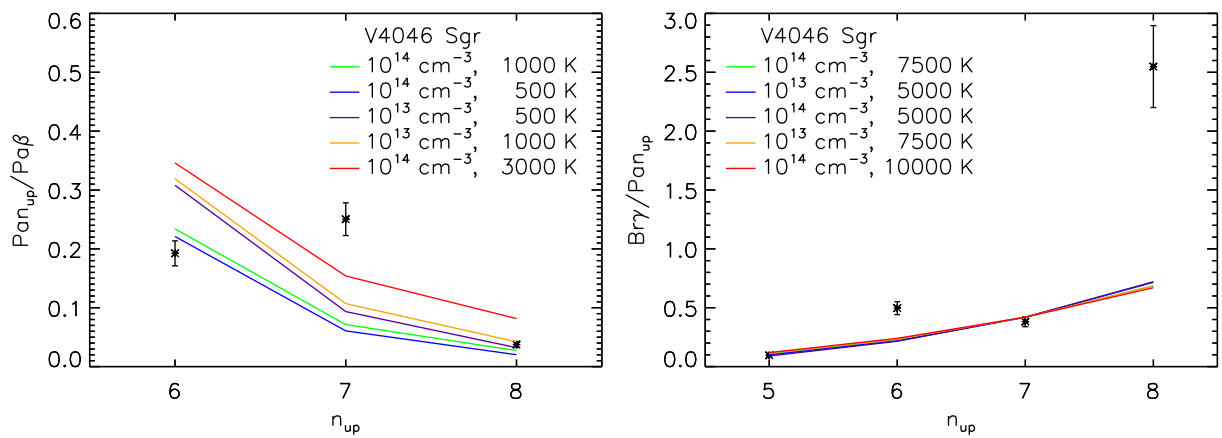


Figure 6.16: As Figure 6.3, but for V4046 Sgr. The χ_{red}^2 are summarised in Table C.20 in Appendix C.4.

6.2 Discussion of the physical conditions in the emitting gas of classical T Tauri stars

In contrast to the results of Bary et al. (2008) who find that the case B models provide a statistically good fit to their data (χ_{red}^2 of the best-fit models between 0.44 and 0.93), in my sample this is only true for a few cases. If the explanation given above is correct that the high reduced χ^2 values for several objects are caused by incorrect dereddening, one could exclude those objects from the analysis. This reduces the sample to 7 objects (indicated with a 'y' in column 9 of Table 6.1) and the spread in the reduced χ^2 values lowers to 0.16 to 3.19, except for V4046 Sgr with values of $\chi_{\text{red}}^2 = 24.65$ and $\chi_{\text{red}}^2 = 18.13$ for only three and four data points, respectively, the lowest number of all objects in the subsample. For the other 6 objects still $\chi_{\text{red}}^2 > 2$ in half of the cases. While this might be caused by underestimated uncertainties or a reflection of the relatively coarse model grid, the reason also could be that the case B models are inappropriate to describe the data.

Looking at the temperatures and densities I find, the spread covers the whole model range in temperatures from 500 K to 30 000 K, while the densities vary between 10^7 cm^{-3} and 10^{14} cm^{-3} , the last highest density of the model grid. The results for the temperature from the three series are inconsistent for half of the objects. For the subsample which shows a good match between the observed and the predicted $\text{Br}\gamma/\text{Pa}\delta$ ratio, the spread is almost the same, but the temperature results from the different series are more consistent with only two objects (TW Hya and V4046 Sgr) having temperatures differing by more than two model steps. Bary et al. (2008) find consistent temperatures, $T = 1000 \text{ K}$ and $T = 500 \text{ K}$, and densities, $n_e = 10^{10} \text{ cm}^{-3}$, from the three series of line ratios in their analysis of the average line ratios of 15 objects. The case B models have been used in a number of other studies to examine the physical conditions in the emitting gas of CTTS in this sample. For TW Hya, Vacca & Sandell (2011) find $T = 20\,000 \text{ K}$ and $n_e \sim 10^{13} \text{ cm}^{-3}$. For RU Lup, Podio et al. (2008) find $T = 10\,000 \text{ K}$ and n_e between 10^3 cm^{-3} and 10^7 cm^{-3} . For EX Lup, Kóspál et al. (2011) find $T = 10\,000 \text{ K}$ and $n_e \sim 10^7 \text{ cm}^{-3}$. While the values for TW Hya fall in the range I find, this is not the case for the other two, albeit my values for EX Lup should be treated with caution because the dereddening seems to be inadequate.

The spread in the physical conditions deduced from comparison to case B models in my study and those mentioned above is quite large, seven magnitudes in density and temperatures from 1000 K to 30 000 K. This raises the question whether the case B scenario really is the appropriate model to analyse the physical conditions in the formation region of hydrogen lines in CTTS, as also pointed out by Edwards et al. (2013).

Setting aside the doubts whether case B is the correct description of the data or not, it is nevertheless worth to take a look at the implications of the physical conditions found. The case B scenario makes no assumptions about where the emission is formed, e.g. in a wind, magnetically channelled accretion flow, or at the disk rim. In the magnetospheric accretion model for CTTS (see also Section 2.2), the current understanding of the accretion processes in CTTS, the emission is thought to mainly originate in the accretion funnel in which the gas is freely falling onto the star. When comparing the results to these models, one has to keep in mind that other regions contribute to the overall hydrogen emission, e.g. winds (Whelan et al. 2004).

These models predict for a fiducial mass accretion rate of $\dot{M}_{\text{ac}} = 10^{-7} M_{\odot} \text{ yr}^{-1}$ a hydrogen density in the accretion flow of about 10^{12} cm^{-3} to 10^{13} cm^{-3} (Martin 1996; Muzerolle et al. 1998a, 2001). The ionisation fraction is about 10^{-2} to 10^{-3} (Martin 1996), resulting in expected electron densities of 10^9 cm^{-3} to 10^{11} cm^{-3} . As shown in Table 6.1, for most objects the densities found from the three series of line ratios fall into this range. Notable exceptions are VV Sco, for which the densities from all line ratio series are below this range, and TW Hya and V4046 Sgr, for which the found densities lie above this range. There is no obvious separating characteristic between these objects or this group of objects and the rest of the sample. VV Sco and V4046 Sgr have similar mass accretion rates and the mass accretion rates itself do not stand out from the

whole sample. None of the objects has a spectral type significantly different from the rest of the sample. Apart from these exceptions, the electron densities deduced from the case B models seem to be consistent with the expectations of the magnetospheric accretion model.

The models predict gas temperatures of $6000 \text{ K} < T < 12000 \text{ K}$ (Martin 1996; Muzerolle et al. 2001). As shown in Section 6.1, the temperatures of the emitting gas found from the three different series of line ratios predominantly lie between 500 K and 5000 K, lower than predicted by the magnetospheric accretion model. This is true both for the whole sample and for the subsample of stars, where the dereddening is not the main source of uncertainty. Notable exceptions are TW Hya, for which $T = 7500 \text{ K}$ and $T = 30000 \text{ K}$ are found, and GQ Lup, for which $T = 7500 \text{ K}$ and $T = 10000 \text{ K}$ are found. Again, there is no obvious separating characteristic. Though both stars are of late K spectral type and have similar mass accretion rates, these characteristics do not single them out from either of the samples.

The temperature is a free parameter in the models of Muzerolle et al. (2001) and the optimal temperatures between 6000 K and 12000 K for mass accretion rates between $10^{-10} M_{\odot} \text{ yr}^{-1}$ and $10^{-6} M_{\odot} \text{ yr}^{-1}$, with lower gas temperature corresponding to higher accretion rates, are found so that the models reproduce the observed magnitudes of the hydrogen emission line fluxes. The models by Martin (1996) self-consistently describe the thermal structure of the accretion flow with adiabatic compression as the strongest heat source. For a gas temperature of $\sim 6000 \text{ K}$, the heating and cooling rates reach equilibrium and the total luminosity of the accretion flow is on the order of $10^{29} \text{ erg s}^{-1}$ to $10^{30} \text{ erg s}^{-1}$. As pointed out by Bary et al. (2008), the line luminosity of the strongest hydrogen emission features is in many objects similar to this value that therefore cannot explain the total luminosity of the accretion flow. According to them, a better estimate of the total luminosity would be reached for a gas temperature of about 10000 K, but this would need more heating than the heat sources included in the models by Martin (1996) can provide (e.g. ambipolar diffusion, adiabatic compression, photoionisation, external radiative excitation). The main source of heating in the accretion flow needs to be further investigated.

Bary et al. (2008) state that the low temperatures found in the gas of the accretion flow imply very short cooling times of only a few minutes. They arrive at their estimate of the radiative cooling time τ_{cool} of the gas in the following way. The total radiated luminosity L_{af} of the accretion flow consists mainly ($\gtrsim 75\%$) of hydrogen continuum emission and a significant contribution by emission line fluxes (Muzerolle et al. 2001). The total accretion luminosity L_{ac} is given by

$$L_{\text{ac}} = \frac{GM_* \dot{M}_{\text{ac}}}{R_*}, \quad (6.1)$$

where G is the gravitational constant, M_* and R_* are the stellar mass and radius, and \dot{M}_{ac} is the mass accretion rate. Muzerolle et al. (2001) compared in their models L_{af} to L_{ac} , assuming

$$L_{\text{af}} = f L_{\text{ac}}, \quad (6.2)$$

where f is the fraction of the accretion luminosity radiated away by the accreting gas, and found values of f between 5% and 30% for mass accretion rates between $10^{-9} M_{\odot} \text{ yr}^{-1}$ and $10^{-6} M_{\odot} \text{ yr}^{-1}$.

An approximation of the total mass of material that is in the accretion flow at a time is given by $\dot{M}_{\text{ac}} \tau_{\text{ff}}$, where τ_{ff} is the free fall time, i.e. the time the material needs to get from the inner disk truncation radius R_{t} to the stellar surface. The free fall time τ_{ff} can be estimated by $R_{\text{t}}(GM_*)^{-1/2}$ and is several hours for a typical CTTS. The total thermal energy E_{th} of the gas in the accretion flow is given by

$$E_{\text{th}} \sim \frac{3}{2} kT \frac{\dot{M}_{\text{ac}} \tau_{\text{ff}}}{\mu m_{\text{H}}}, \quad (6.3)$$

where k is the Boltzmann constant, μ is the mean molecular weight, and m_{H} is the proton mass. The cooling time τ_{cool} is given by

$$\tau_{\text{cool}} = \frac{E_{\text{th}}}{L_{\text{af}}}. \quad (6.4)$$

Rearranging this equation to give the ratio of the cooling time τ_{cool} and the free fall time τ_{ff} and assuming $\mu = 1$ results in

$$\frac{\tau_{\text{cool}}}{\tau_{\text{ff}}} \sim 0.003 \left(\frac{0.1}{f} \right) \left(\frac{T}{1000 \text{ K}} \right) \left(\frac{200 \text{ km s}^{-1}}{\sqrt{\frac{GM_*}{R_*}}} \right)^2. \quad (6.5)$$

For the temperatures in the range between 500 K and 5000 K predominantly found from the case B analysis and using the fiducial values for the other parameters, the cooling time τ_{cool} is much shorter than the free fall time τ_{ff} , on the order of a few minutes. Because Equation 6.5 only very weakly depends on the mass accretion rate \dot{M}_{ac} and the inner disk truncation radius R_t via the parameter f , this finding seems to be correct for most T Tauri stars. Even for the higher temperatures predicted by the magnetospheric accretion models the cooling time τ_{cool} is very short.

Bary et al. (2008) point out that under this conditions heating and radiative cooling are able to reach a balance and that the models of the accretion flow radiation cannot simultaneously explain the large observed luminosities and the low temperatures inferred from the case B analysis. If the results from the case B analysis are reliable, additional sources of heating to power the emission are necessary and the radiative cooling of the gas has to be more efficient to produce the observed line fluxes from a gas with lower temperature. They suggest that ionising radiation from the corona and the accretion shock could explain these conditions.

In summary, the results discussed here show that further work is required to understand the physical conditions in the emitting gas in the environment of CTTS. The assumptions of the case B models do not seem to provide a general description, because they do not statistically well describe the data for all objects. Nevertheless, the physical conditions these models favour point towards a necessity to refine the magnetically funnelled infall model to include further processes and contributions that are important for the emission line formation (see also Section 2.2). The hydrogen emission line ratios do not lose their appeal as a diagnostic to analyse the physical conditions, but more generalised models of line excitation and recombination seem to be necessary. The models by Kwan & Fischer (2011) are a major step into this direction (see also Section 7.2.2).

6.3 The reddening towards classical T Tauri stars

The spectra of 6 of the 20 objects in the sample contain more than one line from each the Paschen and the Brackett series that have a common upper level. From the observed ratios of the Paschen to the Brackett lines and the expected line ratios given by atomic physics (Equation 5.10) the extinction $E(\lambda_{Pa})/E(\lambda_{Br})$ towards each object is determined. The extinction as a function of the common upper level is used to constrain the parameters of Equation 5.20, the extinction value A_V and the exponent α of the reddening power law, describing the reddening towards the objects (see also Sections 5.3 and 5.4.2). Figure 6.17 shows the extinction from the available line ratios for each of the six objects together with two fits using Equation 5.20. In the first fit, depicted by the red line in Figure 6.17, the exponent α of the reddening power law is fixed at a value of 1.84, as in the reddening law found by Martin & Whittet (1990), and the extinction value A_V is the only free parameter. In the second fit, depicted by the blue line in Figure 6.17, both the extinction value A_V and the exponent α of the reddening power law are free parameters. The results for A_V and α obtained from the two fits as well as the reduced χ^2 values for each object are summarised in Table 6.2. The uncertainties stated are the formal 1σ uncertainties. For the first fit, where the exponent α of the reddening power law is fixed, the extinction values A_V determined for each object vary between -0.3 mag and 1.5 mag with a formal 1σ uncertainty of 0.2 mag. Within 2σ , the unphysical extinction value of $A_V = -0.3$ mag found for HO Lup is consistent with zero. The reduced χ^2 values are around 1 for half of the objects, i.e. Equation 5.20 with $\alpha = 1.84$ provides a statistically good fit to the data, while for the other half $2 < \chi_{\text{red}}^2 < 16$.

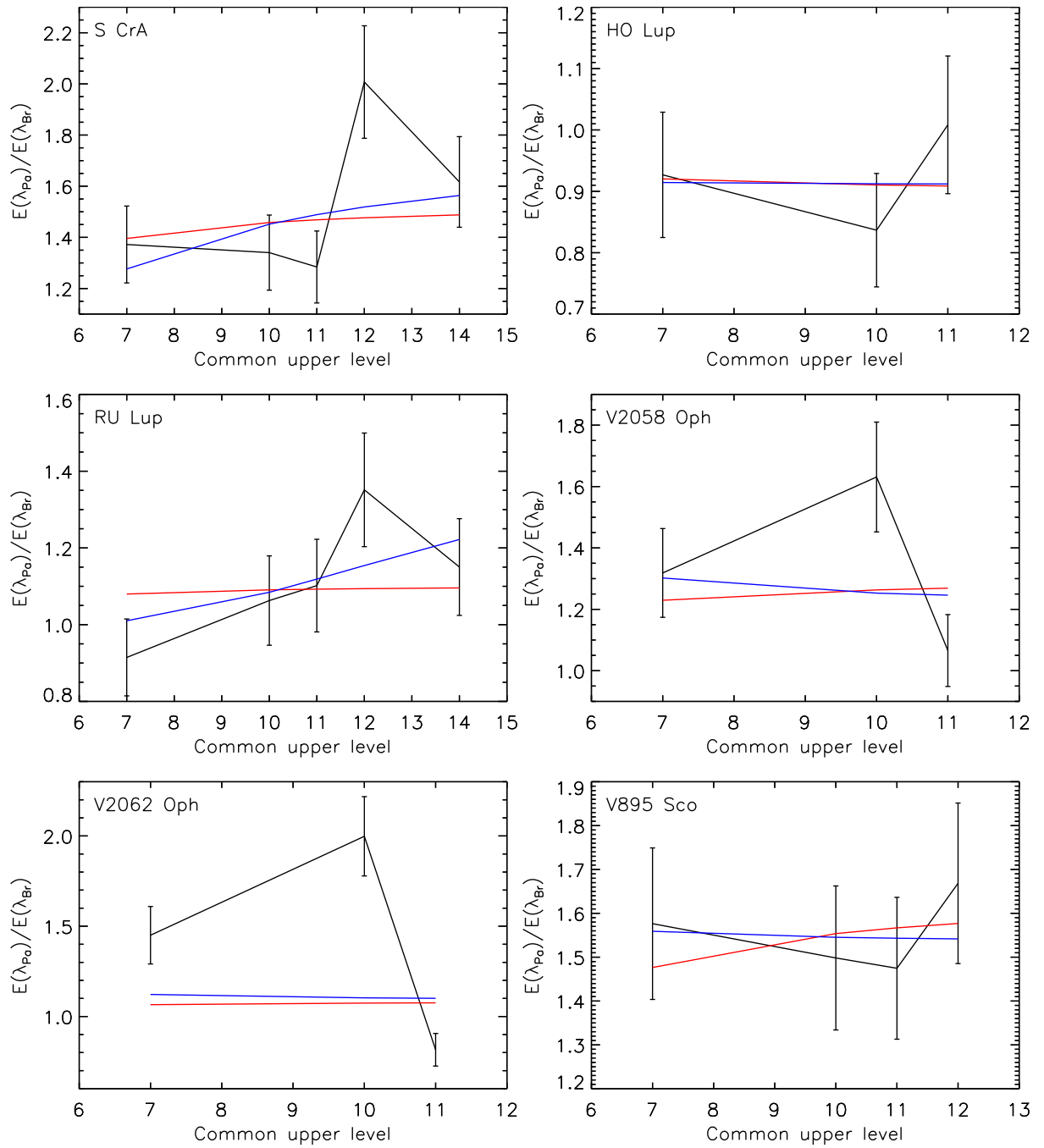


Figure 6.17: The extinction $E(\lambda_{P\alpha})/E(\lambda_{Br})$ (black) of S CrA (top left), HO Lup (top right), RU Lup (middle left), V2058 Oph (middle right), V2062 Oph (bottom left), and V895 Sco (bottom right) together with two fits using Equation 5.20. For the red fit, A_V is a free parameter, while α is fixed at 1.84. For the blue fit, both A_V and α are free parameters. The fitted values of A_V and α are summarised in Table 6.2.

Table 6.2: The results for the extinction value A_V and the exponent of the power law α from fitting Equation 5.20 to the ratios of common upper level lines.

Object (1)	No. of pairs (2)	A_V in mag (3)	χ_{red}^2 (4)	A_V in mag (5)	α (6)	χ_{red}^2 (7)
S CrA	5	1.2 ± 0.2	2.18	0.7 ± 0.4	4.1 ± 3.0	2.70
HO Lup	3	-0.3 ± 0.2	0.71	-0.4 ± 2.6	1.2 ± 9.4	1.42
RU Lup	5	0.3 ± 0.2	1.50	0.0 ± 0.1	19.2 ± 23.2	1.02
V2058 Oph	3	0.8 ± 0.2	3.81	1842 ± 10^7	0.0 ± 3.1	6.85
V2062 Oph	3	0.2 ± 0.2	15.90	$1612 \pm 8 \cdot 10^7$	0.0 ± 13.5	30.78
V895 Sco	4	1.5 ± 0.2	0.34	2.6 ± 3.9	0.9 ± 1.6	0.38

Notes. Columns 3 and 4 for fixed $\alpha = 1.84$; columns 5 to 7 for both α and A_V as free parameters.

An underestimation of the uncertainties seems unlikely as discussed in Section 6.1. Possible errors in the measurement technique, i.e. the flux measurements, are an overcompensation of the photospheric absorption or blue shifted kinematic components, e.g. by a wind, that lead to an overestimated flux. The influence of the latter possibility seems to be limited since most of the line profiles look Gaussian on the blue side (see Figure 5.2 for examples). Finally, the model, i.e. Equation 5.20 with $\alpha = 1.84$, might be inappropriate to describe the data.

To further examine this, the second fit leaves both the extinction value A_V and the exponent α of the reddening power law as free parameters. Here, the extinction values A_V determined for each object vary between -0.4 mag and 1842 mag with formal uncertainties between 0.1 mag and $8 \cdot 10^7$ mag, while the exponents α vary between 0 and 19.2 with formal uncertainties between 1.6 and 23 . Although the reduced χ^2 values stay around 1 for the objects with these values in the first fit, but are a little higher than before for 2 of the 3, it is obvious that fitting both parameters does not yield better results. The uncertainties of the data points are too large to obtain realistic and reliable results with this small number of data points. For the objects with larger χ_{red}^2 in the first fit, the χ_{red}^2 values from the second fit are larger also. Thus, adding the exponent α of the reddening power law as a second parameter to the fit did not improve the fit for these objects. Looking at the number of data points available it stands out that the two objects with the highest χ_{red}^2 only have three data points. Fitting two parameters to a data set of three point leaves not many constraints for the fit, resulting in unrealistic values with large uncertainties. Further discussions concerning the applicability of Equation 5.20 to describe the extinction data follow at the end of Section 6.4.

6.4 Discussion concerning the extinction and the reddening law

The capability of the new method to determine the extinction value A_V , presented in Section 6.3, is examined in the following way: the values found in the fit, where the exponent α of the reddening power law is fixed at 1.84 , are compared to values stated in the literature, which are summarised in Table 5.4. For three objects (S CrA, RU Lup, V895 Sco) the extinction value A_V falls within the spread of the literature values. For V2085 Oph, the value found is slightly lower than the lowest literature value, while for HO Lup and V2062 Oph the values found here are about 1 mag lower than the lowest literature value. Looking at the spread of the literature values, which is for example 3.2 mag for V2062 Oph or reaches from 0 mag to 2.3 mag for V1269 Sco, finding a lower value than previous studies seems likely and does not imply that the method leads to wrong results. Additionally, the extinction value A_V might not be a constant, but change in time. On shorter time scales, A_V may vary due to rotationally induced changes in the structure of the environment that is responsible for the extinction, e.g. inhomogeneities in the cloud or warps in the circumstellar disk. On longer time scales, the extinction may change due to less material being in the immediate environment of the star as the star formation process

Table 6.3: The extinction values A_V used in Section 6.1 and those found Section 6.3.

Object	$A_{V,\text{lit}}$	$A_{V,\text{cul}}$	Match $\text{Br}\gamma/\text{Pa}\delta$
S CrA	1.00	1.2	y
HO Lup	1.25	0.0	n
RU Lup	0.07	0.3	y
V2058 Oph	2.20	0.8	n
V2062 Oph	3.30	0.2	n
V895 Sco	1.67	1.5	y

advances.

Using ratios of common upper level hydrogen lines to determine the extinction has an advantage over other commonly used methods because it does not need a detailed knowledge about the object in question. No exact information on the spectral type of the object and its veiling is needed. The template of the photospheric absorption for the object is chosen by comparison of different available spectra without emission in the Paschen and Brackett lines, regardless of their actual spectral type. The veiling stays unconsidered in the current method. Although using hydrogen emission lines, this method is independent of the physical conditions in the emitting gas, as long as the assumption of the gas being optically thin holds (see Section 5.3). A disadvantage of this method is that it is only applicable to objects that show several lines of the Paschen and the Brackett series in emission. The emission is mainly powered by the accretion process. From the estimated mass accretion rates \dot{M}_{ac} of the sample (see Table 3.1) and the number of Paschen and Brackett lines available (see Tables C.1 and C.2 in Appendix C.1) it seems that a mass accretion rate of about $10^{-8} M_{\odot} \text{yr}^{-1}$ or more is necessary to generate a sufficient number of lines for this method. However, HO Lup has an estimated mass accretion rate of $\dot{M}_{\text{ac}} = 3.2 \cdot 10^{-9} M_{\odot} \text{yr}^{-1}$, but shows 3 Brackett lines, while a few objects (e.g. TW Hya) have estimated mass accretion rates of a few times $10^{-8} M_{\odot} \text{yr}^{-1}$, but only show $\text{Br}\gamma$.

In principle using hydrogen lines with a common upper level to determine the extinction also allows the phenomenological law of reddening at infrared wavelengths to be studied. As shown in Section 6.3, using Equation 5.20 with both the extinction value A_V and the exponent α of the power law as free parameters provides a good fit to the data for several of the sample objects. Unfortunately, the uncertainties of the data points are too high to make any conclusive statement concerning the exponent α of the power law or to identify any features in the extinction curve in the near-infrared. Nevertheless, this method offers a new possibility to help shed light on the nature of the reddening law in the wavelength range covered by the Paschen and Brackett lines. As pointed out in Section 5.3, there still is ongoing debate concerning the shape of the power law at infrared wavelengths and even whether it is a power law at all. For two of the objects in the sample neither of the fits using Equation 5.20 provides a good result. While this probably arises from a mixture of statistical effects, problems in the measurement, a limited number of data points, and high uncertainties of the data points, it might be a hint at the possibility that the reddening law is not a power law. Other data sets like the one presented in this thesis are needed to further study this possibility.

It is instructive to compare the literature extinction values $A_{V,\text{lit}}$, used for the determination of the temperature T and the electron density n_e in Section 6.1, and the extinction values $A_{V,\text{cul}}$ determined from common upper level hydrogen lines in Section 6.3. The values are summarised in Table 6.3. While the two extinction values are very similar for S CrA, RU Lup, and V895 Sco, they vary widely for the other three (HO Lup, V2058 Oph, V2062 Oph). The values found using the common upper level hydrogen lines are much lower. Interestingly, for these three objects the observed $\text{Br}\gamma/\text{Pa}\delta$ line ratio and the one predicted by the case B models do not match, while they do within the uncertainties for the other three. This is further evidence that the literature extinction values used to deredden the fluxes of these objects do not represent the conditions at the time of observation.

In summary, the results discussed above show that common upper level lines of hydrogen are a promising diagnostic for the determination of the extinction towards CTTS. The data used here allows the extinction value A_V to be determined, a quantity very important for the determination of other properties of the system, e.g. the mass accretion rate. The common upper level line diagnostic likely is also able to yield information on the shape of the extinction law in the near-infrared and possibly can even be used to identify new features in the extinction curve. A better understanding of the extinction will offer further constraints on the properties of the dust, like grain size distribution and composition, in the environment of CTTS that in turn are the starting conditions of models of planet formation.

6.5 Using the newly determined A_V values for the estimation of the temperature T and the electron density n_e

The extinction values A_V determined in Section 6.3 can now be used to repeat the analysis of the physical conditions in Section 6.1. Figures 6.18 to 6.23 show the three series of line ratios for each of the six objects together with the five case B models with the smallest reduced χ^2 values. The temperature T and the electron density n_e for each model is stated in the figure legends. Table 6.4 summarises the models that best fit the data and their reduced χ^2 values. In Appendix C.5, the reduced χ^2 values of all models plotted in the figures can be found. The corresponding table for each object is stated in the figure caption and in the last column of Table 6.4.

Comparing the results for the temperatures T and the densities n_e in Tables 6.1 and 6.4 shows that there is only marginal change for the three objects for which the change in A_V is only small (S CrA, RU Lup, V895 Sco). The reduced χ^2 values stay roughly the same and the temperature and densities only change by one model step for three of the individual ratios. Interestingly, the observed $\text{Br}\gamma/\text{Pa}\delta$ ratio of RU Lup now does not match the predicted one within the uncertainties. The reduced χ^2 increases by 0.65 for the $\text{Br}\gamma/\text{Pa}n_{\text{up}}$ line ratios, resulting in the temperature to change by one model step from 1000 K to 3000 K. For the $\text{Pa}n_{\text{up}}/\text{Pa}\beta$ line ratios the reduced χ^2 decreases by 0.77 with no change in T and n_e .

The new extinction values improve the fit for the other three objects (HO Lup, V2058 Oph, V2062 Oph) with two exceptions where the reduced χ^2 slightly increases ($\text{Pa}n_{\text{up}}/\text{Pa}\beta$ of HO Lup, $\text{Br}n_{\text{up}}/\text{Br}\gamma$ for V2062 Oph). The reduced χ^2 values are lower by up to a factor of 15. The improvement is most pronounced for the $\text{Br}\gamma/\text{Pa}n_{\text{up}}$ line ratios, where the observed and predicted ratio now match for all objects. This further strengthens the conclusion that for these objects an inadequate dereddening is a major source of uncertainty.

For HO Lup, V2058 Oph, V2062 Oph, and V895 Sco, now $\chi_{\text{red}}^2 \leq 1.15$, except for the $\text{Br}n_{\text{up}}/\text{Br}\gamma$ ratios of V2058 Oph and V2062 Oph, where there are only two data points. For S CrA and RU Lup, still $\chi_{\text{red}}^2 > 2$. While the former can be considered a statistically good fit, the latter add to the doubts voiced in Section 6.2 whether the case B models are really the appropriate models to examine the physical conditions in the emitting gas in the environment of CTTS. For V2062 Oph, the values found show a considerable spread both in temperature T , from 500 K to 20 000 K, and in density n_e , from 10^5 cm^{-3} to 10^{11} cm^{-3} . While large spreads in temperature also occur in the results in Section 6.1 for a few objects (e.g. TW Hya), this is not found for the density. With the reduced χ^2 below 1 for the $\text{Pa}n_{\text{up}}/\text{Pa}\beta$ and $\text{Br}\gamma/\text{Pa}n_{\text{up}}$ line ratios nonetheless, this might be an additional indication that the case B models are not appropriate.

Table 6.4: The temperature T and the electron density n_e of the best fitting model for each series of line ratios.

Object (1)	Figure (2)	Pan _{up} /Pa β			Br γ /Pan _{up}			Br n_{up} /Br γ			Table of other χ^2_{red} (13)	
		T in K (3)	n_e in cm ⁻³ (4)	χ^2_{red} (5)	T in K (6)	n_e in cm ⁻³ (7)	χ^2_{red} (8)	Match Br γ /Pa δ (9)	T in K (10)	n_e in cm ⁻³ (11)		χ^2_{red} (12)
S CrA	6.18	1000	10 ¹⁰	2.20	3000	10 ⁹	2.1	y	5000	10 ⁹	3.36	C.21
HO Lup	6.19	10000	10 ¹⁰	0.53	7500	10 ¹⁰	0.83	y	7500	10 ¹⁰	0.03	C.22
RU Lup	6.20	1000	10 ¹⁰	2.33	1000	10 ⁹	3.01	n	3000	10 ⁹	3.08	C.23
V2058 Oph	6.21	5000	10 ¹⁰	1.15	5000	10 ⁹	1.15	y	7500	10 ¹⁰	6.66	C.24
V2062 Oph	6.22	20000	10 ⁸	0.26	3000	10 ⁵	0.97	y	500	10 ¹¹	15.59	C.25
V895 Sco	6.23	7500	10 ¹⁰	0.67	5000	10 ¹⁰	0.47	y	7500	10 ¹⁰	0.75	C.26

Notes. Column 2: label of the figure showing the data and the models; column 9: 'y', if observed and predicted Br γ /Pa δ ratio match within the uncertainties; column 13: label of the table summarising the χ^2_{red} of all models in the corresponding figure.

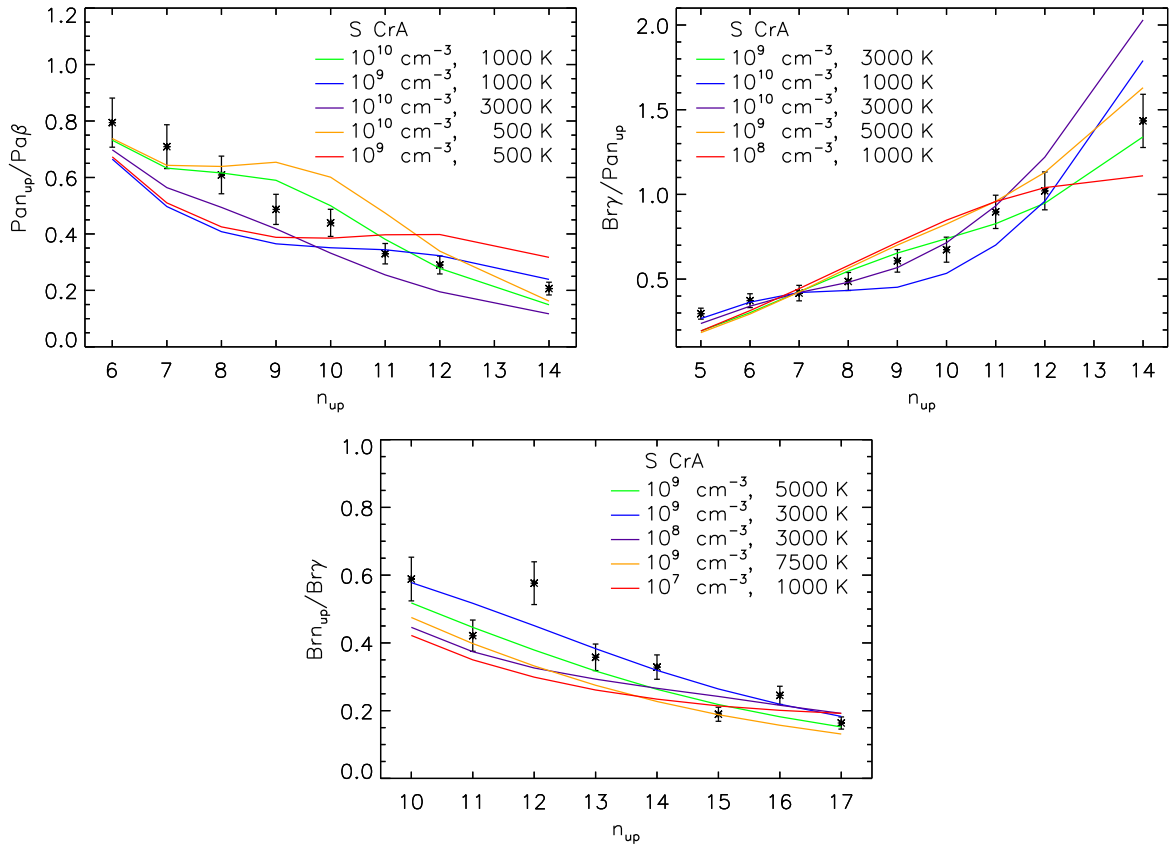


Figure 6.18: The observed line ratios of the Paschen lines using $Pa\beta$ as reference line (*top left*), the Paschen lines using $Br\gamma$ as reference line (*top right*), and the Brackett lines using $Br\gamma$ as reference line (*bottom*) of S CrA together with the five case B models with lowest χ_{red}^2 . The legend indicates the electron density n_e and temperature T for each model with χ_{red}^2 increasing from *green* to *red*. The χ_{red}^2 are summarised in Table C.21 in Appendix C.5.

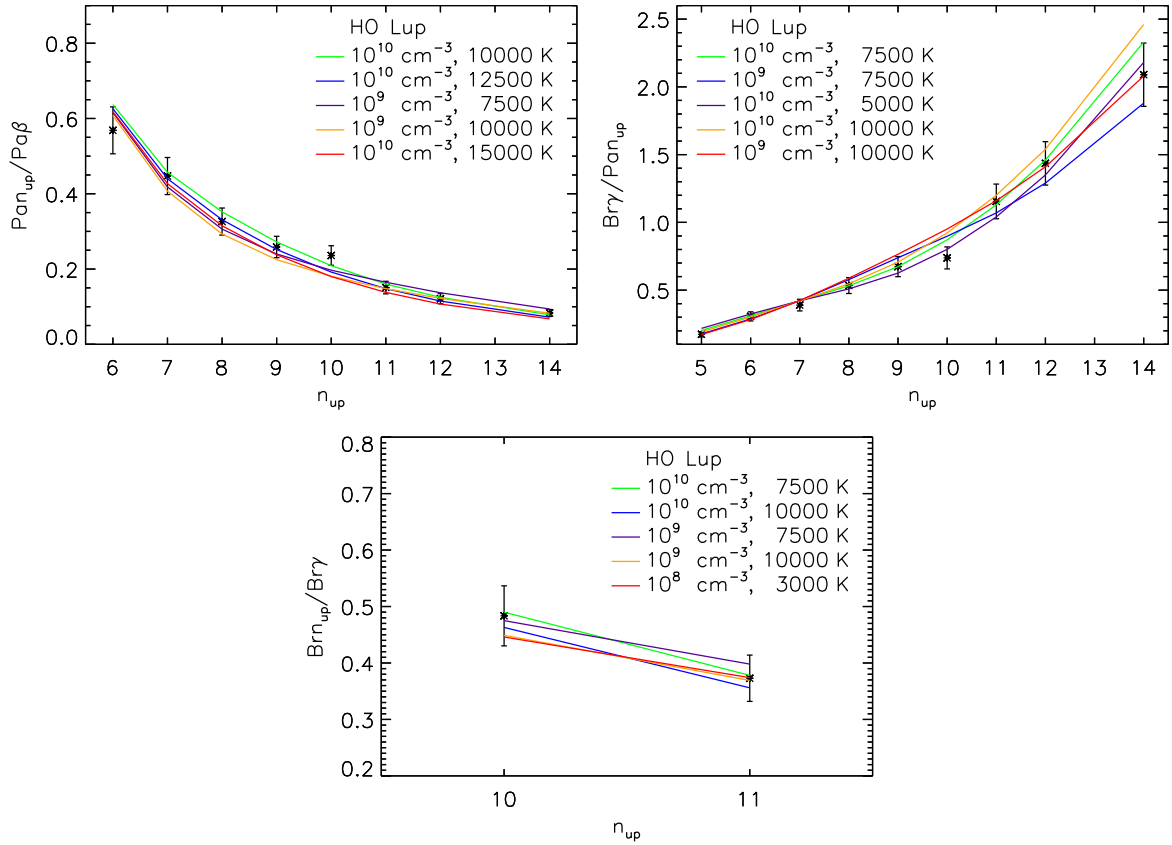


Figure 6.19: As Figure 6.18, but for HO Lup. The χ_{red}^2 are summarised in Table C.22 in Appendix C.5.

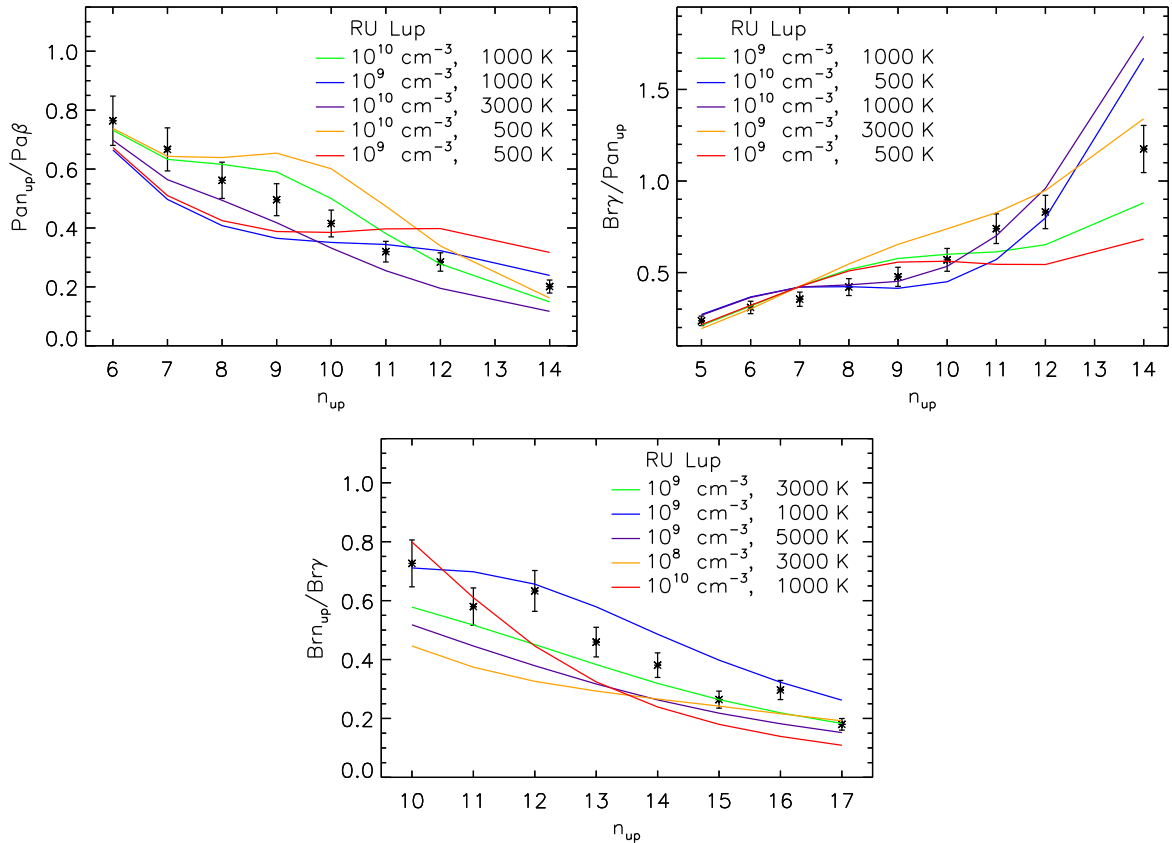


Figure 6.20: As Figure 6.18, but for RU Lup. The χ_{red}^2 are summarised in Table C.23 in Appendix C.5.

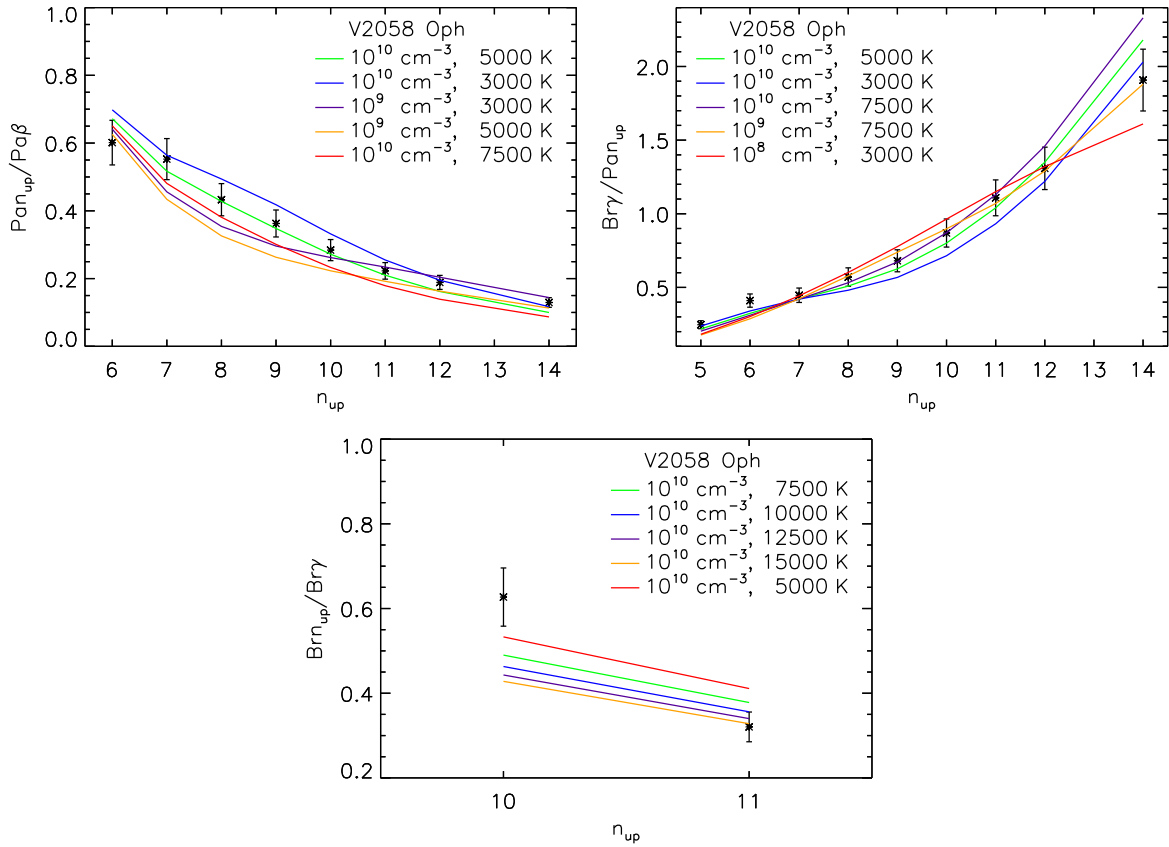


Figure 6.21: As Figure 6.18, but for V2058 Oph. The χ_{red}^2 are summarised in Table C.24 in Appendix C.5.

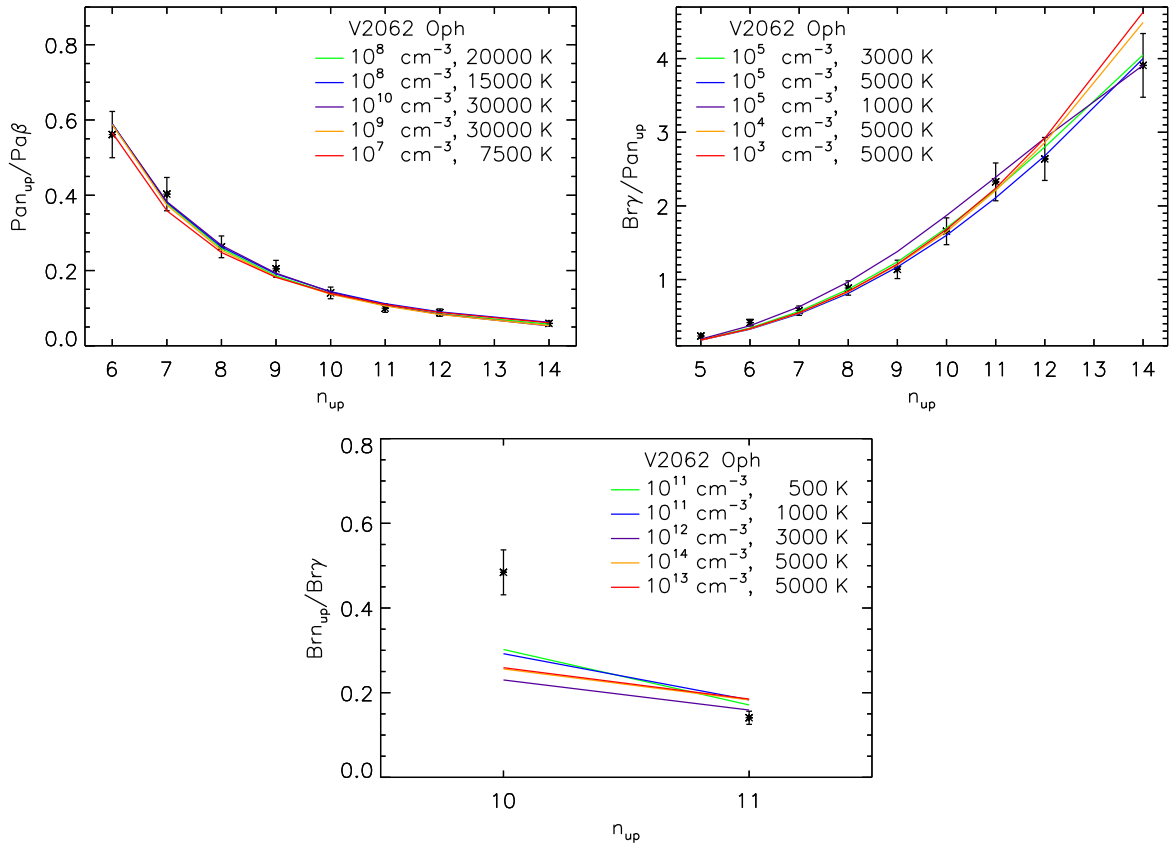


Figure 6.22: As Figure 6.18, but for V2062 Oph. The χ_{red}^2 are summarised in Table C.25 in Appendix C.5.

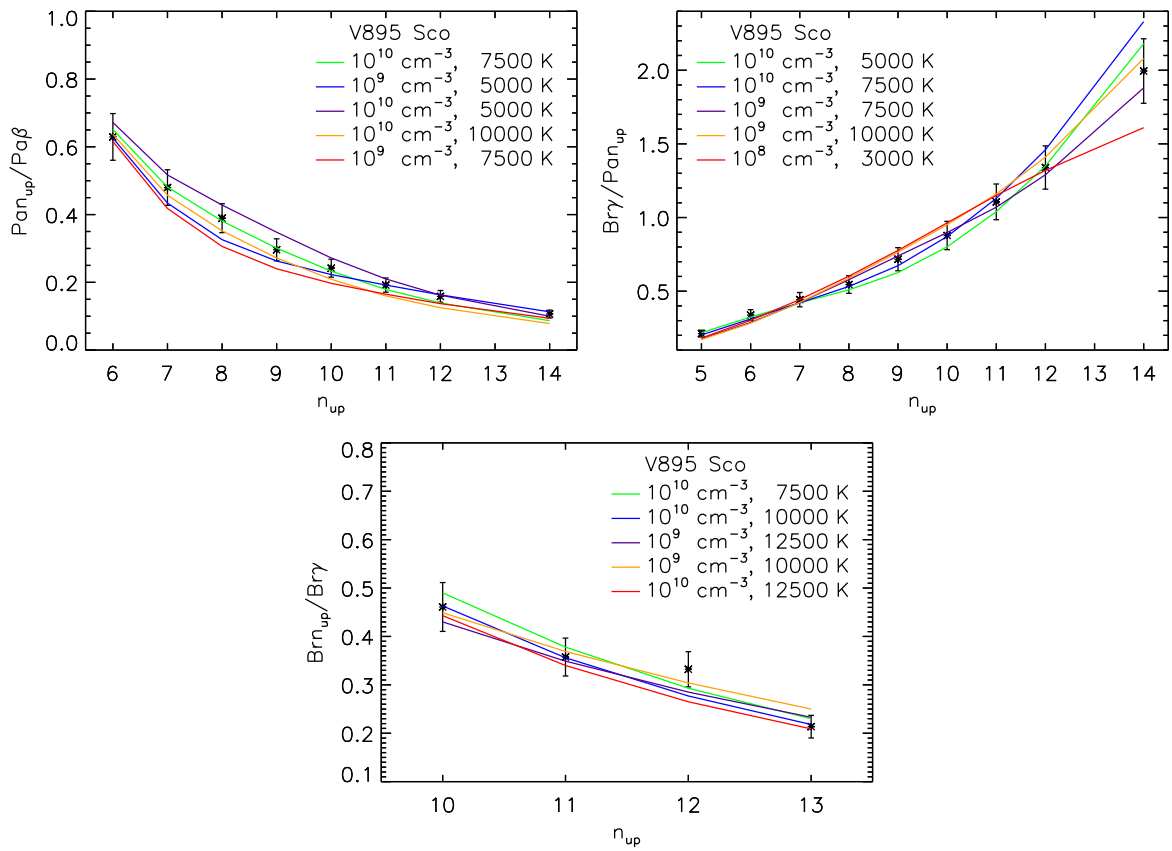


Figure 6.23: As Figure 6.18, but for V895 Sco. The χ_{red}^2 are summarised in Table C.26 in Appendix C.5.

Chapter 7

Summary and Outlook

In this chapter I summarise the results of this thesis (Section 7.1) obtained from analysing VLT/X-Shooter spectra of 20 T Tauri stars. Thereafter, I present ideas for further projects involving the existing data set as well as future prospects arising from the completed work (Section 7.2).

7.1 Summary

In this thesis the environment of T Tauri stars was investigated using hydrogen emission lines. The method used to remove the contamination by telluric lines is summarised in Section 7.1.1. The results and conclusions from the examination of the physical conditions in the emitting gas and the reddening towards the stars are summarised in Sections 7.1.2 and 7.1.3, respectively.

7.1.1 Telluric line removal

An important step for the analysis of ground-based near-infrared spectra is the proper treatment of the contamination by telluric lines. For this purpose, I extended the approach by Seifahrt et al. (2010) to model the transmission of Earth’s atmosphere and use these models to correct the effect of telluric absorption lines. The resulting software package `tellrem` can be applied to almost the complete spectral range of X-Shooter. It is in principle adaptable to any instrument and will be made available to the community. The use of telluric models is a worthwhile alternative to the observation of telluric standard stars. It also circumvents the difficulties for the analysis of the hydrogen lines of the target star caused by the use of A or B stars, that show distinctive hydrogen absorption lines themselves, as telluric standards.

7.1.2 The physical conditions in the emitting gas

Up to three series of line ratios, namely Pan_{up} to $\text{Pa}\beta$, $\text{Br}\gamma$ to Pan_{up} , and $\text{Br}n_{\text{up}}$ to $\text{Br}\gamma$, of 15 of the 20 objects in the sample were compared to case B model predictions, which depend on the temperature T and the electron density n_e in the emitting gas. The temperatures T inferred lie predominantly between 500 K and 5000 K, while the electron densities n_e predominately fall in the range of 10^9 cm^{-3} to 10^{10} cm^{-3} . The results from the case B analysis have to be treated with caution, because the models do not provide a statistically good fit to the data for many objects. While for several objects the main reason seems to be the use of inadequate extinction values A_V in the dereddening of the fluxes, the remaining subsample still raises the question whether case B really is an appropriate description of the conditions in the gas.

The values stated above, despite the doubts in their reliability, can be compared to the predictions of the magnetospheric accretion model, the currently accepted model to describe the CTTS phase of star formation. This shows that the densities found here agree with those predicted by the models, whereas the deduced temperatures lie below the predicted ones. The conditions found imply very short cooling times of the gas of only a few minutes. These findings cannot

be explained by the heating and radiative cooling processes included in the models by Martin (1996) and Muzerolle et al. (2001). Bary et al. (2008) find similar results and suggest that ionising radiation from the corona and the accretion shock could explain the conditions found. Further refinement of the magnetically funnelled infall model to include additional processes and contributions that are important for the emission line formation seems to be necessary.

7.1.3 The reddening towards classical T Tauri stars

Employing the hydrogen emission lines that have a common upper level, I applied a new method to examine the reddening towards CTTS to 6 of the 20 objects in the sample. In an optically thin gas, the ratios of these lines are independent of the physical conditions in the emitting gas and given by constants known from atomic physics. I determined new extinction values A_V for the objects. These lie within the literature range for most objects and a little lower for the remaining ones. Actual changes in the extinction value A_V are likely responsible for the deviation. This method has an advantage over other commonly used procedures because it does not require a detailed knowledge about the object under study.

While this new method in principle can be used to study the shape of the reddening law, I cannot find deviations from the standard parametrisation $A \sim A_V \lambda^{-1.84}$ (Martin & Whittet 1990) of the reddening at infrared wavelengths due to relatively high uncertainties of the data.

7.2 Outlook

The large simultaneous wavelength coverage of X-Shooter allows several questions concerning T Tauri stars to be addressed without the problems arising from their variability. The full potential of the data set I studied in my thesis still needs to be exploited. Here, I present several ideas and projects I would like to pursue in the future involving the existing data set as well as others.

7.2.1 Adaptation of tellrem for TIGRE

As described above the software package `tellrem`, which I developed for the removal of telluric lines from the VLT/X-Shooter spectra, is in principle adaptable to any instrument. The Hamburger Sternwarte is main partner in a consortium that operates the TIGRE, a 1.2 m telescope at La Luz Observatory in Mexico. This telescope is equipped with a medium resolution ($R \sim 20\,000$) echelle spectrograph covering the wavelength range from 3500 Å to 8800 Å. This region contains several telluric bands. A PhD student will adapt the software package `tellrem` to the requirements of this instrument.

7.2.2 The physical conditions in the emitting gas

As pointed out in Sections 6.2 and 7.1.2 there are growing doubts whether the case B models used in this thesis to determine the temperature and density in the emitting gas are the appropriate description of the conditions in the hydrogen line formation region of CTTS. Edwards et al. (2013) find for their sample of CTTS that the models by Kwan & Fischer (2011) provide a more consistent interpretation than case B assumptions. The models by Kwan & Fischer (2011) for the line formation use local line excitation calculations that specifically reproduce the conditions in the T Tauri winds and magnetic accretion columns. These models are more general because they include both recombination and collisional excitation for the production of photons emitted in the lines and allow for the full range of optical depth. The case B models are restricted in terms of optical depth because they assume that the population of the $n = 2$ level is small, so that collisional excitation from this level is negligible.

It would be very interesting to compare the observed hydrogen line ratios to the Kwan & Fischer (2011) models and to further examine their usability to study the conditions in the accretion

disk of CTTS. Their models additionally include He I, Ca II, O I, and Na I. Including line ratios from these elements will give more constraints. Additionally, I fitted the three series of line ratios independent of each other. However, the individual lines are not unrelated, they are all formed in the same gas and should arise from the same physical conditions. Developing a robust procedure to combine all line ratios in one fit will further constrain the results.

As remarked by Edwards et al. (2013) uncertainties in the extinction prevent them from determining reliable temperatures. The same problem is present in my study. Therefore, it is essential for this analysis to have reliable extinction values A_V . For the objects to which the new method to determine A_V presented in this thesis can be applied, these can be used. They already greatly improve the fit for the case B models. However, this does not dissipate the doubts concerning the appropriateness of the case B models. For the other objects, determining the extinction directly from the spectra using the common methods hopefully will provide more reliable results.

For a complete understanding of the hydrogen emission of CTTS the contributions from different regions with potentially different temperatures and densities to the overall emission have to be taken into account. The most important regions are the accretion funnels, the accretion shocks, the winds, and the inner disk rim. In further studies I would examine how different models, diagnostics, and tracers can be used to help solve this jigsaw puzzle.

7.2.3 Characterising the sample stars

The large wavelength coverage of X-Shooter offers the possibility to determine several characteristics of the sample objects. Apart from the above-mentioned extinction value A_V , the mass accretion rate and wind properties are of great interest for CTTS. There are quite a number of methods to determine mass accretion rates and wind properties. Some of the tracers used for these purposes are scattered over the covered wavelength range. Examples are the hydrogen Balmer and Paschen continuum from the accretion hot spots that can be converted to mass accretion rates with the help of the models by Calvet & Gullbring (1998), the He I 10830 Å line (Fischer et al. 2008), and the Ca II infrared triplet (Muzerolle et al. 1998b). It will be interesting to compare the results from different methods using simultaneously acquired data, as is possible with the data set used in this thesis. This provides an excellent benchmark for correlations between the different tracers among themselves as well as between the mass accretion rate and the hydrogen emission. This will allow existing relations to be checked and possibly re-calibrated. The accretion hot spots on the stellar surface create a continuum of about 20 000 K veiling the photospheric lines. The veiling is another tracer of the mass accretion rate. The determination of the veiling provides also the spectral type, a stellar parameter that is not well determined for many of the sample objects. Knowing the spectral type of an object also will improve my new method to determine the extinction because the photospheric contribution to the line flux can be treated more reliably, though this does not seem to be the driving source of uncertainty for this method.

7.2.4 The reddening towards classical T Tauri stars

In a first step for continuing my studies of reddening it would be interesting to compare the extinction values A_V I determined with my new method to values resulting from other common methods applied to the same data set. Additionally, there are several existing studies of extinction and dust in the infrared, e.g. Spitzer's c2d survey and WISE data, providing information about the composition of the dust and its distribution (e.g. Kessler-Silacci et al. 2006; Chapman et al. 2009; Furlan et al. 2009), or the COMPLETE survey of star-forming regions, providing extinction and dust-emission maps (e.g. Ridge et al. 2006). These studies offer the possibility to compare the extinction values measured for the sample objects and/or their surrounding environment in different wavelength regions and with different methods, though non-simultaneous. This could be extended to other wavelengths, e.g. to the UV by using Hubble data. Moreover,

the sample itself could be increased with archival data as well as new data.

My new method to study the reddening also allows the phenomenological law of reddening to be tested. The quality of my existing data does not permit this. Higher quality data taken by X-Shooter or another instrument could be used to shed light on the shape of the reddening law. As discussed in Section 5.3 there is still no consensus on the exponent α of the reddening power law at infrared wavelengths and even some doubts whether it is a power law at all. For future observations it will be most important to lower the uncertainties of the flux calibration. This can be done by observing a suitable flux standard star also with the same slit width as the target stars, as is usually done but was not for the observations used here. It might be useful to re-observe a flux standard for each target star to accurately trace also the effects different airmasses have on the observations. The most promising candidates for further observations from the sample of this thesis are S CrA and RU Lup which show the largest number of common upper level lines.

New data also would allow connections to be studied between dust properties in the mid and far infrared, e.g. the silicate features at 10 and 18 μm , and the power law exponent α . This way one could examine whether near-infrared data can add new information on properties like the grain size distribution or the composition of dust in the disks of CTTS. New constraints on these properties would certainly be of interest for models of the dust and the disks.

Appendix A

Documentation for tellrem Routines

A.1 CREATE_STANDARD_PARINFO

Name:

CREATE_STANDARD_PARINFO

Purpose:

This function creates a parameter info structure for use with FITTELL containing appropriate values.

Calling Sequence:

Result = CREATE_STANDARD_PARINFO()

Inputs:

None.

Outputs:

This function returns a parameter info structure for use with FITTELL and in the format expected by MPFIT.

Example:

```
parinfo = CREATE_STANDARD_PARINFO()
```

Modification History:

Written by: Natascha Rudolf, October 2013.

A.2 EXCLUSION

Name:

EXCLUSION

Purpose:

This function extracts from a wavelength array a certain range but without the regions specified to exclude.

Calling Sequence:

Result = EXCLUSION(Wavelength, Range, Exclude)

Inputs:

Wavelength: Wavelength array from a range of which one wants to exclude certain regions.
 Range: Wavelength range to extract from above array as two-element array in the form [start,end].
 Exclude: Regions to exclude from wavelength array in the range specified as array with up to 10 entries of the form [start1,end1,...,start5,end5].

Outputs:

This function returns an index array for the wavelength array that contains the specified range but does not contain the regions stated in exclude.

Example:

indices = EXCLUSION(Wavelength, [6500.,6800.], [6558.,6568.])

Modification History:

Written by: Natascha Rudolf, October 2013.

A.3 FITTELL**Name:**

FITTELL

Purpose:

This procedure uses LBLRTM to fit a transmission model to the observed spectrum and then uses this model to remove the telluric lines from the spectrum.

Calling Sequence:

FITTELL, Wave, Data, Error, Range, Gdasdata, Obsaltitude, Params, Paramerror, Wavere-
 sult, Result, Cleaned, Cleanederror

Inputs:

Wave: Wavelength array of observed spectrum.
 Data: Flux array of observed spectrum.
 Error: Error of flux measurements.
 Range: Wavelength range of fit as two-element array in the form [start,end].
 Gdasdata: Scalar string containing absolute path to GDAS file.
 Obsaltitude: Altitude angle of observation in deg.

Keyword Parameters:

EXCLUDE:	Regions to exclude from wavelength array in the range specified as array with up to 10 entries of the form [start1,end1,...,start5,end5].
PLOT:	Set this keyword to get a plot of the result.
SILENT:	Set this keyword to suppress informational messages.
PARINFO:	Parameter info structure to use in MPFIT. Default is a standard structure created by CREATE_STANDARD_PARINFO.
TITLEPLOT:	Title of plot.

Outputs:

Params:	Fitted parameters ([smoothing_FWHM, velocity_shift, slope_of_straight, intercept_of_straight, water_abundance, methane_abundance, carbondioxide_abundance, oxygen_abundance]).
Paramserror:	Formal 1σ errors of parameters.
Waveresult:	Wavelength array of the fitted part.
Result:	Model fitted with all parameters (to be compared to observation).
Cleaned:	Telluric line removed spectrum.
Cleanederror:	Error of flux measurements divided by transmission model.

Example:

FITTELL, Wave, Data, Error, [9000.,9300.], '/here/lies/the/Gdasdata', 87.2, Params, Paramserror, Waveresult, Result, Cleaned, Cleanederror

Modification History:

Written by: Natascha Rudolf, October 2013.

A.4 GAUSSCONV**Name:**

GAUSSCONV

Purpose:

This function smooths an array by convolving with a Gaussian profile.

Calling Sequence:

smoothed_y = GAUSSCONV(X, Y, Fwhm)

Inputs:

X:	Array (double or float) of the values of the x-axis in ascending order.
Y:	Array (double or float) of same size as x of the y-axis values.
Fwhm:	FWHM in units of the x-axis of the Gaussian profile.

Outputs:

Array (double or float) of same size as x containing smoothed y.

Example:

```
flux_smoothed = (wavelength,flux,0.75)
```

Modification History:

Written by: Natascha Rudolf, October 2013.

A.5 GETABUNDANCES**Name:**

GETABUNDANCES

Purpose:

This procedure determines the abundances of the main molecules (H₂O, CO₂, CH₄, O₂) producing telluric lines in the X-Shooter spectral range.

Calling Sequence:

GETABUNDANCES, Wavevis, Specvis, Errvis, Wavenir, Specnir, Errnir, Gdasdata, Obsaltitude, Ab_h2o, Ab_co2, Ab_ch4, Ab_o2

Inputs:

Wavevis:	Wavelength array of VIS data.
Specvis:	Flux array of VIS data.
Errvis:	Error array of VIS data.
Wavenir:	Wavelength array of NIR data.
Specnir:	Flux array of NIR data.
Errnir:	Error array of NIR data.
Gdasdata:	Scalar string containing absolute path to GDAS file.
Obsaltitude:	Altitude angle of observation in deg.

Keyword Parameters:

SILENT:	Set this keyword to suppress informational messages.
PLOT:	Set this keyword to get a plot of the result.

Outputs:

Ab_h2o:	Abundance of H ₂ O in this observation.
Ab_co2:	Abundance of CO ₂ in this observation.
Ab_ch4:	Abundance of CH ₄ in this observation.
Ab_o2:	Abundance of O ₂ in this observation.

Example:

GETABUNDANCES, Wavevis, Specvis, Errvis, Wavenir, Specnir, Errnir, '/here/lies/the/Gdas-data', 87.2, Ab_h2o, Ab_co2, Ab_ch4, Ab_o2

Modification History:

Written by: Natascha Rudolf, October 2013.

A.6 GETOBJECTS

Name:

GETOBJECTS

Purpose:

This function extracts the names of the objects to use the `tellrem` package on.

Calling Sequence:

```
Result = GETOBJECTS()
```

Inputs:

None.

Outputs:

This function returns a string array of the folder names located in the path containing the reduced spectra specified in the info file provide to `LOADTELLREMINFO`. It expects these to be the object names which will be added as auxiliary information during the further run of `TELLREM`.

Common Blocks:

`TELLREM_INFO`: This common block contains relevant folder names and strings for running `TELLREM`. It has to be initialised by running `LOADTELLREMINFO`.

Example:

```
objects = GETOBJECTS()
```

Modification History:

Written by: Natascha Rudolf, October 2013.

A.7 IDLPLOTTITLECHANGER

Name:

IDLPLOTTITLECHANGER

Purpose:

This procedure replaces the IDL standard plot title "Graphics produced by IDL" with the file name in the specified postscript file.

Calling Sequence:

```
IDLPLOTTITLECHANGER, Filename
```

Inputs:

Filename: Name of the postscript file to work on (scalar string).

Outputs:

None.

Example:

IDLPLOTTITLECHANGER,'plotfileXYZ.ps'

Modification History:

Written by: Natascha Rudolf, October 2013.

A.8 LOADTELLREMINFO

Name:

LOADTELLREMINFO

Purpose:

This procedure loads the information necessary to run the procedures of the `tellrem` package and creates the common block `TELLREM.INFO`. An example file called `'info_for_tellrem'`, which you can adjust for your needs, is provided with the package. Run this procedure before any of the other functions or procedure of the `tellrem` package.

Calling Sequence:

LOADTELLREMINFO, filename

Inputs:

Filename: Absolute path to file containing the information as string.

Outputs:

None. But creates the common block `TELLREM.INFO`. This common block contains the variables `Gdasfolder`, `Modelatmosphere`, `Executeablename`, `Spectrafolder`, and `Obstype`. All of them are scalar strings. `Gdasfolder` contains the absolute path of the folder containing the GDAS files, `Modelatmosphere` contains the absolute path to the MIPAS model atmosphere, `Executeablename` contains the name of LBLRTM executable, `Spectrafolder` contains the absolute path to the folder containing the reduced spectra (in individual subfolders therein), and `Obstype` contains the prefix specifying the type of observation (i.e. `SCI`, `FLUX`, or `TELL`), which the X-Shooter pipeline assigns to the `.fits` files.

Common Blocks:

`TELLREM.INFO`: This common block contains relevant folder names and strings for running `tellrem`. It is created by this procedure.

Example:

LOADTELLREMINFO,'/here/lies/info_for_tellrem'

Modification History:

Written by: Natascha Rudolf, October 2013.

A.9 RDDAT

Name:

RDDAT

Purpose:

This procedure reads VLT/X-Shooter spectra.

Calling Sequence:

RDDAT,File,Wave,Spec,Error,Header

Inputs:

File: Scalar string containing complete path to file.

Keyword Parameters:

PHOENIX: Set this keyword if you want to read spectra from the Göttingen Spectral Library by PHOENIX (<http://phoenix.astro.physik.uni-goettingen.de/>).

Outputs:

Wave: Wavelength array in Å.
Spec: Flux array.

Optional Outputs:

Error: Error array.
Header: Header of the fits file.

Example:

If you just want to have wavelength and flux use
rddat, '/here/is/the/data/SCI_SLIT_MERGE1D_VIS.fits', wave, spec

If you also want error and header use
rddat, '/here/is/the/data/SCI_SLIT_MERGE1D_VIS.fits', wave, spec, error, header

Modification History:

Written by: Natascha Rudolf, October 2013.

A.10 READMODATM

Name:

READMODATM

Purpose:

This procedure reads the requested parameter (e.g. pressure, abundance) from the MIPAS model atmosphere.

Calling Sequence:

Result = READMODATM(Parameter)

Inputs:

Parameter: Parameter to be read (scalar string) in format of MIPAS model atmosphere file.

Outputs:

This function returns the requested parameter in a float array.

Common Blocks:

TELLREM.INFO: This common block contains relevant folder names and strings for running TELLREM. It has to be initialised by running LOADTELLREMINFO.

Restrictions:

This function only works for the parameters available in the MIPAS model atmosphere. These are: HGT, PRE, TEM, N2, O2, CO2, O3, H2O, CH4, N2O, HNO3, CO, NO2, N2O5, ClO, HOCl, ClONO2, NO, HNO4, HCN, NH3, F11, F12, F14, F22, CCl4, COF2, H2O2, C2H2, C2H6, OCS, SO2, SF6.

Example:

height = READMODATM('HGT')

Modification History:

Written by: Natascha Rudolf, October 2013.

A.11 RECRFITTELLRES

Name:

RECRFITTELLRES

Purpose:

This procedure recreates the output of FITTELL for the parameters specified.

Calling Sequence:

RECRFITTELLRES, Wave, Data, Error, Range, Gdasdata, Obsaltitude, Params, Waveresult, Result, Cleaned, Cleanederror

Inputs:

Wave:	Wavelength array of observed spectrum.
Data:	Flux array of observed spectrum.
Error:	Error of flux measurements.
Range:	Wavelength range of fit as two-element array in the form [start,end].
Gdasdata:	Scalar string containing absolute path to GDAS file.
Obsaltitude:	Altitude angle of observation in deg.
Params:	Fitted parameters ([smoothing_FWHM, velocity_shift, slope_of_straight, intercept_of_straight, water_abundance, methane_abundance, carbondioxide_abundance, oxygen_abundance]).

Keyword Parameters:

SILENT:	Set this keyword to suppress informational messages.
---------	--

Outputs:

Waveresult:	Wavelength array of the fitted part.
Result:	Model fitted with all parameters (to be compared to observation).
Cleaned:	Telluric line removed spectrum.
Cleanederror:	Error of flux measurements divided by transmission model.

Example:

RECRFITTELLRES, Wave, Data, Error, [9000.,9300.], '/here/lies/the/Gdasdata', 87.2, Params, Waveresult, Result, Cleaned, Cleanederror

Modification History:

Written by:	Natascha Rudolf, October 2013.
-------------	--------------------------------

A.12 RUNLBLRTM**Name:**

RUNLBLRTM

Purpose:

This procedure creates a TAPE5 using the GDAS data and the MIPAS model atmosphere and runs LBLRTM to obtain a transmission spectrum in the specified wavelength range.

Calling Sequence:

RUNLBLRTM, Wavestart, Waveend, Gdasdata, Obsaltitude, Wavetransmission, Transmission

Inputs:

Wavestart:	Start wavelength in Å (scalar float or double).
Waveend:	End wavelength in Å (scalar float or double).
Gdasdata:	Scalar string containing absolute path to GDAS file.
Obsaltitude:	Altitude angle of observation in deg (scalar float or double).

Keyword Parameters:

OBSELEVATION:	Elevation above sea level in km of observatory site, default is 2.648 for VLT at Paranal.
WATER:	Water abundance (scalar float or double) relative to model abundance.
METHANE:	Methane abundance (scalar float or double) relative to model abundance.
OXYGEN:	Oxygen abundance (scalar float or double) relative to model abundance.
CARBONDIOXIDE:	Carbondioxide abundance (scalar float or double) relative to model abundance.
AMMONIA:	Ammonia abundance (scalar float or double) relative to model abundance.
NITRICOXIDE:	Nitricoxide abundance (scalar float or double) relative to model abundance.
OZONE:	Ozone abundance (scalar float or double) relative to model abundance.
SILENT:	Set this keyword to suppress informational messages by LBLRTM.
KEEP:	Set this keyword to keep the produced TAPE files.

Outputs:

Wavetransmission:	Wavelength in vacuum (double array)
Transmission:	Calculated transmission spectrum (double array)

Common Blocks:

TELLREM.INFO:	This common block contains relevant folder names and strings for running TELLREM. It has to be initialised by running LOADTELLREMINFO.
---------------	--

Restrictions:

LBLRTM can only calculate a piece of less then 2020 cm^{-1} in width.

Example:

A simple call looks like this:

```
RUNLBLRTM, 6000., 6500., '/here/is/the/GDAS/file', 79.8, wt, t
```

If you want to adjust the abundance of water and suppress informational messages, use this:

```
RUNLBLRTM, 6000., 6500., '/here/is/the/GDAS/file', 79.8, wt, t, water=0.8, /silent
```

wt contains the wavelength array and t the transmission spectrum.

The abundance keywords work relative to the model abundance, i.e. setting water=1. means using the water abundance from the atmospheric model, setting water=0.8 means lowering the abundance from the atmospheric model by 20 %.

Modification History:

Written by: Natascha Rudolf, October 2013.

A.13 STATUSINTERPRETER**Name:**

STATUSINTERPRETER

Purpose:

This function maps the status code of MPFITFUN to a text explaining its meaning.

Calling Sequence:

```
text = STATUSINTERPRETER(Status)
```

Inputs:

Status: The integer status code returned by MPFITFUN.

Outputs:

This function returns a string explaining the meaning of the status code MPFITFUN set.

Example:

```
textmeaning = STATUSINTERPRETER(1)
```

Modification History:

Written by: Natascha Rudolf, October 2013.

A.14 SUBZERO

Name:

SUBZERO

Purpose:

This function replaces zero or subzero elements of the input array by the mean of the neighbouring points.

Calling Sequence:

```
Result = SUBZERO(Inputarray)
```

Inputs:

Inputarray: Array to be treated.

Outputs:

This function returns the array containing no zero or subzero elements.

Example:

```
outputarray = subzero(inputarray)
```

Modification History:

Written by: Natascha Rudolf, October 2013.

A.15 TELL

Name:

TELL

Purpose:

This function calculates a model transmission spectrum with the abundances stated and adjusts it by convolving with a Gaussian, shifting in wavelength and multiplying by a straight line so that it can be compared to an observed spectrum.

Calling Sequence:

```
model = TELL(Wavelength,Parameters,Gdasdata=Gdasdata,Obsaltitude=Obsaltitude)
```

Inputs:

Wavelength: Wavelength array in Å for which model is requested.
 Parameters: Array of parameters of model ([smoothing_FWHM, velocity_shift, slope_of_straight, intercept_of_straight, water_abundance, methane_abundance, carbondioxide_abundance, oxygen_abundance]).

Required Keyword Parameters:

GDASDATA: Scalar string containing absolute path to GDAS file.
 OBSALTITUDE: Altitude angle of observation in deg.

Keyword Parameters:

SILENT: Set to 1 if you do not want to get informational messages.

Outputs:

This function returns an array of the same size as wavelength containing the transmission spectrum modelled and adjusted according to the parameters.

Common Blocks:

MERKEN: This common block saves the parameters and results to avoid having to run LBLRTM too often.

Example:

```
mod = TELL(wave_array, [0.5,0.1,-5.8,2.,1.0,1.0,1.0,1.0], gdasdata='/here/lies/the/Gdasdata',  
obsaltitude=82.2)
```

Modification History:

Written by: Natascha Rudolf, October 2013.

A.16 TELLREM

Name:

TELLREM

Purpose:

This procedure creates telluric line removed spectra using the information specified by the info file.

Calling Sequence:

TELLREM,Infofile,Telluricremovedspectra

Inputs:

Infofile: Absolute path to file containing the necessary information to run the procedures of the `tellrem` package. An example file called `'info_for_tellrem'`, which you can adjust for your needs, is provided with the package. The format must be adhered to.

Keyword Parameters:

NOSAVE: Set this keyword if you do not want the results to be saved to an IDL .sav file.
NO PLOT: Set this keyword if you do not want plots of the results to be created.

Outputs:

This procedure returns an array of structures `'Telluricremovedspectra'` containing the telluric line removed spectra and additional information for each object. For each object the structure consists of the tags `'object'` containing the object name in a string, `'obsdate'` containing the JD observation date as double scalar, `'obsaltitude'` containing the altitude angle of the observation as double scalar, `'exptimeu'` containing the exposure time in the UVB arm as double scalar, `'exptimev'` containing the exposure time in the VIS arm as double scalar, `'exptimen'` containing the exposure time in the NIR arm as double scalar, `'wclv'` containing the wavelength array for the UVB data, `'clu'` containing the flux array of UVB, `'eclu'` containing the error array of the UVB flux, `'wclv'` containing the wavelength array for the VIS data, `'clv'` containing the flux array of VIS, `'eclv'` containing the error array of the VIS flux, `'wcln1'` containing the wavelength array for the NIR data in region 1, `'cln1'` containing the flux array of NIR in region 1, `'ecln1'` containing the error array of the NIR flux in region 1, `'wcln2'` containing the wavelength array for the NIR data in region 2, `'cln2'` containing the flux array of NIR in region 2, `'ecln2'` containing the error array of the NIR flux in region 2, `'wcln3'` containing the wavelength array for the NIR data in region 3, `'cln3'` containing the flux array of NIR in region 3, `'ecln3'` containing the error array of the NIR flux in region 3. The NIR arm spectrum is divided into 3 parts omitting the heavily absorbed parts.

Example:

TELLREM,'/here/lies/info_for_tellrem',Telluricremovedspectra

Modification History:

Written by: Natascha Rudolf, October 2013.

A.17 TELLREMPARAMETERS

Name:

TELLREMPARAMETERS

Purpose:

This function determines the parameters needed to create a telluric line model for the individual observations.

Calling Sequence:

Result = TELLREMPARAMETERS(Objects)

Inputs:

Objects: String array containing the object names that are to be treated, i.e. the names of the folders that contain the data of the individual objects.

Keyword Parameters:

PLOTNAME: String containing the name of the file holding the plots. It is named plotnameobjectname.ps. Default is 'tellrem'.
 NOPLOT: Set this keyword if you do not want the fit results to be plotted.
 NOSAVE: Set this keyword if you do not want the parameters to be saved into an IDL .sav file.
 SAVNAME: String containing the name of the .sav file. It will be called sav-name.sav, default is 'tellremparams'.
 SILENT: Set this keyword if you do not want informational message about the progress to be printed to the terminal.

Outputs:

This function returns an array of structures containing the parameters fitted to the spectrum and additional information for each object. For each object, the structure consists of the tags 'object' containing the object name in a string, 'obsdate' containing the JD observation date as double scalar, 'obsaltitude' containing the altitude angle of the observation as double scalar, 'exptimev' containing the exposure time in the VIS arm as double scalar, 'exptimen' containing the exposure time in the NIR arm as double scalar and a 55-element array of structures called 'para'. The individual structures consist of the tags 'range' containing the start and end of the region for which the parameters stored in 'p', an 8-element double array, were determined. 'pe', an 8-element double array, contains the errors of the parameters. The parameters are [smoothing_FWHM, velocity_shift, slope_of_straight, intercept_of_straight, water_abundance, methane_abundance, carbondioxide_abundance, oxygen_abundance] used in TELL.

Common Blocks:

TELLREM.INFO: This common block contains relevant folder names and strings for running TELLREM. It has to be initialised by running LOADTELLREMINFO.

Example:

```
params=TELLREMPARAMETERS(['Object1','Object2','Object3'])
```

Modification History:

Written by: Natascha Rudolf, October 2013.

A.18 TELLREMSPECTRA

Name:

TELLREMSPECTRA

Purpose:

This function takes the parameters determined by TELLREMPARAMETERS and uses the modelled telluric line spectrum to remove the telluric lines from the observed spectrum.

Calling Sequence:

```
Result = TELLREMSPECTRA(Tellremparameters)
```

Inputs:

Tellremparameters: The array of structures returned by TELLREMPARAMETERS.

Keyword Parameters:

SILENT: Set this keyword if you do not want informational message about the progress printed to the terminal.

SAVNAME: String containing the name of the .sav file. It will be called savname.sav, default is 'spectra_tellrem'.

NOSAVE: Set this keyword if you do not want the resulting spectra to be saved to an IDL .sav file.

Outputs:

This function returns an array of structures containing the telluric line removed spectra and additional information for each object. For each object, the structure consists of the tags 'object' containing the object name in a string, 'obsdate' containing the JD observation date as double scalar, 'obsaltitude' containing the altitude angle of the observation as double scalar, 'exptimeu' containing the exposure time in the UVB arm as double scalar, 'exptimev' containing the exposure time in the VIS arm as double scalar, 'exptimen' containing the exposure time in the NIR arm as double scalar, 'wclu' containing the wavelength array for the UVB data, 'clu' containing the flux array of UVB, 'eclu' containing the error array of the UVB flux, 'wclv' containing the wavelength array for the VIS data, 'clv' containing the flux array of VIS, 'eclv' containing the error array of the VIS flux, 'wcln1' containing the wavelength array for the NIR data in region 1, 'cln1' containing the flux array of NIR in region 1, 'ecln1' containing the error array of the NIR flux in region 1, 'wcln2' containing the wavelength array for the NIR data in region 2, 'cln2' containing the flux array of NIR in region 2, 'ecln2' containing the error array of the NIR flux in region 2, 'wcln3' containing the wavelength array for the NIR data in region 3, 'cln3' containing the flux array of NIR in region 3, 'ecln3' containing the error array of the NIR flux in region 3. The NIR arm spectrum is divided into 3 parts omitting the heavily absorbed parts.

Common Blocks:

TELLREM_INFO: This common block contains relevant folder names and strings for running TELLREM. It has to be initialised by running LOADTELLREMINFO.

Example:

```
tellremspecs = TELLREMSPECTRA(Tellremparams)
```

Modification History:

Written by: Natascha Rudolf, October 2013.

A.19 TELLREM_TEST_RUN**Name:**

TELLREM_TEST_RUN

Purpose:

This procedure performs a test run of the `tellrem` package using exemplary data provided in the package to check whether the installation of the related software was successful.

Calling Sequence:

TELLREM_TEST_RUN, Packagefolder, Executablename, Mipasmodel

Inputs:

Packagefolder: String containing the path to where the `tellrem` package folder is located.
Executablename: String containing the name of LBLRTM executable.
Mipasmodel: String containing the absolute path to the MIPAS model atmosphere.

Outputs:

None. But creates plot file `Tellrem_test_run_comparison.ps` comparing the freshly determined telluric line removed spectrum to the spectrum provided in the package.

Example:

```
TELLREM_TEST_RUN, '/the/tellrem/package/is/here/', 'lblrtm_executable',  
'/MIPAS/model/is/here/equ.atm'
```

Modification History:

Written by: Natascha Rudolf, December 2013.

A.20 TELLWITHOUT**Name:**

TELLWITHOUT

Purpose:

This function calculates a model transmission spectrum with the abundances stated and adjusts it by convolving with a Gaussian and shifting in wavelength to enable its use to remove telluric lines from an observed spectrum.

Calling Sequence:

```
model = TELLWITHOUT(Wavelength, Parameters, GDASDATA=gdasdata, OBSALTITUDE
= obsaltitude)
```

Inputs:

Wavelength: Wavelength array in Å for which model is requested.
Parameters: Array of parameters of model ([smoothing_FWHM, velocity_shift, slope_of_straight, intercept_of_straight, water_abundance, methane_abundance, carbondioxide_abundance, oxygen_abundance]).

Required Keyword Parameters:

GDASDATA: Scalar string containing absolute path to GDAS file.
OBSALTITUDE: Altitude angle of observation in deg.

Keyword Parameters:

SILENT: Set to 1 if you do not want to get informational messages.
WORIG: Wavelength array of unconvolved model.
TORIG: Unconvolved model.

Outputs:

This function returns an array of the same size as wavelength containing the transmission spectrum modelled and adjusted according to the parameters but without using the straight line that TELL used to fit the model to the data.

Example:

```
mod = TELLWITHOUT(wave_array, [0.5,0.1,-5.8,2.,1.0,1.0,1.0,1.0], gdasdata='/here/lies/the/Gdasdata', obsaltitude=82.2)
```

Modification History:

Written by: Natascha Rudolf, October 2013.

A.21 UVEXTINCTION**Name:**

UVEXTINCTION

Purpose:

This function calculates the UV extinction using an LBLRTM model for the stated parameters.

Calling Sequence:

```
Result = UVEXTINCTION(Tellremparameters,Wave,Gdasdata)
```

Inputs:

Tellremparameters: Structure for the individual object from the array of structures created by TELLREMPARAMETERS.
 Wave: UVB wavelength array of the object.
 Gdasdata: Scalar string containing absolute path to GDAS file.

Outputs:

This function returns the extinction in the UVB region appropriate for the input LBLRTM model parameters at the wavelengths given by wave. Since the model only reaches down to 3672 Å, the extinction is extrapolated below that value.

Example:

```
uvext = UVEXTINCTION(Tellremparameters_object,Wave,'/here/lies/the/Gdasdata')
```

Modification History:

Written by: Natascha Rudolf, October 2013.

A.22 WHICHGDAS**Name:**

WHICHGDAS

Purpose:

This function selects the GDAS sounding data file that lies closest to the observation date.

Calling Sequence:

```
Result = WHICHGDAS(Obsdate)
```

Inputs:

Obsdate: Julian date of the observation (scalar float or double).

Outputs:

Result: Scalar string with absolute path of the closest GDAS sounding data file.

Common Blocks:

TELLREM_INFO: This common block contains relevant folder names and strings for running TELLREM. It has to be initialised by running LOADTELLREMINFO.

Example:

```
filename = WHICHGDAS(2456590.9276736d)
```

Modification History:

Written by: Natascha Rudolf, October 2013.

Appendix B

Annotated Example TAPE5

```

; record 1.1: $ signals LBLRTM to start, rest is comment
$ TAPE5 created by runlblrtm.pro
; record 1.2
  1  1  1  0  1  0  0  0  0  1  0  0  0  0  5  5
; record 1.3
 9089.909 10001.000    4.000 0.000E-00    0.000  0.0000 2.000E-04 1.000E-03
; record 1.4
  0.000    0.000    0.000    0.000    0.000    0.000    0.000
; record 3.1: user supplied model
  0  3  0  0  0  19  0    0.000  75.000    0.000  000.000
; record 3.2
 2.64800  0.00000  0.00000  0.00000  0.00000  0
; record 3.3A, use defaults
  2.000    5.000    8.000    0.000    0.000
; user defined atmospheric profile
; record 3.4
  50
; record 3.5
 9.160E-01 9.150E+02 2.874E+02    AA  GAAAAAAAAAAAA
; record 3.6.1 to 3.6.3
 1.080E+01 3.685E+02 2.231E-02 3.170E-01 9.173E-02 1.768E+00 2.120E+05 7.956E-06
 1.000E-04 6.260E-05 1.000E-04 1.781E-04
 0.000E+00 0.000E+00 6.000E-04
; repeating records 3.5 and 3.6.1 to 3.6.3 for all boundaries
 1.030E+00 9.000E+02 2.934E+02    AA  GAAAAAAAAAAAA
 4.300E+00 3.685E+02 2.280E-02 3.170E-01 9.114E-02 1.768E+00 2.120E+05 7.075E-06
 1.000E-04 5.074E-05 1.000E-04 1.884E-04
 0.000E+00 0.000E+00 6.000E-04
 1.518E+00 8.500E+02 2.909E+02    AA  GAAAAAAAAAAAA
-6.000E-01 3.685E+02 2.498E-02 3.170E-01 8.998E-02 1.768E+00 2.120E+05 5.372E-06
 1.000E-04 3.043E-05 1.000E-04 2.260E-04
 0.000E+00 0.000E+00 6.000E-04
 2.033E+00 8.000E+02 2.884E+02    AA  GAAAAAAAAAAAA
-6.200E+00 3.685E+02 2.722E-02 3.170E-01 8.950E-02 1.768E+00 2.120E+05 5.418E-06
 1.000E-04 3.356E-05 1.000E-04 2.495E-04
 0.000E+00 0.000E+00 6.000E-04
.....
.....
.....

```

```

.....
7.800E+01 1.507E-02 2.069E+02      AA  AAAAAAAAAAAAA
3.573E+00 3.447E+02 2.028E-01 7.810E-04 1.956E+01 7.364E-02 2.120E+05 3.000E-03
2.000E-04 1.244E-07 1.914E-11 2.639E-06
0.000E+00 0.000E+00 1.091E-08
8.300E+01 6.730E-03 2.045E+02      AA  AAAAAAAAAAAAA
2.963E+00 3.295E+02 2.818E-01 6.327E-04 2.879E+01 5.510E-02 2.130E+05 4.762E-03
2.000E-04 9.353E-08 1.914E-11 1.567E-06
0.000E+00 0.000E+00 1.091E-08
8.800E+01 2.931E-03 1.933E+02      AA  AAAAAAAAAAAAA
2.471E+00 2.996E+02 5.553E-01 5.215E-04 3.826E+01 4.086E-02 2.130E+05 1.817E-02
2.000E-04 9.000E-08 1.914E-11 9.149E-07
0.000E+00 0.000E+00 1.091E-08
; signalling the end of the repetition
-1
; end of user defined atmospheric profile
; restart LBLRTM and make it write ASCII file of transmittance (TAPE99)
; record 1.1 again
$ Make ASCII
; record 1.2 again only activating 'plotting'
HI=0 F4=0 CN=0 AE=0 EM=0 SC=0 FI=0 PL=1 TS=0 AM=0 MG=0 LA=0 MS=0 XS=0      0      0
; record 12.1
# Plot title not used
; record 12.2A
9090.909 10000.000 10.2000 001.0000 1 0 12 0 1.000 0 0 0
; record 12.3A
0.0000 1.2000 7.0200 0.2000 4 0 1 0 0 0 1 3 99
; terminate plotting
-1.
; % signals end of TAPE5 and terminates LBLRTM, rest comment
%
```

Appendix C

Additional Tables

C.1 Hydrogen emission line fluxes

Table C.1: The Paschen lines present in each object.

Object	3-24	3-23	3-22	3-21	3-20	3-19	3-18	3-17	3-16	3-15	3-14	3-13	3-12	3-11	3-10	3-9	3-8	3-7	3-6	3-5
S CrA	x	x	x	x	x ^d	x	x ^d	x	x ^a	x ^b	x	x ^c	x	x	x	x	x	x	x	x
TW Hya									x		x	x ^c	x	x	x	x	x	x	x	x
EX Lup												x ^c	x	x	x	x	x	x	x	x
GQ Lup									x		x	x ^c	x	x	x	x	x	x	x	x
HO Lup									x		x	x ^c	x	x	x	x	x	x	x	x
IM Lup																				
MV Lup																				
RU Lup					x ^d	x	x ^d	x	x ^a	x ^b	x	x ^c	x	x	x	x	x	x	x	x
MP Mus																				
V853 Oph																				
V2058 Oph							x ^d	x	x ^a	x ^b	x	x ^c	x	x	x	x	x	x	x	x
V2062 Oph																				
V2129 Oph																				
V2251 Oph																x	x	x	x	x
V2252 Oph															x	x	x	x	x	x
VV Sco																				
V895 Sco					x	x	x ^d	x	x ^a	x ^b	x	x ^c	x	x	x	x	x	x	x	x
V1279 Sco																				
V4046 Sgr																				
Sz77																				

Notes. Line 3-4 is lost due to telluric lines; (a) blend with Ca II infrared triplet line at 8498 Å; (b) blend with Ca II infrared triplet line at 8542 Å; (c) blend with Ca II infrared triplet line at 8662 Å; (d) blend with other line.

Table C.2: The Brackett lines present in each object.

Object	4-20	4-19	4-18	4-17	4-16	4-15	4-14	4-13	4-12	4-11	4-10	4-7
S CrA	x	x	x	x	x	x	x	x	x	x	x	x
TW Hya												x
EX Lup												x
GQ Lup												x
HO Lup										x	x	x
IM Lup												
MV Lup												
RU Lup	x	x	x	x	x	x	x	x	x	x	x	x
MP Mus												x
V853 Oph												
V2058 Oph										x	x	x
V2062 Oph										x	x	x
V2129 Oph												
V2251 Oph												x
V2252 Oph												x
VV Sco												x
V895 Sco								x	x	x	x	x
V1279 Sco												
V4046 Sgr												x
Sz77												

Note. Lines 4-9 and 4-8 are lost due to telluric lines and line 4-7 is the last in the spectral range of X-Shooter.

Table C.3: The wavelength positions and velocity ranges used as continuum and line in the line flux measurements of the deviation fluxes for the determination of the best template.

Wavelength in Å	Continuum start in km s ⁻¹	Continuum end in km s ⁻¹	Flux summation start/end in km s ⁻¹
5800	500	1500	400
6850	500	1500	400
8000	500	1500	400
9800	500	1500	400
11050	500	1500	400
11500	500	1500	400
12200	500	1500	400
12490	500	1500	400
13000	500	1500	400
13300	500	1500	400
14750	500	1500	400
16000	500	1500	400
16600	500	1500	400
17000	500	1500	400
17230	500	1500	400
17600	500	1500	400
18000	500	1500	400
20000	500	1500	400
20440	500	1500	400
20850	500	1500	400
21200	500	1500	400
21490	500	1500	400
22000	500	1500	400
22500	500	1500	400
23070	500	1500	400

C.2 Flux calibration

Table C.4: The regions excluded in the determination of the individual response curves using the telluric standards.

Wavelength in Å	Feature	Width in Å
3662.2	Balmer end	10
3750	High Balmer lines	140
3835.4	2-9	40
3889.1	2-8	50
3970.1	2-7	60
4101.7	2-6	70
4340.5	2-5	86
4861.4	2-4	80
6562.8	2-3	80
7645	O ₂ band	110
8286.5	Paschen end	50
8413.3	3-19	5
8438	3-18	8
8467.3	3-17	24
8502.5	3-16	30
8545.4	3-15	30
8598.4	3-14	40
8665	3-13	80
8750.5	3-12	80
8862.9	3-11	80
9014.9	3-10	80
9229	3-9	90
9546	3-8	90
10049.4	3-7	80
10938.2	3-6	190
11412.5	Telluric residuals	575
12818.1	3-5	150
14848.6	Brackett end	40
15260.6	4-19	50
15341.8	4-18	60
15438.9	4-17	100
15556.5	4-16	100
15700.7	4-15	100
15880.6	4-14	100
16109.3	4-13	100
16407.2	4-12	100
16806.5	4-11	80
17362.1	4-10	80
21655.3	4-7	100

Note. The region excluded, given by the width, is centred on the wavelength.

C.3 Additional reduction steps

Table C.5: The radial velocity of each object determined from Li I 6708 Å.

Object	Radial velocity in km s ⁻¹	Object	Radial velocity in km s ⁻¹
S CrA	-22.9 ± 0.6	V2058 Oph	-14.8 ± 0.1
TW Hya	29.7 ± 0.1	V2062 Oph	-17.6 ± 0.1
EX Lup	-7.8 ± 0.2	V2129 Oph	-18.3 ± 0.1
GQ Lup	-8.6 ± 0.1	V2251 Oph	-20.3 ± 0.2
HO Lup	-11.0 ± 0.2	V2252 Oph	-18.9 ± 0.1
IM Lup	-8.2 ± 0.1	VV Sco	-15.8 ± 0.1
MV Lup	-6.4 ± 0.1	V895 Sco	-14.8 ± 0.2
RU Lup	-7.5 ± 0.2	V1279 Sco	-8.3 ± 0.2
MP Mus	10.9 ± 0.1	V4046 Sgr	-25.1 ± 0.1
V853 Oph	-15.5 ± 0.2	Sz77	-8.5 ± 0.1

Note. No barycentric correction is applied.

C.4 The temperature T and the density n_e in the emitting gas

Table C.6: The temperature T and density n_e of the five models with lowest χ_{red}^2 for each series of line ratios for S CrA.

Pan _{up} /Paβ			Brγ/Pan _{up}			Brn _{up} /Brγ		
T in K	n_e in cm ⁻³	χ_{red}^2	T in K	n_e in cm ⁻³	χ_{red}^2	T in K	n_e in cm ⁻³	χ_{red}^2
1000	10 ¹⁰	2.57	3000	10 ¹⁰	2.03	5000	10 ⁹	3.19
1000	10 ⁹	4.23	3000	10 ⁹	2.55	3000	10 ⁹	3.65
3000	10 ¹⁰	4.96	5000	10 ⁹	2.67	3000	10 ⁸	5.30
500	10 ¹⁰	8.15	1000	10 ⁸	3.22	7500	10 ⁹	6.04
500	10 ⁸	9.32	1000	10 ¹⁰	3.36	1000	10 ⁷	6.66

Table C.7: The temperature T and density n_e of the five models with lowest χ_{red}^2 for each series of line ratios for TW Hya.

Pan _{up} /Paβ			Brγ/Pan _{up}		
T in K	n_e in cm ⁻³	χ_{red}^2	T in K	n_e in cm ⁻³	χ_{red}^2
7500	10 ¹²	0.86	30000	10 ¹⁴	2.42
15000	10 ¹³	1.11	30000	10 ¹³	2.43
20000	10 ¹⁴	1.20	20000	10 ¹³	2.57
15000	10 ¹⁴	1.32	20000	10 ¹⁴	2.59
20000	10 ¹³	1.34	30000	10 ⁷	2.66

Table C.8: The temperature T and density n_e of the five models with lowest χ_{red}^2 for each series of line ratios for EX Lup.

Pan _{up} /Pa β			Br γ /Pan _{up}		
T in K	n_e in cm ⁻³	χ_{red}^2	T in K	n_e in cm ⁻³	χ_{red}^2
1000	10 ¹¹	2.63	500	10 ⁹	25.90
3000	10 ¹¹	3.41	1000	10 ⁹	26.30
3000	10 ¹⁰	3.60	3000	10 ⁹	29.02
500	10 ¹¹	5.00	5000	10 ¹⁰	29.14
1000	10 ¹⁰	5.32	3000	10 ¹⁰	29.26

Table C.9: The temperature T and density n_e of the five models with lowest χ_{red}^2 for each series of line ratios for GQ Lup.

Pan _{up} /Pa β			Br γ /Pan _{up}		
T in K	n_e in cm ⁻³	χ_{red}^2	T in K	n_e in cm ⁻³	χ_{red}^2
10000	10 ¹⁰	0.16	7500	10 ¹⁰	0.51
7500	10 ¹⁰	0.69	10000	10 ¹⁰	0.77
12500	10 ¹⁰	0.77	7500	10 ⁹	0.86
7500	10 ⁹	0.90	5000	10 ¹⁰	0.89
10000	10 ⁹	1.36	10000	10 ⁹	0.93

Table C.10: The temperature T and density n_e of the five models with lowest χ_{red}^2 for each series of line ratios for HO Lup.

Pan _{up} /Pa β			Br γ /Pan _{up}			Brn _{up} /Br γ		
T in K	n_e in cm ⁻³	χ_{red}^2	T in K	n_e in cm ⁻³	χ_{red}^2	T in K	n_e in cm ⁻³	χ_{red}^2
5000	10 ¹⁰	0.51	1000	10 ⁹	11.67	5000	10 ¹⁰	0.25
7500	10 ¹⁰	1.86	3000	10 ⁹	13.00	7500	10 ¹⁰	0.34
5000	10 ⁹	2.10	500	10 ⁹	13.72	7500	10 ⁹	0.40
3000	10 ⁹	2.68	1000	10 ¹⁰	15.21	5000	10 ⁹	1.24
3000	10 ¹⁰	3.27	500	10 ¹⁰	15.62	1000	10 ⁸	1.32

Table C.11: The temperature T and density n_e of the five models with lowest χ_{red}^2 for each series of line ratios for RU Lup.

Pan _{up} /Pa β			Br γ /Pan _{up}			Brn _{up} /Br γ		
T in K	n_e in cm ⁻³	χ_{red}^2	T in K	n_e in cm ⁻³	χ_{red}^2	T in K	n_e in cm ⁻³	χ_{red}^2
1000	10 ¹⁰	3.10	3000	10 ⁹	2.36	3000	10 ⁹	2.80
1000	10 ⁹	3.76	1000	10 ¹⁰	2.56	5000	10 ⁹	7.71
3000	10 ¹⁰	3.81	1000	10 ⁹	3.18	1000	10 ⁹	8.80
3000	10 ⁹	7.81	500	10 ¹⁰	3.59	3000	10 ⁸	9.30
500	10 ⁸	7.89	500	10 ⁸	4.47	1000	10 ¹⁰	9.83

Table C.12: The temperature T and density n_e of the five models with lowest χ_{red}^2 for each series of line ratios for MP Mus.

Pan _{up} /Pa β			Br γ /Pan _{up}		
T in K	n_e in cm ⁻³	χ_{red}^2	T in K	n_e in cm ⁻³	χ_{red}^2
5000	10 ⁸	0.29	12500	10 ⁹	6.97
7500	10 ⁸	0.31	10000	10 ⁹	7.02
20000	10 ¹⁰	0.31	20000	10 ¹⁰	7.07
12500	10 ⁹	0.33	7500	10 ⁹	7.09
15000	10 ⁹	0.36	15000	10 ⁹	7.15

Table C.13: The temperature T and density n_e of the five models with lowest χ_{red}^2 for each series of line ratios for V853 Oph.

Pan _{up} /Pa β		
T in K	n_e in cm ⁻³	χ_{red}^2
1000	10 ¹⁰	5.61
500	10 ¹⁰	5.86
500	10 ¹¹	10.09
3000	10 ¹⁰	10.32
1000	10 ¹¹	10.32

Table C.14: The temperature T and density n_e of the five models with lowest χ_{red}^2 for each series of line ratios for V2058 Oph.

Pan _{up} /Pa β			Br γ /Pan _{up}			Brn _{up} /Br γ		
T in K	n_e in cm ⁻³	χ_{red}^2	T in K	n_e in cm ⁻³	χ_{red}^2	T in K	n_e in cm ⁻³	χ_{red}^2
3000	10 ¹⁰	3.32	1000	10 ⁹	5.33	5000	10 ¹⁰	6.45
1000	10 ¹⁰	3.49	500	10 ¹⁰	6.44	7500	10 ¹⁰	6.63
1000	10 ⁹	4.16	500	10 ⁹	6.77	10000	10 ¹⁰	7.85
3000	10 ⁹	7.14	1000	10 ¹⁰	7.74	7500	10 ⁹	8.88
500	10 ⁸	7.53	3000	10 ⁹	9.79	10000	10 ⁹	9.28

Table C.15: The temperature T and density n_e of the five models with lowest χ_{red}^2 for each series of line ratios for V2062 Oph.

Pan _{up} /Pa β			Br γ /Pan _{up}			Brn _{up} /Br γ		
T in K	n_e in cm ⁻³	χ_{red}^2	T in K	n_e in cm ⁻³	χ_{red}^2	T in K	n_e in cm ⁻³	χ_{red}^2
5000	10 ¹⁰	1.04	1000	10 ⁹	15.22	500	10 ¹¹	17.32
3000	10 ¹⁰	2.27	3000	10 ⁹	16.64	1000	10 ¹¹	19.58
3000	10 ⁹	2.43	500	10 ⁹	17.31	5000	10 ¹²	24.27
7500	10 ¹⁰	3.28	1000	10 ¹⁰	20.44	5000	10 ¹³	24.79
5000	10 ⁹	3.42	500	10 ¹⁰	20.58	7500	10 ¹⁴	24.93

Table C.16: The temperature T and density n_e of the five models with lowest χ_{red}^2 for each series of line ratios for V2251 Oph.

Pan _{up} /Pa β			Br γ /Pan _{up}		
T in K	n_e in cm ⁻³	χ_{red}^2	T in K	n_e in cm ⁻³	χ_{red}^2
3000	10 ⁷	0.74	20000	10 ⁹	10.76
5000	10 ⁷	0.78	30000	10 ¹⁰	10.80
7500	10 ⁷	0.83	30000	10 ⁹	10.80
30000	10 ⁹	0.89	15000	10 ⁹	10.91
10000	10 ⁷	0.89	30000	10 ⁸	10.93

Table C.17: The temperature T and density n_e of the five models with lowest χ_{red}^2 for each series of line ratios for V2252 Oph.

Pan _{up} /Pa β			Br γ /Pan _{up}		
T in K	n_e in cm ⁻³	χ_{red}^2	T in K	n_e in cm ⁻³	χ_{red}^2
12500	10 ¹⁰	1.10	3000	10 ⁹	13.30
10000	10 ¹⁰	1.17	5000	10 ⁹	13.89
10000	10 ¹¹	1.28	1000	10 ⁹	14.42
15000	10 ¹⁰	1.47	7500	10 ¹⁰	15.00
12500	10 ¹¹	1.52	7500	10 ⁹	15.07

Table C.18: The temperature T and density n_e of the five models with lowest χ_{red}^2 for each series of line ratios for VV Sco.

Pan _{up} /Pa β			Br γ /Pan _{up}		
T in K	n_e in cm ⁻³	χ_{red}^2	T in K	n_e in cm ⁻³	χ_{red}^2
1000	10 ⁷	2.55	3000	10 ⁸	1.36
3000	10 ⁷	2.71	10000	10 ⁹	1.53
5000	10 ⁷	3.14	7500	10 ⁹	1.55
500	10 ⁷	3.25	5000	10 ⁸	1.57
7500	10 ⁷	3.53	12500	10 ⁹	1.66

Table C.19: The temperature T and density n_e of the five models with lowest χ_{red}^2 for each series of line ratios for V895 Sco.

Pan _{up} /Pa β			Br γ /Pan _{up}			Brn _{up} /Br γ		
T in K	n_e in cm ⁻³	χ_{red}^2	T in K	n_e in cm ⁻³	χ_{red}^2	T in K	n_e in cm ⁻³	χ_{red}^2
5000	10 ¹⁰	0.60	5000	10 ¹⁰	0.45	7500	10 ¹⁰	0.71
5000	10 ⁹	0.97	5000	10 ⁹	0.66	10000	10 ¹⁰	0.85
7500	10 ¹⁰	1.07	7500	10 ⁹	0.68	12500	10 ⁹	0.98
3000	10 ⁹	2.34	3000	10 ¹⁰	0.97	10000	10 ⁹	0.98
10000	10 ¹⁰	2.88	7500	10 ¹⁰	1.05	12500	10 ¹⁰	1.40

Table C.20: The temperature T and density n_e of the five models with lowest χ_{red}^2 for each series of line ratios for V4046 Sgr.

$Pan_{\text{up}}/Pa\beta$			$Br\gamma/Pan_{\text{up}}$		
T in K	n_e in cm^{-3}	χ_{red}^2	T in K	n_e in cm^{-3}	χ_{red}^2
1000	10^{14}	24.65	7500	10^{14}	18.13
500	10^{14}	29.87	5000	10^{13}	18.14
500	10^{13}	31.34	5000	10^{14}	18.38
1000	10^{13}	31.58	7500	10^{13}	18.67
3000	10^{14}	69.55	10000	10^{14}	18.99

C.5 Using the newly determined A_V values for the estimation of the temperature T and the electron density n_e

Table C.21: The temperature T and density n_e of the five models with lowest χ_{red}^2 for each series of line ratios for S CrA.

Pan _{up} /Pa β			Br γ /Pan _{up}			Brn _{up} /Br γ		
T in K	n_e in cm ⁻³	χ_{red}^2	T in K	n_e in cm ⁻³	χ_{red}^2	T in K	n_e in cm ⁻³	χ_{red}^2
1000	10 ¹⁰	2.20	3000	10 ⁹	2.10	5000	10 ⁹	3.36
1000	10 ⁹	4.38	1000	10 ¹⁰	2.54	3000	10 ⁹	3.40
3000	10 ¹⁰	6.17	3000	10 ¹⁰	2.78	3000	10 ⁸	5.36
500	10 ⁹	6.36	5000	10 ⁹	3.37	7500	10 ⁹	6.40
500	10 ⁹	8.54	1000	10 ⁸	3.54	1000	10 ⁷	6.85

Table C.22: The temperature T and density n_e of the five models with lowest χ_{red}^2 for each series of line ratios for HO Lup.

Pan _{up} /Pa β			Br γ /Pan _{up}			Brn _{up} /Br γ		
T in K	n_e in cm ⁻³	χ_{red}^2	T in K	n_e in cm ⁻³	χ_{red}^2	T in K	n_e in cm ⁻³	χ_{red}^2
10000	10 ¹⁰	0.53	7500	10 ¹⁰	0.83	7500	10 ¹⁰	0.03
125000	10 ¹⁰	0.79	7500	10 ⁹	1.03	10000	10 ¹⁰	0.32
7500	10 ⁹	1.04	5000	10 ¹⁰	1.07	7500	10 ⁹	0.40
10000	10 ⁹	1.12	10000	10 ¹⁰	1.24	10000	10 ⁹	0.43
15000	10 ¹⁰	1.52	10000	10 ⁹	1.30	3000	10 ⁸	0.50

Table C.23: The temperature T and density n_e of the five models with lowest χ_{red}^2 for each series of line ratios for RU Lup.

Pan _{up} /Pa β			Br γ /Pan _{up}			Brn _{up} /Br γ		
T in K	n_e in cm ⁻³	χ_{red}^2	T in K	n_e in cm ⁻³	χ_{red}^2	T in K	n_e in cm ⁻³	χ_{red}^2
1000	10 ¹⁰	2.33	1000	10 ⁹	3.01	3000	10 ⁹	3.08
1000	10 ⁹	3.68	500	10 ¹⁰	3.99	1000	10 ⁹	7.84
3000	10 ¹⁰	5.07	1000	10 ¹⁰	4.08	5000	10 ⁹	8.24
500	10 ¹⁰	7.51	3000	10 ⁹	4.61	3000	10 ⁸	9.73
500	10 ⁹	8.68	500	10 ⁹	5.03	1000	10 ¹⁰	10.28

Table C.24: The temperature T and density n_e of the five models with lowest χ_{red}^2 for each series of line ratios for V2058 Oph.

Pan _{up} /Pa β			Br γ /Pan _{up}			Brn _{up} /Br γ		
T in K	n_e in cm ⁻³	χ_{red}^2	T in K	n_e in cm ⁻³	χ_{red}^2	T in K	n_e in cm ⁻³	χ_{red}^2
5000	10 ¹⁰	1.15	5000	10 ¹⁰	1.15	7500	10 ¹⁰	6.66
3000	10 ¹⁰	1.54	3000	10 ¹⁰	1.58	10000	10 ¹⁰	6.72
3000	10 ⁹	1.54	7500	10 ¹⁰	1.68	12500	10 ¹⁰	7.48
5000	10 ⁹	3.37	7500	10 ⁹	1.91	15000	10 ¹⁰	8.44
7500	10 ¹⁰	3.74	3000	10 ⁸	2.08	5000	10 ¹⁰	8.52

Table C.25: The temperature T and density n_e of the five models with lowest χ_{red}^2 for each series of line ratios for V2062 Oph.

Pan _{up} /Pa β			Br γ /Pan _{up}			Brn _{up} /Br γ		
T in K	n_e in cm ⁻³	χ_{red}^2	T in K	n_e in cm ⁻³	χ_{red}^2	T in K	n_e in cm ⁻³	χ_{red}^2
20000	10 ⁸	0.26	3000	10 ⁵	0.97	500	10 ¹¹	15.59
15000	10 ⁸	0.33	5000	10 ⁵	1.33	1000	10 ¹¹	20.55
30000	10 ¹⁰	0.35	1000	10 ⁵	1.39	3000	10 ¹²	24.32
30000	10 ⁹	0.44	5000	10 ⁴	1.44	5000	10 ¹⁴	25.92
7500	10 ⁷	0.45	5000	10 ³	1.53	5000	10 ¹³	26.16

Table C.26: The temperature T and density n_e of the five models with lowest χ_{red}^2 for each series of line ratios for V895 Sco.

Pan _{up} /Pa β			Br γ /Pan _{up}			Brn _{up} /Br γ		
T in K	n_e in cm ⁻³	χ_{red}^2	T in K	n_e in cm ⁻³	χ_{red}^2	T in K	n_e in cm ⁻³	χ_{red}^2
7500	10 ¹⁰	0.67	5000	10 ¹⁰	0.47	7500	10 ¹⁰	0.75
5000	10 ⁹	0.70	7500	10 ¹⁰	0.54	10000	10 ¹⁰	0.78
5000	10 ¹⁰	0.95	7500	10 ⁹	0.65	12500	10 ⁹	0.93
10000	10 ¹⁰	2.12	10000	10 ⁹	0.92	10000	10 ⁹	1.06
7500	10 ⁹	2.20	3000	10 ⁸	1.02	12500	10 ¹⁰	1.26

Appendix D

Additional Plots

D.1 Uncertainty of relative flux calibration

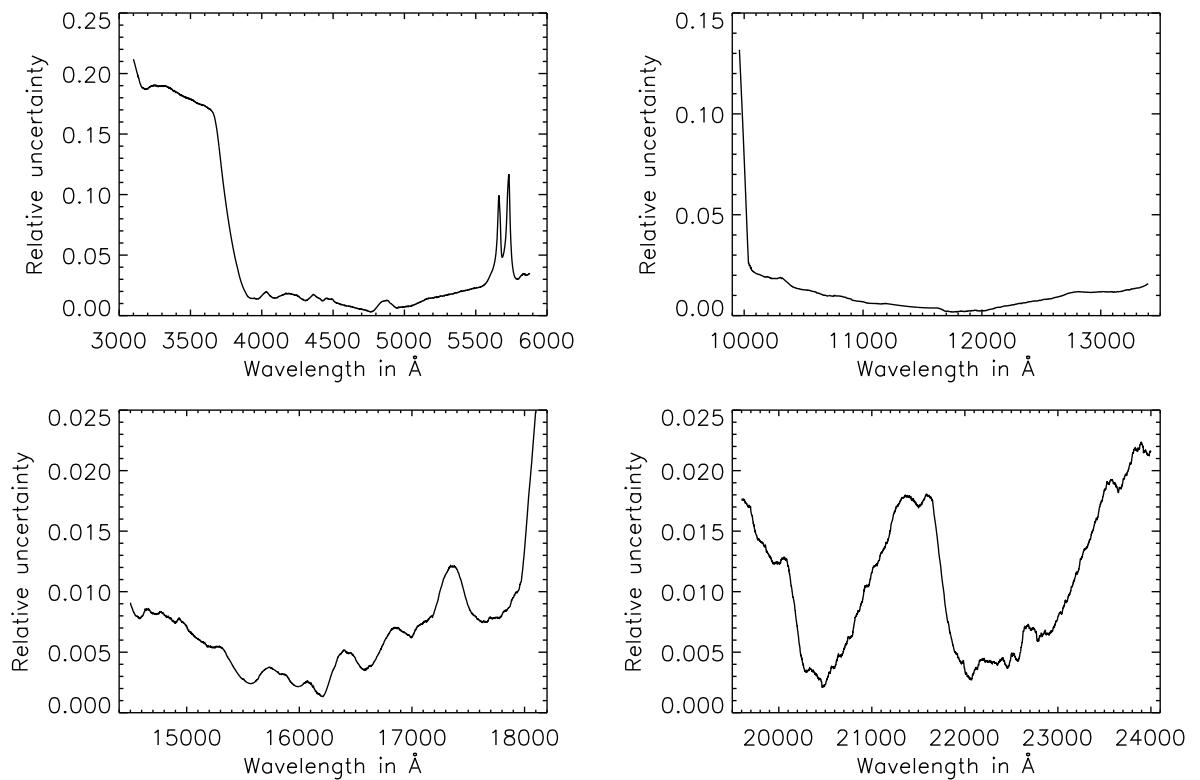


Figure D.1: The relative uncertainty of the relative flux calibration for the UVB arm (*upper left*), the NIR1 arm (*upper right*), the NIR2 arm (*lower left*), and the NIR3 arm (*lower right*).

D.2 Uncertainty of absolute flux calibration

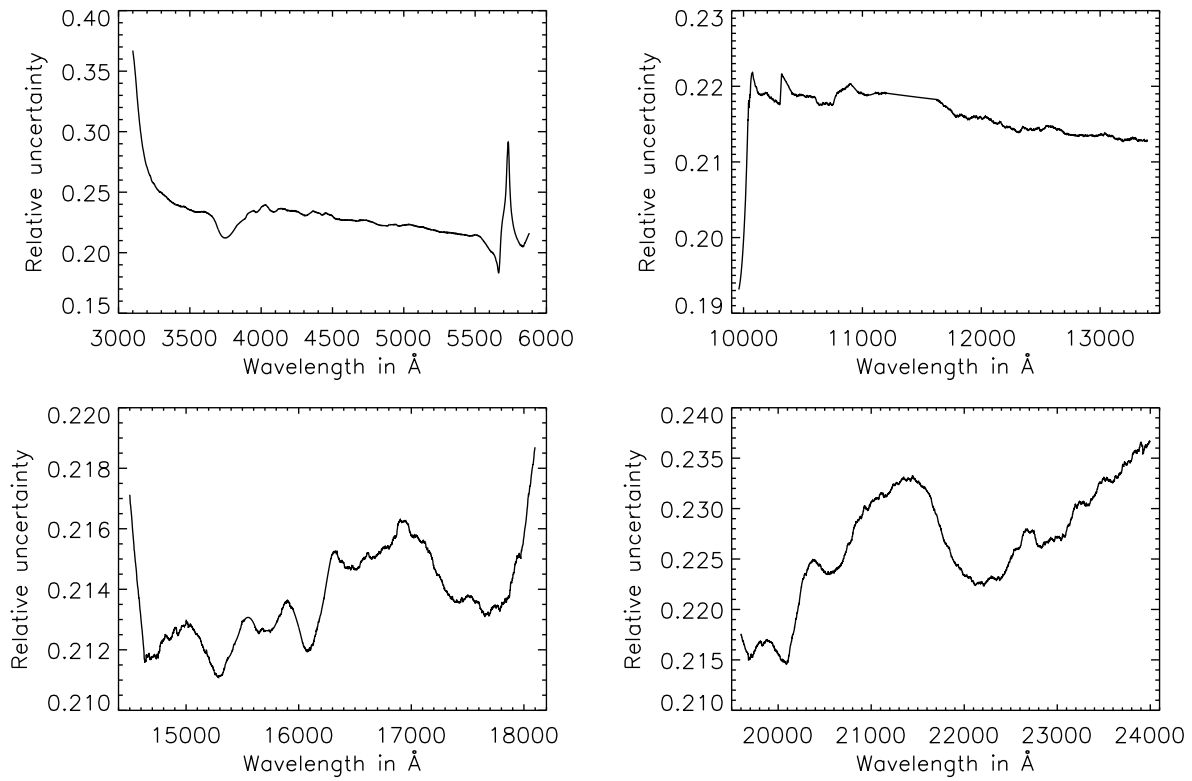


Figure D.2: The relative uncertainty of the absolute flux calibration for the UVB arm (*upper left*), the NIR1 arm (*upper right*), the NIR2 arm (*lower left*), and the NIR3 arm (*lower right*).

List of Figures

1.1	Dark cloud Barnard 68	2
1.2	Star forming region NGC 2174	3
1.3	Schematic Hertzsprung-Russel (HR) diagram	4
2.1	Example VLT/X-Shooter spectrum of RU Lup	9
2.2	Measured line flux ratios and calculated case B models from Bary et al. (2008)	10
2.3	Sketch of model of disk accretion in CTTS	11
2.4	Extinction curves for different R_V	13
2.5	Grain size distributions of carbonaceous-silicate grain model of Weingartner & Draine (2001)	15
3.1	Tentative spectrum of RU Lup	20
3.2	Tentative spectrum of IM Lup	21
3.3	Individual response curves determined for each arm for first 7 objects	24
3.4	As Figure 3.3, but for remaining 5 objects	25
3.5	Individual response curves normalised and colour-coded by airmass	26
3.6	Comparison of spectra of RU Lup from both flux calibrations	27
3.7	Comparison of spectra of IM Lup from both flux calibrations	27
4.1	Example of GDAS sounding data text file	39
5.1	Example of line flux measurement	48
5.2	Example of absorption in red side of lines	50
5.3	Relative statistical uncertainty of line flux	50
5.4	Relative uncertainty due to template subtraction	51
5.5	Relative uncertainty of relative flux calibration	52
5.6	Relative uncertainty of absolute flux calibration	52
5.7	Effect of reddening on ratios of Paschen and Brackett lines with common upper level	56
6.1	Sensitivity of case B models	60
6.2	Observed line ratios of S CrA together with five case B models with lowest χ_{red}^2	62
6.3	Observed line ratios of TW Hya together with five case B models with lowest χ_{red}^2	63
6.4	Observed line ratios of EX Lup together with five case B models with lowest χ_{red}^2	63
6.5	Observed line ratios of GQ Lup together with five case B models with lowest χ_{red}^2	64
6.6	Observed line ratios of HO Lup together with five case B models with lowest χ_{red}^2	64
6.7	Observed line ratios of RU Lup together with five case B models with lowest χ_{red}^2	65
6.8	Observed line ratios of MP Mus together with five case B models with lowest χ_{red}^2	65
6.9	Observed line ratios of V853 Oph together with five case B models with lowest χ_{red}^2	66
6.10	Observed line ratios of V2058 Oph together with five case B models with lowest χ_{red}^2	66
6.11	Observed line ratios of V2062 Oph together with five case B models with lowest χ_{red}^2	67

6.12	Observed line ratios of V2251 Oph together with five case B models with lowest χ_{red}^2	67
6.13	Observed line ratios of V2252 Oph together with five case B models with lowest χ_{red}^2	68
6.14	Observed line ratios of VV Sco together with five case B models with lowest χ_{red}^2	68
6.15	Observed line ratios of V895 Sco together with five case B models with lowest χ_{red}^2	69
6.16	Observed line ratios of V4046 Sgr together with five case B models with lowest χ_{red}^2	69
6.17	Extinction of S CrA, HO Lup, RU Lup, V2058 Oph, V2062 Oph, and V895 Sco together with two fits using Equation 5.20	73
6.18	Observed line ratios of S CrA together with five case B models with lowest χ_{red}^2	78
6.19	Observed line ratios of HO Lup together with five case B models with lowest χ_{red}^2	79
6.20	Observed line ratios of RU Lup together with five case B models with lowest χ_{red}^2	79
6.21	Observed line ratios of V2058 Oph together with five case B models with lowest χ_{red}^2	80
6.22	Observed line ratios of V2062 Oph together with five case B models with lowest χ_{red}^2	80
6.23	Observed line ratios of V895 Sco together with five case B models with lowest χ_{red}^2	81
D.1	Relative uncertainty of relative flux calibration	119
D.2	Relative uncertainty of absolute flux calibration	120

List of Tables

3.1	Sample and observational details	18
3.2	Telluric standard stars used for flux calibration	22
4.1	Content of <code>tellrem</code> input file	40
4.2	Structure tags and content of output of <code>tellrem</code>	42
5.1	Template spectra used for object spectra in line flux determination	48
5.2	Velocity ranges used in line flux measurements	49
5.3	Regions excluded in determination of mean of individual responses	51
5.4	Literature extinction values A_V for each object	58
6.1	Temperature T and electron density n_e of best fitting model for each series of line ratios	61
6.2	Results for extinction value A_V and exponent of the power law α	74
6.3	Extinction values A_V used in Section 6.1 and found in Section 6.3	75
6.4	Temperature T and electron density n_e of best fitting model for each series of line ratios	77
C.1	Paschen lines present in each object	108
C.2	Brackett lines present in each object	109
C.3	Wavelength positions and velocity ranges used in pseudo line flux measurements	110
C.4	Regions excluded in determination of individual response curves using telluric standards.	111
C.5	Radial velocity of each object	112
C.6	Temperature T and density n_e of five best-fit models for each series of line ratios for S CrA	112
C.7	Temperature T and density n_e of five best-fit models for each series of line ratios for TW Hya	112
C.8	Temperature T and density n_e of five best-fit models for each series of line ratios for EX Lup	113
C.9	Temperature T and density n_e of five best-fit models for each series of line ratios for GQ Lup	113
C.10	Temperature T and density n_e of five best-fit models for each series of line ratios for HO Lup	113
C.11	Temperature T and density n_e of five best-fit models for each series of line ratios for RU Lup	113
C.12	Temperature T and density n_e of five best-fit models for each series of line ratios for MP Mus	114
C.13	Temperature T and density n_e of five best-fit models for each series of line ratios for V853 Oph	114
C.14	Temperature T and density n_e of five best-fit models for each series of line ratios for V2058 Oph	114

C.15	Temperature T and density n_e of five best-fit models for each series of line ratios for V2062 Oph	114
C.16	Temperature T and density n_e of five best-fit models for each series of line ratios for V2251 Oph	115
C.17	Temperature T and density n_e of five best-fit models for each series of line ratios for V2252 Oph	115
C.18	Temperature T and density n_e of five best-fit models for each series of line ratios for VV Sco	115
C.19	Temperature T and density n_e of five best-fit models for each series of line ratios for V895 Sco	115
C.20	Temperature T and density n_e of five best-fit models for each series of line ratios for V4046 Sgr	116
C.21	Temperature T and density n_e of five best-fit models for each series of line ratios for S CrA	117
C.22	Temperature T and density n_e of five best-fit models for each series of line ratios for HO Lup	117
C.23	Temperature T and density n_e of five best-fit models for each series of line ratios for RU Lup	117
C.24	Temperature T and density n_e of five best-fit models for each series of line ratios for V2058 Oph	118
C.25	Temperature T and density n_e of five best-fit models for each series of line ratios for V2062 Oph	118
C.26	Temperature T and density n_e of five best-fit models for each series of line ratios for V895 Sco	118

Bibliography

- Alencar, S. H. P. & Basri, G. 2000, *AJ*, 119, 1881
- Alencar, S. H. P., Johns-Krull, C. M., & Basri, G. 2001, *AJ*, 122, 3335
- Appenzeller, I. & Mundt, R. 1989, *A&A Rev.*, 1, 291
- Bacciotti, F., Mundt, R., Ray, T. P., et al. 2000, *ApJ*, 537, L49
- Baker, J. G. & Menzel, D. H. 1938, *ApJ*, 88, 52
- Barrado y Navascués, D. & Martín, E. L. 2003, *AJ*, 126, 2997
- Bary, J. S., Matt, S. P., Skrutskie, M. F., et al. 2008, *ApJ*, 687, 376
- Beck, T. L., McGregor, P. J., Takami, M., & Pyo, T.-S. 2008, *ApJ*, 676, 472
- Bell, E. F., McIntosh, D. H., Katz, N., & Weinberg, M. D. 2003, *ApJ*, 585, L117
- Bertoldi, F., Timmermann, R., Rosenthal, D., Drapatz, S., & Wright, C. M. 1999, *A&A*, 346, 267
- Bouvier, J., Alencar, S. H. P., Bouvier, T., et al. 2007, *A&A*, 463, 1017
- Bouvier, J., Cabrit, S., Fernandez, M., Martin, E. L., & Matthews, J. M. 1993, *A&A*, 272, 176
- Bradley, J., Dai, Z. R., Erni, R., et al. 2005, *Science*, 307, 244
- Calvet, N. & Gullbring, E. 1998, *ApJ*, 509, 802
- Cardelli, J. A., Clayton, G. C., & Mathis, J. S. 1989, *ApJ*, 345, 245
- Carmona, A., van den Ancker, M. E., & Henning, T. 2007, *A&A*, 464, 687
- Chapman, N. L., Mundy, L. G., Lai, S.-P., & Evans, II, N. J. 2009, *ApJ*, 690, 496
- Clough, S. A., Shephard, M. W., Mlawer, E. J., et al. 2005, *J. Quant. Spec. Radiat. Transf.*, 91, 233
- Cohen, M. & Kuhl, L. V. 1979, *ApJS*, 41, 743
- Cohen, M., Wheaton, W. A., & Megeath, S. T. 2003, *AJ*, 126, 1090
- Cortes, S. R., Meyer, M. R., Carpenter, J. M., et al. 2009, *ApJ*, 697, 1305
- Currie, T. & Sicilia-Aguilar, A. 2011, *ApJ*, 732, 24
- Dobbs, C. L., Krumholz, M. R., Ballesteros-Paredes, J., et al. 2013, *ArXiv e-prints*
- Dodin, A. V. & Lamzin, S. A. 2012, *Astronomy Letters*, 38, 649
- Dodin, A. V., Lamzin, S. A., & Chumtunov, G. A. 2012, *Astronomy Letters*, 38, 167

- Donati, J.-F., Jardine, M. M., Gregory, S. G., et al. 2007, *MNRAS*, 380, 1297
- Draine, B. T. 1989, in *ESA Special Publication*, Vol. 290, *Infrared Spectroscopy in Astronomy*, ed. E. Böhm-Vitense, 93–98
- Draine, B. T. 2003, *ARA&A*, 41, 241
- Dupree, A. K., Brickhouse, N. S., Cranmer, S. R., et al. 2012, *ApJ*, 750, 73
- Dutrey, A., Semenov, D., Chapillon, E., et al. 2014, *ArXiv e-prints*
- Edwards, S., Fischer, W., Hillenbrand, L., & Kwan, J. 2006, *ApJ*, 646, 319
- Edwards, S., Fischer, W., Kwan, J., Hillenbrand, L., & Dupree, A. K. 2003, *ApJ*, 599, L41
- Edwards, S., Kwan, J., Fischer, W., et al. 2013, *ApJ*, 778, 148
- Eisner, J. A. 2007, *Nature*, 447, 562
- Eisner, J. A., Chiang, E. I., & Hillenbrand, L. A. 2006, *ApJ*, 637, L133
- ESO. 2010, *X-Shooter User Manual*, Issue P86.1, Doc. No.: VLT-MAN-ESO-14650-4942
- ESO. 2012, *X-Shooter Pipeline User Manual*, Issue 10.0, Doc. No.: VLT-MAN-ESO-14650-4840
- Evans, II, N. J., Dunham, M. M., Jørgensen, J. K., et al. 2009, *ApJS*, 181, 321
- Finkenzeller, U. & Basri, G. 1987, *ApJ*, 318, 823
- Fischer, W., Kwan, J., Edwards, S., & Hillenbrand, L. 2008, *ApJ*, 687, 1117
- Fitzpatrick, E. L. 1999, *PASP*, 111, 63
- Fitzpatrick, E. L. & Massa, D. 2009, *ApJ*, 699, 1209
- Folha, D. F. M. & Emerson, J. P. 1998, *Ap&SS*, 261, 147
- Folha, D. F. M. & Emerson, J. P. 2001, *A&A*, 365, 90
- Frank, A., Ray, T. P., Cabrit, S., et al. 2014, *ArXiv e-prints*
- Furlan, E., Watson, D. M., McClure, M. K., et al. 2009, *ApJ*, 703, 1964
- Gahm, G. F., Loden, K., Gullbring, E., & Hartstein, D. 1995, *A&A*, 301, 89
- Galazutdinov, G., Stachowska, W., Musaev, F., et al. 2002, *A&A*, 396, 987
- González-Fernández, C., Asensio Ramos, A., Garzón, F., Cabrera-Lavers, A., & Hammersley, P. L. 2014, *ApJ*, 782, 86
- Gregory, S. G., Jardine, M., Simpson, I., & Donati, J.-F. 2006, *MNRAS*, 371, 999
- Güdel, M., Skinner, S. L., Audard, M., Briggs, K. R., & Cabrit, S. 2008, *A&A*, 478, 797
- Güdel, M., Skinner, S. L., Briggs, K. R., et al. 2005, *ApJ*, 626, L53
- Gullbring, E., Calvet, N., Muzerolle, J., & Hartmann, L. 2000, *ApJ*, 544, 927
- Gullbring, E., Hartmann, L., Briceno, C., & Calvet, N. 1998, *ApJ*, 492, 323
- Günther, H. M., Schmitt, J. H. M. M., Robrade, J., & Liefke, C. 2007, *A&A*, 466, 1111
- Hamann, F. & Persson, S. E. 1992, *ApJ*, 394, 628

- Hamuy, M., Suntzeff, N. B., Heathcote, S. R., et al. 1994, *PASP*, 106, 566
- Hartmann, L. 2009, *Accretion Processes in Star Formation: Second Edition* (Cambridge University Press)
- Hartmann, L., Avrett, E. H., Loeser, R., & Calvet, N. 1990, *ApJ*, 349, 168
- Hartmann, L., Hewett, R., & Calvet, N. 1994, *ApJ*, 426, 669
- Herbig, G. H. & Bell, K. R. 1988, *Third Catalog of Emission-Line Stars of the Orion Population : 3 : 1988*
- Herczeg, G. J., Linsky, J. L., Valenti, J. A., Johns-Krull, C. M., & Wood, B. E. 2002, *ApJ*, 572, 310
- Herczeg, G. J., Walter, F. M., Linsky, J. L., et al. 2005, *AJ*, 129, 2777
- Herczeg, G. J., Wood, B. E., Linsky, J. L., Valenti, J. A., & Johns-Krull, C. M. 2004, *ApJ*, 607, 369
- Hobbs, L. M., York, D. G., Thorburn, J. A., et al. 2009, *ApJ*, 705, 32
- Høg, E., Fabricius, C., Makarov, V. V., et al. 2000, *A&A*, 355, L27
- Huélamo, N., Figueira, P., Bonfils, X., et al. 2008, *A&A*, 489, L9
- Hughes, J., Hartigan, P., Krautter, J., & Kelemen, J. 1994, *AJ*, 108, 1071
- Hummer, D. G. & Storey, P. J. 1987, *MNRAS*, 224, 801
- Hummer, D. G. & Storey, P. J. 1992, *MNRAS*, 254, 277
- Husser, T.-O., Wende-von Berg, S., Dreizler, S., et al. 2013, *A&A*, 553, A6
- Jardine, M. M., Gregory, S. G., & Donati, J.-F. 2008, *MNRAS*, 386, 688
- Jenniskens, P. & Desert, F.-X. 1994, *A&AS*, 106, 39
- Johns, C. M. & Basri, G. 1995a, *AJ*, 109, 2800
- Johns, C. M. & Basri, G. 1995b, *ApJ*, 449, 341
- Johns-Krull, C. M., Valenti, J. A., & Koresko, C. 1999, *ApJ*, 516, 900
- Joy, A. H. 1945, *ApJ*, 102, 168
- Kessler-Silacci, J., Augereau, J.-C., Dullemond, C. P., et al. 2006, *ApJ*, 639, 275
- Koenigl, A. 1991, *ApJ*, 370, L39
- Kóspál, Á., Ábrahám, P., Goto, M., et al. 2011, *ApJ*, 736, 72
- Krautter, J., Wichmann, R., Schmitt, J. H. M. M., et al. 1997, *A&AS*, 123, 329
- Kurosawa, R., Harries, T. J., & Symington, N. H. 2006, *MNRAS*, 370, 580
- Kurosawa, R., Romanova, M. M., & Harries, T. J. 2011, *MNRAS*, 416, 2623
- Kwan, J. & Fischer, W. 2011, *MNRAS*, 411, 2383
- Lamzin, S. A. 1998, *Astronomy Reports*, 42, 322

- Lamzin, S. A., Kravtsova, A. S., Romanova, M. M., & Batalha, C. 2004, *Astronomy Letters*, 30, 413
- Lawson, W. A., Lyo, A.-R., & Muzerolle, J. 2004, *MNRAS*, 351, L39
- Long, M., Romanova, M. M., & Lovelace, R. V. E. 2007, *MNRAS*, 374, 436
- Lutz, D., Feuchtgruber, H., Genzel, R., et al. 1996, *A&A*, 315, L269
- Maíz Apellániz, J. 2006, *AJ*, 131, 1184
- Mamajek, E. E., Meyer, M. R., & Liebert, J. 2002, *AJ*, 124, 1670
- Markwardt, C. B. 2009, in *Astronomical Society of the Pacific Conference Series*, Vol. 411, *Astronomical Data Analysis Software and Systems XVIII*, ed. D. A. Bohlender, D. Durand, & P. Dowler, 251
- Martin, P. G. & Whittet, D. C. B. 1990, *ApJ*, 357, 113
- Martin, S. C. 1996, *ApJ*, 470, 537
- Mathis, J. S., Rumpl, W., & Nordsieck, K. H. 1977, *ApJ*, 217, 425
- McCabe, C., Ghez, A. M., Prato, L., et al. 2006, *ApJ*, 636, 932
- McClure, M. K., Furlan, E., Manoj, P., et al. 2010, *ApJS*, 188, 75
- McGroarty, F. & Ray, T. P. 2004, *A&A*, 420, 975
- Modigliani, A., Goldoni, P., Royer, F., et al. 2010, in *Society of Photo-Optical Instrumentation Engineers (SPIE) Conference Series*, Vol. 7737, *Society of Photo-Optical Instrumentation Engineers (SPIE) Conference Series*
- Monet, D. G., Levine, S. E., Canzian, B., et al. 2003, *AJ*, 125, 984
- Müller, H. S. P., Thorwirth, S., Roth, D. A., & Winnewisser, G. 2001, *A&A*, 370, L49
- Muzerolle, J., Calvet, N., & Hartmann, L. 1998a, *ApJ*, 492, 743
- Muzerolle, J., Calvet, N., & Hartmann, L. 2001, *ApJ*, 550, 944
- Muzerolle, J., Hartmann, L., & Calvet, N. 1998b, *AJ*, 116, 455
- Natta, A., Testi, L., Muzerolle, J., et al. 2004, *A&A*, 424, 603
- O'Donnell, J. E. 1994, *ApJ*, 422, 158
- Osterbrock, D. E. 1989, *Astrophysics of gaseous nebulae and active galactic nuclei*
- Podio, L., Garcia, P. J. V., Bacciotti, F., et al. 2008, *A&A*, 480, 421
- Prato, L., Greene, T. P., & Simon, M. 2003, *ApJ*, 584, 853
- Reipurth, B. & Heathcote, S. 1997, in *IAU Symposium*, Vol. 182, *Herbig-Haro Flows and the Birth of Stars*, ed. B. Reipurth & C. Bertout, 3–18
- Reipurth, B., Pedrosa, A., & Lago, M. T. V. T. 1996, *A&AS*, 120, 229
- Ricci, L., Testi, L., Natta, A., & Brooks, K. J. 2010, *A&A*, 521, A66
- Ridge, N. A., Di Francesco, J., Kirk, H., et al. 2006, *AJ*, 131, 2921
- Rieke, G. H. & Lebofsky, M. J. 1985, *ApJ*, 288, 618

- Robitaille, T. P., Whitney, B. A., Indebetouw, R., Wood, K., & Denzmore, P. 2006, *ApJS*, 167, 256
- Rodmann, J., Henning, T., Chandler, C. J., Mundy, L. G., & Wilner, D. J. 2006, *A&A*, 446, 211
- Romanova, M. M., Ustyugova, G. V., Koldoba, A. V., & Lovelace, R. V. E. 2004, *ApJ*, 610, 920
- Rosenthal, D., Bertoldi, F., & Drapatz, S. 2000, *A&A*, 356, 705
- Rucinski, S. M. & Krautter, J. 1983, *A&A*, 121, 217
- Rucinski, S. M., Matthews, J. M., Kuschnig, R., et al. 2008, *MNRAS*, 391, 1913
- Rudolf, N., Günther, H. M., Schneider, P. C., & Schmitt, J. H. M. M. 2014, submitted to *A&A*
- Sartori, M. J., Lépine, J. R. D., & Dias, W. S. 2003, *A&A*, 404, 913
- Scheegerer, A., Wolf, S., Voshchinnikov, N. V., Przygodda, F., & Kessler-Silacci, J. E. 2006, *A&A*, 456, 535
- Schneider, P. C. & Schmitt, J. H. M. M. 2008, *A&A*, 488, L13
- Schultz, G. V. & Wiemer, W. 1975, *A&A*, 43, 133
- Seifahrt, A., Käufel, H. U., Zängl, G., et al. 2010, *A&A*, 524, A11
- Seperuelo Duarte, E., Alencar, S. H. P., Batalha, C., & Lopes, D. 2008, *A&A*, 489, 349
- Setiawan, J., Henning, T., Launhardt, R., et al. 2008, *Nature*, 451, 38
- Shu, F., Najita, J., Ostriker, E., et al. 1994, *ApJ*, 429, 781
- Skrutskie, M. F., Cutri, R. M., Stiening, R., et al. 2006, *AJ*, 131, 1163
- Stead, J. J. & Hoare, M. G. 2009, *MNRAS*, 400, 731
- Stecher, T. P. & Donn, B. 1965, *ApJ*, 142, 1681
- Stempels, H. C. & Gahm, G. F. 2004, *A&A*, 421, 1159
- Stempels, H. C. & Piskunov, N. 2002, *A&A*, 391, 595
- Storey, P. J. & Hummer, D. G. 1988, *MNRAS*, 231, 1139
- Storey, P. J. & Hummer, D. G. 1995, *MNRAS*, 272, 41
- Szomoru, A. & Guhathakurta, P. 1999, *AJ*, 117, 2226
- Takami, M., Chrysostomou, A., Ray, T. P., et al. 2004, *A&A*, 416, 213
- Testi, L., Natta, A., Shepherd, D. S., & Wilner, D. J. 2003, *A&A*, 403, 323
- Torres, C. A. O., Quast, G. R., da Silva, L., et al. 2006, *A&A*, 460, 695
- Trumpler, R. J. 1930, *PASP*, 42, 214
- Uchida, Y. 1983, in *Astrophysics and Space Science Library*, Vol. 102, IAU Colloq. 71: Activity in Red-Dwarf Stars, ed. P. B. Byrne & M. Rodono, 625
- Udalski, A. 2003, *ApJ*, 590, 284

- Unsöld, A. & Baschek, B. 2002, *Der neue Kosmos. Einführung in die Astronomie und Astrophysik*
- Vacca, W. D. & Sandell, G. 2011, *ApJ*, 732, 8
- Valenti, J. A. & Johns-Krull, C. M. 2004, *Ap&SS*, 292, 619
- van Eyken, J. C., Ciardi, D. R., von Braun, K., et al. 2012, *ApJ*, 755, 42
- van Leeuwen, F. 2007, *A&A*, 474, 653
- Vernet, J., Dekker, H., D'Odorico, S., et al. 2011, *A&A*, 536, A105
- Vernet, J., Kerber, F., Mainieri, V., et al. 2010, *Highlights of Astronomy*, 15, 535
- Waters, L. B. F. M. & Waelkens, C. 1998, *ARA&A*, 36, 233
- Weingartner, J. C. & Draine, B. T. 2001, *ApJ*, 548, 296
- Welty, D. E. & Fowler, J. R. 1992, *ApJ*, 393, 193
- Whelan, E. T., Ray, T. P., & Davis, C. J. 2004, *A&A*, 417, 247
- Whittet, D. C. B. 1988, in *Dust in the Universe*, ed. M. E. Bailey & D. A. Williams, 25–53
- Whittet, D. C. B. 1992, *Dust in the galactic environment*
- Whittet, D. C. B., Martin, P. G., Fitzpatrick, E. L., & Massa, D. 1993, *ApJ*, 408, 573
- Wichmann, R., Krautter, J., Covino, E., et al. 1997, *A&A*, 320, 185
- Wilking, B. A., Meyer, M. R., Robinson, J. G., & Greene, T. P. 2005, *AJ*, 130, 1733
- Yang, H., Herczeg, G. J., Linsky, J. L., et al. 2012, *ApJ*, 744, 121
- Yang, H., Johns-Krull, C. M., & Valenti, J. A. 2005, *ApJ*, 635, 466

Acknowledgements

There are many people I want to thank for supporting me in my work for this doctoral thesis and for making my time at the Hamburger Sternwarte a very enjoyable period of my life.

First of all, I want to thank my advisor Prof. Jürgen Schmitt for giving me the opportunity to work in his group and letting me choose my topic on my own, for his advice, and for encouraging me to present my work at conferences.

I am also very grateful to Moritz Günther (Harvard-Smithsonian Center for Astrophysics) for suggesting and offering his VLT/X-Shooter data for my thesis. A big thank-you to him for the great collaboration we had so far and for all his advice and support, both in science and in personal life. Further, I want to thank my collaborators Christian Schneider (Hamburger Sternwarte) and Alyssa Goodman (Harvard University). Discussing all the different aspects of my work with them was always very pleasant. Moreover, I wish to thank Jeff Bary (Colgate University) and Sean Matt (University of Exeter) for their support, although most of it happened probably unbeknownst to them.

I likewise thank the Harvard-Smithsonian Center for Astrophysics for hosting me in Spring 2013 where part of this work was done. Especially, I want to thank Sarah Block and Judy Schwab for their help in the organisation of my stay and Mohaddesseh “Moha” Azimlu for her help in settling in at the CfA. It was a wonderful time.

Additional thanks to Moritz Günther, Christian Schneider, Birgit Fuhrmeister, and Carolina von Essen for proof-reading my thesis.

To my family and friends, many thanks for everything.

I acknowledge support by the Deutsches Zentrum für Luft- und Raumfahrt e. V. (DLR) under project numbers 50 OR 1002 and 50 OR 1114, the Deutscher Akademischer Austauschdienst e. V. (DAAD), who financed my visit to the CfA with a stipend, and the Graduiertenkolleg (GrK) 1351 “Extrasolar Planets and their host stars” of which I was an associated member.

This research has made use of NASA’s Astrophysics Data System as well as the SIMBAD database and the VizieR catalogue access tool, both operated at CDS, Strasbourg, France.

Last but not least, greetings and thanks to all the people from the Hamburger Sternwarte and to everyone else who would like to be mentioned here that I forgot.